

JAMES COOK UNIVERSITY  
COLLEGE OF SCIENCE &  
ENGINEERING

EG4011/2  
Chemical Engineering

INFRARED THERMAL IMAGE ANALYSIS FOR THE  
DETERMINATION OF BULK PARTICLE PROPERTIES  
IN CASCADING PARTICLE CURTAINS

Laura Kuskopf

Thesis submitted to the College of Science & Engineering in partial fulfillment  
of the requirements for the degree of Bachelor of Engineering  
(Chemical Engineering)

7<sup>th</sup> October, 2016

## Statement of Access

I, the undersigned, author of this work, understand that James Cook University may make this thesis available for use within the University Library and, via the Australian Digital Theses network, for use elsewhere.

I understand that, as an unpublished work, a thesis has significant protection under the Copyright Act and I do not wish to place any further restriction on access to this work.

Signature



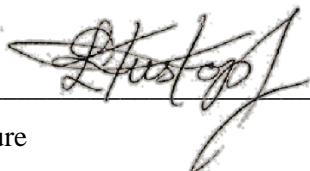
24/11/2016

Date

## Declaration of Sources

I declare that this thesis is my own work and has not been submitted in any form for another degree or diploma at any university or other institution of tertiary education. Information derived from the published or unpublished work of others has been acknowledged in the text and a list of references is given.

---



---

Signature

24/11/2016

---

Date

## Abstract

Acquiring accurate temperature data from complex two-phase systems, like particle curtains, is inherently difficult. As a consequence, computational models often lack accurate thermal data required for validation to optimise these curtains. Infrared (IR) thermal imaging is gaining attention as an alternative to direct measurements for its non-invasive procurement of temperature fields. Little research however has been done to pinpoint the limitations of the technique. This project therefore aimed to further assesses the strengths and limitations of infrared imaging methods as applied to hot particle curtains.

Chapter 1 provides an introduction to particle curtains. This review summarises the key problem statement; despite infrared imaging's potential, methods required to successfully integrate visible (VIS) imagery with IR thermography in two-phase systems are not well established. Broad research aims are also presented in this section, namely that this thesis shall involve the characterization of bulk curtain behavior of hot particle curtains by means of VIS and IR imaging integration.

Infrared imaging may be coupled with VIS imaging to determine a variety of bulk particle curtain properties. These properties include curtain edges and temperature. Examples of successful applications where VIS and IR imaging have been integrated are presented in Chapter 2. In addition, the review of literature describes the underlying principles of IR thermography, emphasising key considerations to be made when undertaking IR imaging. Particulate emissivity, for example, was determined to have the greatest influence on the accuracy of recorded thermographical data. Also introduced are common image analyses, such as thresholding. This is a processing technique used to separate meaningful data in the foreground from the undesirable background.

The methodologies used to generate a hot particle curtain with consistent properties are given in Chapter 3. This includes descriptions of the experimental apparatus, as well as methods to heat particles and measure their mass flow rate. This thesis focused on generating two distinct types of curtain behavior: converging and diverging. Varying slot width from where the particles flow induces this behavior. The 20mm and 60mm slot widths exhibited different initial solids volume fractions, a property which was the focus of much subsequent analysis. Silica beads of  $257\mu\text{m}$  were chosen as smaller sized particles produce the best agreement with computational fluid dynamics. Thirteen sampling locations at which direct thermocouple temperatures were taken are also justified; two sampling series with curtain depth (at 4cm and 60cm height) compare the curtain depth profiles, and a series with height

are used to compare against the centerline IR temperature profile. As confidence in direct temperature measurements and mass flow rate is required, descriptions on how error was quantified (i.e. by standard deviation) are provided in this section. Specifically, the cold mass flow rate standard deviation was only 0.00055kg/s, attributed to thorough equipment cleaning methods. Thermocouple standard deviation was found to be a linear function of height, increasing from 0.3°C at 4cm to 1.5°C at 60cm height (at the curtain edge). The specifications of both the IR and VIS image cameras are described next, along with their necessary software utilized to extract a series of images. Prior to testing, calibrations of both the particulate emissivity and light intensity were required. In-camera calibration was the chosen method to determine particle emissivity. Found to be 0.89, an absolute error was postulated to be  $\pm 0.02$ , which is discussed in later image analysis.

Chapter 3 concludes with a section on recounting the applied image calibration and image analysis techniques. These techniques are implemented primarily in MATLAB, by utilising the image analysis toolbox. The two chosen edge detection techniques, namely VIS image thresholding and temperature field differentiation/polynomial fitting, are described. Standard deviations for both edge detection methods were determined as a function of height by the collection of multiple VIS and IR images. Lastly, the approach used to assess the degree of alignment between direct thermocouple and infrared imaging (a two-tail t-test) is outlined. This test was extended to three dimensions. The purpose of this was to assess the acknowledged potential of IR imaging to integrate temperatures through curtain depth.

Results and discussions presented in Chapter 4 begin with the presentation of direct temperature measurements recorded with curtain depth. Distinctly different modes of heat transfer were illustrated between the 20mm and 60mm slot widths. These were evident from the direct thermocouple measurements taken with curtain depth, but were most noticeable in the normalized temperature profiles. Comparative solids volume fractions were then obtained by VIS image analysis. They clarified that the rate of change of volume fraction with height, due to increasing particle velocity, is independent of initial solids volume fraction. Furthermore, the commonly made assumption that image intensity is proportional to volume fraction does not hold in these experiments due to the high mass flow rate. The 60mm slot width was found to align with the direct thermocouple temperature deeper within the curtain than for the 20mm slot width, a direct result of their comparative solids volume fractions. Another important experimental result was the comparison of two obtained temperature profiles at different emissivities, providing renewed confidence in the previously determined 0.89 value. Edge detection methods were shown to have unique strengths and limitations; VIS image thresholding performed remarkably in characterizing

realistic, asymmetric behaviours, whereas IR gradient/polynomial fitting produced highly uniform temperature segregation across the curtain edge with curtain height.

The final noteworthy result to stem from this investigation presented in Chapter 4 was comparison of IR centerline temperature and bulk heat transfer for each slot width condition. Thermochemical methods successfully validated that, despite the improved heat transfer observed down the centerline of 60mm slot widths, overall the 20mm slot width achieved superior particulate heat transfer at the experimental conditions applied in this thesis. Chapter 5 presents the conclusions and recommendations of the research.

## Acknowledgements

First and foremost, I would like to extend my sincere thanks to my supervisor, Dr. Madoc Sheehan. His unique perspective and unyielding support was by far the greatest bonus of undertaking this thesis. I shall sorely miss our lengthy dialogues from which was born a great deal of critical thought, analysis, and best of all, self-confidence.

Secondly I would like to acknowledge my thesis room companions. Our little family will shortly be torn apart, but the banter and laughs will not be forgotten.

Thanks must also go to the legend, Aaron Cheng, for dutifully assisting in over thirty experiments at no personal benefit. Stuart Hinchliff also deserves a standing ovation for readily offering up his MATLAB handy hints whenever coder's-block had struck.

To my family, thank you for putting up with me, period. Especially thank you to my mother for those Friday coffees, and to my family members who completed my chores when I regularly failed to make it home from the lab (there had to be some advantages, right?).

Above all I am thankful for Mitchell, for his unimaginable support, day in... day out. For believing in me when I didn't, and for empowering me to direct every ounce of effort into finishing this grueling degree. Without you, I would have been surely lost.

## Table of Contents

<b>Statement of Access.....</b>	<b>i</b>
<b>Declaration of Sources .....</b>	<b>ii</b>
<b>Abstract.....</b>	<b>iii</b>
<b>Acknowledgements .....</b>	<b>vi</b>
<b>Table of Contents .....</b>	<b>vii</b>
<b>List of Figures.....</b>	<b>x</b>
<b>List of Tables .....</b>	<b>xiii</b>
<b>List of Terms .....</b>	<b>xv</b>
<b>1.0 Introduction.....</b>	<b>1</b>
<b>1.1 Objectives .....</b>	<b>2</b>
<b>2.0 Literature Review .....</b>	<b>3</b>
<b>2.1 Industrial Applications of Particle Curtains.....</b>	<b>3</b>
<b>2.2 Particle Curtain Models .....</b>	<b>5</b>
<b>2.3 Particle Curtain Temperature Measurement .....</b>	<b>6</b>
<b>2.3.1 Traditional Direct Temperature Measurements.....</b>	<b>6</b>
<b>2.3.2 IR Thermal Imaging .....</b>	<b>8</b>
<b>2.4 Infrared Theory .....</b>	<b>15</b>
<b>2.4.1 The Electromagnetic Spectrum.....</b>	<b>15</b>
<b>2.4.2 Blackbody Radiation .....</b>	<b>16</b>
<b>2.4.3 Emissivity .....</b>	<b>17</b>
<b>2.4.4 Infrared Detectors .....</b>	<b>19</b>
<b>2.5 Image Analysis .....</b>	<b>21</b>
<b>2.5.1 Image Thresholding.....</b>	<b>21</b>
<b>2.5.2 Visible Image Analysis.....</b>	<b>22</b>
<b>2.5.3 IR Image Analysis .....</b>	<b>24</b>
<b>2.6 Conclusions .....</b>	<b>24</b>
<b>3.0 Methodology .....</b>	<b>26</b>
<b>3.1 Equipment Selection.....</b>	<b>28</b>
<b>3.1.1 Particulate Properties .....</b>	<b>28</b>
<b>3.1.2 Experimental Apparatus .....</b>	<b>29</b>

3.1.3	Direct Temperature Measurement .....	30
3.1.4	Imaging .....	34
<b>3.2</b>	<b>Experimental Procedures.....</b>	<b>36</b>
3.2.1	Initial Thermal Conditions.....	36
3.2.2	Mass Flow Rate .....	37
3.2.3	Hopper and Curtain Temperature .....	38
3.2.4	Bulk Curtain Heat Transfer .....	41
3.2.5	Image Calibration .....	42
<b>3.3</b>	<b>Image Analysis .....</b>	<b>47</b>
3.3.1	MATLAB Code Development .....	47
3.3.2	IR and Direct Thermocouple Temperature Alignment.....	52
3.3.3	Summary.....	54
<b>4.0</b>	<b>Results &amp; Discussion.....</b>	<b>55</b>
4.1	Temperature Variation with Curtain Depth.....	55
4.2	VIS Image Intensity vs. Height.....	59
4.3	Comparison of IR and Thermocouple Temperature .....	60
4.3.1	Influence of Emissivity.....	67
4.4	Edge Detection Methods .....	68
4.4.1	VIS Image Edges via Thresholding.....	68
4.5	VIS Image Edges vs. IR Image Edges.....	69
4.6	Bulk Curtain Temperature.....	71
4.7	Summary .....	72
<b>5.0</b>	<b>Conclusions and Recommendations .....</b>	<b>73</b>
<b>6.0</b>	<b>References.....</b>	<b>76</b>
Appendix 1,	Risk Assessment for Mastersizer3000 .....	80
Appendix 2,	Hopper Specifications .....	82
Appendix 3,	Spreader Box Assembly Specifications.....	83
Appendix 4,	General Experimental Process .....	86
Appendix 5,	Risk Assessment for General Methodology .....	87
Appendix 6,	Flow Rate Consistency .....	91
Appendix 7,	Emissivity Calibration Steps .....	92
Appendix 8,	Emissivity Graphs .....	93

<b>Appendix 9, MATLAB Code .....</b>	<b>94</b>
<b>Appendix 10, VIS Image Threshold Consistency.....</b>	<b>98</b>
<b>Appendix 11, VIS Image Repeatability.....</b>	<b>100</b>
<b>Appendix 12, IR Image Repeatability.....</b>	<b>101</b>

*Word Count: 20,000*

## List of Figures

Figure 2.1: Typical particle curtains in a flighted rotary dryer [12] .....	4
Figure 2.2: Conceptual design of a solid particle receiver [16] .....	4
Figure 2.3: An example of a 3-dimensional CFD contour.....	5
Figure 2.4: (a) Particle temperature sampling cup in the particle curtain during data collection, & (b) numerical prediction vs. experimental data of dimensionless particle temperature at high & low (0.02 kg/s & 0.04kg/s) mass flow rates at initial temperature of 773K. [16].....	6
Figure 2.5: Schematic diagram of Wardjiman et al.'s experimental setup, also showing the diagram of temperature probes: (a) solid temperature, and (b) gas temperature [19].....	7
Figure 2.6: Direct thermocouple measurements in a particle curtain system [9].....	8
Figure 2.7: A faulty circuit breaker amongst an array of visibly identical devices, indicated by the temperature scale [8]......	9
Figure 2.8: Steps for gas concentration measurements used by Dang et al. inside gas-solids systems via a combination of VIS and IR images: (a) VIS camera image, (b) particle detection from VIS image, (c) IR camera image, (d) particle removal by stitching VIS-IR image, (e) apparent absorbance, and (f) concentration profile [10] .....	10
Figure 2.9: IR image processing steps showing the raw image (a) that was processed by direct filtering (b). The filter used corrects for wrong temperature readings at particle edges that in fact are due to partly covered pixels, by filtering these pixels off [11]. .....	11
Figure 2.10: 2D thermal image of a particle curtain at slot width=60mm, $d_s=290\mu\text{m}$ and $m^\circ=0.063\text{kg/s}$ .....	12
Figure 2.11: Thermocouple and infrared temperatures calculated from visible image photography (a) $d_s=290 \mu \text{ m}$ , $m^\circ=0.15\text{kg/s}$ and slot width=20mm (b) $d_s=610 \mu \text{ m}$ , $m^\circ=0.047\text{kg/s}$ and slot width=60mm. [9] .....	13
Figure 2.12: Particle curtain shape at small particle size, $d_s=290\mu\text{m}$ , and (a) $m=0.040\text{kg/s}$ with slot width=20mm, compared to (b) $m=0.040\text{kg/s}$ with slot width=60mm [28].....	13
Figure 2.13: Effect of slot width on raw IR centerline temperatures at constant $ds=290\mu\text{m}$ particle size [9].....	14
Figure 2.14: Location of the infrared region on the electromagnetic spectrum [33] .....	15
Figure 2.15: Spectral emittance of a blackbody on a logarithmic scale, where the coloured region represents the visible wavelengths [34] .....	16
Figure 2.16: Comparison of spectral emission for black, gray and real surfaces [35] .....	17
Figure 2.17: Variation of glass spectral properties with wavelength [22] .....	18
Figure 2.18: (a) A non-conducting 'hot' object to be studied is placed with its surface normal	

facing 90° to the IR camera lens. Then, measurements of the emitted radiation are recorded as a function of angle while rotating the object. (b) Actual surface temperature measured by contact thermometry, and emissivity value in the IR camera software is altered until the real temperature is shown (emissivity for correct temperature value given on the y-axis) [34]... 19	
Figure 2.19: Effect of FOV on minimum detectable size for an IR camera [37].....	20
Figure 2.20: Processed VIS images of a particle curtain with various threshold intensities .	21
Figure 2.21: Ideal biomodal histogram, showing the misclassification of pixels following calculation of the level threshold by Otsu's method [39] .....	22
Figure 2.22: Image of particle curtain captured at the wall of duct by high-speed camera [42].....	23
Figure 2.23: (a) Solid volume fraction contour of a particle curtain determined by CFD, & (b) solid volume fraction gradient at various heights of the curtain's middle plane [9] .....	23
Figure 2.24: (a) Temperature gradient profiles and (b) overlaid edges on thermal image, $ds=290\mu\text{m}$ , $m^{\circ}=0.066\text{kg/s}$ and slot width=20mm [9] .....	24
Figure 3.1: Methodology overview.....	26
Figure 3.2: Particle size distribution produced by Malvern Mastersizer 3000, giving mean particle diameter, $d_s=257\mu\text{m}$ .....	28
Figure 3.3: Side view of experimental apparatus with relative dimensions (Afshar [9]) .....	29
Figure 3.4: Comparison between the old thermocouples used by S. Afshar [9] and the new cups developed in this thesis.....	31
Figure 3.5: Comparison of two sampling cup hole sizes, one too wide (i.e. insufficient hold-up) .....	31
Figure 3.6: Sampling cup alignment with spreader box slot opening, for a height of 4cm and depth of 0cm. .....	32
Figure 3.8: Testo 610 humidity sensor (left) with a temperature reading greater than that of three attached thermocouples to the data logger thermometer (SE-378) (right).....	34
Figure 3.9: Sampling location and depth of measurement for points A, B and C measured using a thermocouple .....	37
Figure 3.10: Plot of internal hopper temperature in 120°C oven at Points A, B and C over a 12-hour period.....	37
Figure 3.12: Example of hopper and sampling cup temperature recorded during direct sampling cup measurements .....	39
Figure 3.13: Plot of five repeat thermocouple data trends for 60mm slot width, taken at 8cm depth and 4cm height .....	39
Figure 3.15: Set-up of IR camera relative to sample, line of sight directed through the aluminum container onto the sampling cup .....	43

Figure 3.16: Optional thermocouple placements in silica bead sample: with tip submerged until just concealed (a), and with the tip resting against the surface (b).....	43
Figure 3.20: MATLABs curve-fitting interface, used to show the goodness of fit for the curtain temperature with depth.....	47
Figure 3.21: Pictorial description of the steps taken to scale images in MATLAB. Shown for VIS images.....	49
Figure 3.22: Raw VIS image (a) and Gaussian filtered image with two-level threshold (b). ..	50
Figure 3.23: Edge detection result for 20mm (a) and 60mm slot width (b), overlaid on original grayscale, Gaussian smoothed images. Colours correspond to inner (●) and outer (○) edges. ....	51
Figure 3.24: (a) Temperature versus width at three different heights of the middle plane, with (b) their corresponding curve-fitted temperature gradients found using a second order polynomial fit. Note (---) indicates the separation of left and right polynomials. ....	52
Figure 3.25: Comparison of centerline temperatures taken as a 3-pixel average (approach taken by Afshar [9]) versus profile averaged over the sampling cup width. ....	53
Figure 4.1: Thermocouple temperature profiles for 20mm slot width as a function of curtain depth.....	56
Figure 4.2: Thermocouple temperature profiles for 60mm slot width as a function of curtain depth.....	56
Figure 4.3: Normalised temperature profile where $\phi_h = (T - T_{min}) / (T_{min} - T_{max})$ for 20mm slot width curtain .....	57
Figure 4.4: Normalised temperature profile where $\phi_h = (T - T_{min}) / (T_{min} - T_{max})$ for 60mm slot width curtain, with interpolated profiles for additional key heights .....	58
Figure 4.5: Pictorial description of a single IR pixel and the relative temperatures of perceived particles (drawn roughly to scale). .....	59
Figure 4.6: Normalised VIS image intensity centerline profile for 20mm and 60mm slot widths.....	60
Figure 4.7: IR average temperature field data for the 20mm(a) and 60mm (b) slot width curtain .....	61
Figure 4.8: Comparison of IR and thermocouple profile temperatures (with discrete temperatures, ‘o’) for 20mm slot width with curtain height. ....	63
Figure 4.9: Comparison of IR and thermocouple profile temperatures (with discrete temperatures, ‘o’) for 60mm slot width with curtain height. ....	63
Figure 4.10: Adjusted IR centerline temperature from change in emissivity value. Extrapolated intercepts, ‘o’, also presented. ....	67
Figure 4.11: Two-level threshold image of 20mm slot width (a) and 60mm slot width (b) curtain .....	68

Figure 4.12: VIS edge detection via thresholding for 20mm (a) & 60mm (b) slot width, overlaid onto raw IR image. Also IR edges predicted via temperature differentiation for 20mm (a) & 60mm (d), where black and white lines correspond to 1 <sup>st</sup> and 2 <sup>nd</sup> roots of the polynomial respectively .....	70
Figure 4.13: Centerline profile of the convergent (60mm) and divergent (20mm) particle curtain .....	71

## List of Tables

Table 1: Spreader box assembly components for nominated curtains .....	30
Table 2: Specifications of NEC Avio H2600 Series IR camera .....	34
Table 3: Specifications and settings of Nikon D80 VIS image camera .....	35
Table 4: Direct thermocouple consistency assessment for 60mm slot width, width, taken at 8cm depth and 4cm height .....	40
Table 5: Recorded sample surface temperature and corresponding absolute emissivity error .....	45
Table 6: T-test results comparing 20mm slot width thermocouple and IR temperatures .....	65
Table 7: T-test results comparing 60mm slot width thermocouple and IR temperatures .....	66
Table 8: Results of assessment of silica temperature change during descent .....	72

## List of Terms

- AOI** - Area of Interest  
**CFD** - Computational Fluid Dynamics  
**CSP** - Concentrating Solar Power  
**DIA** - Digital Image Analysis  
**EM** - Electromagnetic  
**FRD** - Flighted Rotary Dryer  
**IR** - Infrared  
**VIS** - Visible

## 1.0 Introduction

Effective quantification of temperature is invaluable in many engineering applications. As the most frequently measured physical quantity, it holds significant potential in the optimization of heat transfer in a diverse range of engineering systems. One particularly challenging engineering process that has proven problematic to acquire thermal data for is the particle curtain.

Particle curtains are defined as a continuous stream of particles made to fall in a curtain-like shape through a gaseous medium. They are employed in a wide variety of industries as heat exchangers for particulate mediums, due primarily to their simplicity and low operational costs [1, 2]. Examples include the flighted rotary dryer (FRD) and the hopper, which are common in mineral and pharmaceutical industries. However, particle curtains are steadily emerging in promising new renewable energy technologies for use in concentrating solar power (CSP) plants. These solar particle receiver designs are currently in the early demonstration phase, delivering improved thermal efficiency through their direct storage of heat within sand-like particles [3, 4].

The dynamics of cascading solid particles in a two-phase process are inherently complex. This complexity stems from the incorporation of many physical phenomena, including radiation, conduction and convection, particle flow dynamics and gas-particle interactions [5]. Over the last three decades, numerous intricate models of particle curtains have been developed with the aim of optimizing and controlling devices that incorporate them. Computational fluid dynamics (CFD) modeling, for example, provides a complete mathematical description of fluid behavior using conservation laws. Irrespective of the type of model selected, refinement of numerical models continues to be hindered by a lack of knowledge about the critical parameter: temperature. Difficulty in obtaining temperature data in these systems for numerical data validation stems from the inability of existing technologies to record the bulk temperature profile across the curtain. At present, researchers are restricted instead to the use of sampling cups fitted with thermocouples to record discrete measurements [6].

An innovative, new technique with the potential to revolutionize thermal analyses of multi-phase systems is infrared (IR) thermal imaging. IR imaging is a non-invasive technique capable of detecting electromagnetic energy emitted by a material and converting it into a surface temperature field [7]. Thermal imaging is currently applied as a form of predictive maintenance and quality control in the civil, energy and processing industries [8]. Equipment such as pipelines and motors, for example, can be monitored qualitatively for deterioration by distinguishing “hot spots” of a colourised temperature field. Extensive advancement of IR technology over the last

decade has further increased the accessibility of IR systems, making the extraction of quantitative temperature field data viable. This development has broadened the demand for IR thermal imagery in industrial applications.

Initial investigations of particle curtains using IR techniques concluded curtains of low volume fraction and large particle size suffered from background interference [9]. Visible (VIS) imagery, which is a well-established technique for visualising the volume fraction of particles, would clarify this dependence, leading to the collection of more reliable IR thermographic temperature data in dilute two-phase systems. Novel IR techniques have been successfully used in the determination of gas concentration in gas-solid fluidised beds [10], with recent experiments successfully coupling high-resolution VIS imagery with IR imagery [11]. The result obtained from this simultaneous image recording was both instantaneous thermal and hydrodynamic data of the two-phase system.

The collection of IR and VIS images and validation of the thermographic temperature data enable the non-invasive determination of bulk particle properties, such as temperature, in a wide range of two-phase systems. Additionally, whole-field temperature data will provide engineers with improved confidence in computational fluid dynamics modelling of particle curtains, and ultimately lead to more efficient equipment designs. Despite its potential, the methods required to successfully synchronise and integrate visible imagery with IR thermography in two-phase gas-particle systems are not well established. Furthermore, the accuracy and reliability of the IR thermo graphic temperature data is uncertain under conditions of low solids volume fraction.

## 1.1 Objectives

This thesis aims to assess the use of IR thermography to capture characteristics of hot particle curtains. To achieve this, VIS images and IR thermal images will be collected from a candidate particle curtain system to develop methods of integrating IR and visible image data. Subsequently, the objective is to obtain an accurate description of the thermal characteristics of hot particle curtains cooling in quiescent, ambient air. This thermal data will then be used to characterize the bulk behavior of particle curtains.

## 2.0 Literature Review

In this literature review, a general description of particle curtain applications and existing models is provided. Subsequently, a critical review of the application of IR technology in particle curtain analysis highlights the benefits of IR and VIS imagery coupling in contrast to existing direct temperature measurement techniques. Examples of successful integration of IR and VIS imagery in two-phase systems are also specified, with details of their strengths and limitations. The fundamentals of infrared theory are presented to emphasize the influences of key material properties and environmental factors on IR thermographical measurements. Finally, with emphasis on the detection of leading and trailing curtain edges, key image analysis techniques are presented to demonstrate the integration possibilities of IR and VIS imagery.

### 2.1 Industrial Applications of Particle Curtains

A particle curtain may be defined as a continuous stream of particles falling through a gaseous medium in an arched, curtain-like shape. They are employed in the food, mineral and pharmaceutical industries as heat exchangers for particulate mediums, due primary to their simple operation and flexibility to handle a wide range of throughputs [1, 2].

A common industrial apparatus using particle curtains is the flighted rotary dryer (FRD). These dryers play an important role in the production of raw sugar for example, where internally fitted 'flights' of a long cylindrical shell lift the wetted sugar crystals, causing them to fall in a curtain during rotation (shown in Figure 2.1). During the particles' fall, the heat and mass transfer experienced by the bulk particles is a measure of dryer efficiency. Everything from flight design, air stream quality, air velocity, dryer throughput, rotational speed, and physical particle properties can influence dryer efficiency.

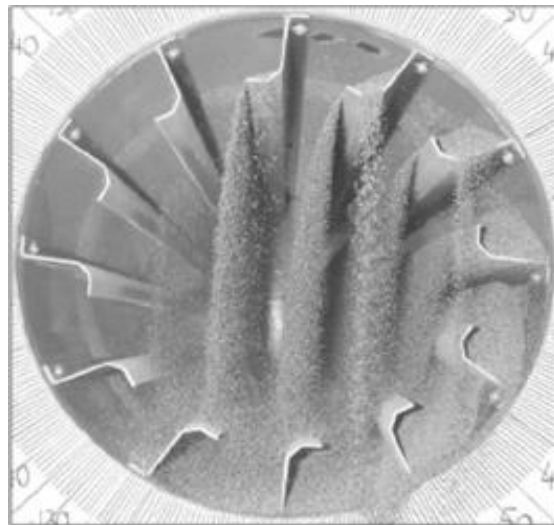


**Figure 2.1:** Typical particle curtains in a flighted rotary dryer [12]

The particle curtain is finding new and innovative applications in the renewable energy sector. Concentrating solar power (CSP) plants are a promising, future-orientated renewable energy technology, with various models in either the early operation or demonstration phase [4]. One such example is the central receiver configuration. Central receiver technology utilizes falling particles, which have absorbed concentrated sunlight reflected from heliostats. Subsequently, the particles are passed through a particle-to-steam heat exchanger to drive a power plant [13]. The benefit of these receivers over other CSP technologies is their ability to improve plant efficiency and lower the costs of energy storage [14]. This is achieved by directly storing heat in the sand-like particles, allowing the standard 600°C temperature limit of standard thermal to electric conversion systems to be surpassed [3, 15].

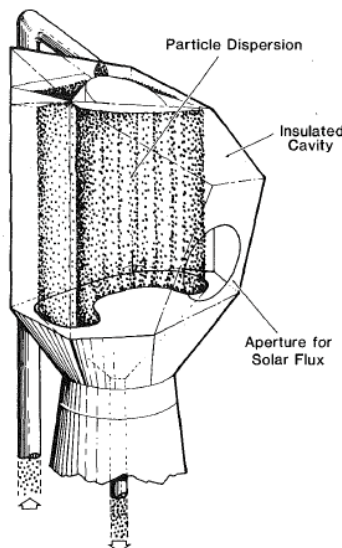


**Figure 2.2:** Conceptual design of a solid particle receiver [16]

## 2.2 Particle Curtain Models

Due to the existing industrial importance of particle curtains and their progression into new renewable energy markets, improved heat-transfer models are in demand. Consequently, there is incentive to develop superior experimental methods for refining these models. Over the last three decades, numerous models of particle curtains have been developed with the aim of optimizing and controlling devices (such as FRDs) that incorporate them [1, 2, 17].

CFD modeling in particular has preferentially emerged as a powerful tool to model multi-phase particle-gas systems [9]. This modeling technique provides a complete mathematical description of fluid behavior using the conservation laws, equations that may be discretised and computationally solved in algebraic form [18]. Key parameters required to apply CFD modelling to a system include knowledge about initial and final curtain temperature, initial particle velocity and slot width (i.e. the dimensions of the bulk particles at the highpoint of the curtain). The bulk solid volume fraction must also be estimated. Due to the discretized nature in which the governing CFD equations are computed, the output of this model is a matrix of field data. Thus, two and three-dimensional arrays describing physical properties of the system, such as temperature, particle velocity and solids volume fraction, are made available by CFD. Likewise, the nature of CFD models mean they may be adjusted to incorporate field data to achieve better agreement with experimental results.

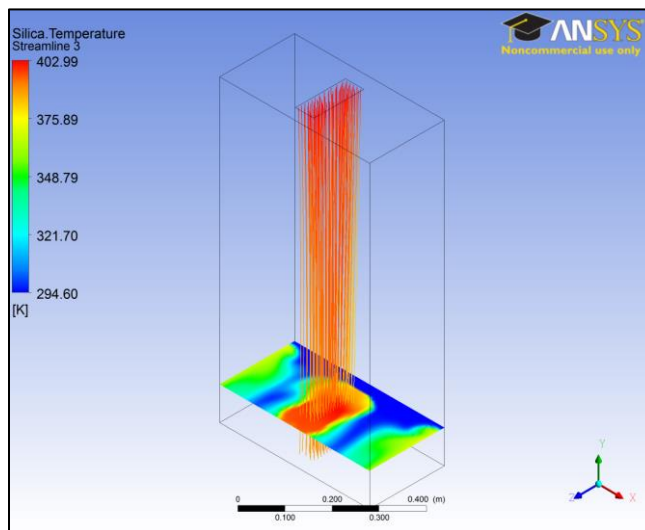


*Figure 2.3: An example of a 3-dimensional CFD contour*

## 2.3 Particle Curtain Temperature Measurement

### 2.3.1 Traditional Direct Temperature Measurements

Experiments undertaken for the purpose of developing and validating particle curtain models have traditionally been based on discrete temperature measurements. These discrete measurements are usually taken using thermocouples or sampling cups fitted with a bare thermocouple [6]. One of the earliest investigations into particle curtain heat transfer was performed by Hruby et al. [16]. The primary objective was to understand the convective heat transfer of free-falling particle curtains in quiescent and cross-flow air in a simple heat and mass transfer model, as compared with temperatures recorded by means of a sampling cup. This cup contained a small hole in the base to generate a constant particle hold-up. A key limitation of this technique is disturbance of the curtain by the sampling cup, as shown in Figure 2.4(a), preventing simultaneous thermocouple air measurement.

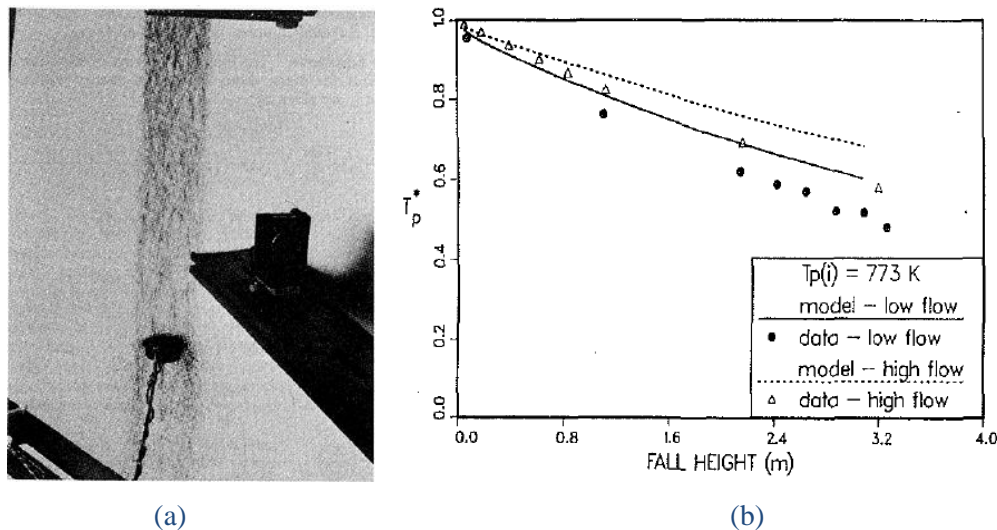


**Figure 2.4:** (a) Particle temperature sampling cup in the particle curtain during data collection, & (b) numerical prediction vs. experimental data of dimensionless particle temperature at high & low ( $0.02 \text{ kg/s}$  &  $0.04 \text{ kg/s}$ ) mass flow rates at initial temperature of  $773\text{K}$ . [16]

Hruby et al. [16] noted that hot particle flow produced poor agreement between numerical and experimental particle velocity, air temperature and particle temperature. The latter is shown in Figure 2.4(b). Over-predictions were attributed to an underestimation of the steady state drag coefficient,  $C_D$ . However, insufficient and/or inaccurate curtain temperature data was an underlying contributor. Wardjiman et al. [19] extended on Hruby et al.'s initial experiments to investigate the heat transfer between the gas and the particles when the curtain spanned the entire width of a duct (i.e. no preferential gas flow). The experimental setup used is shown in Figure 2.5. Note the discrete sampling probes used to record gas and particle temperatures in Figure 2.5(a) and (b) inset.

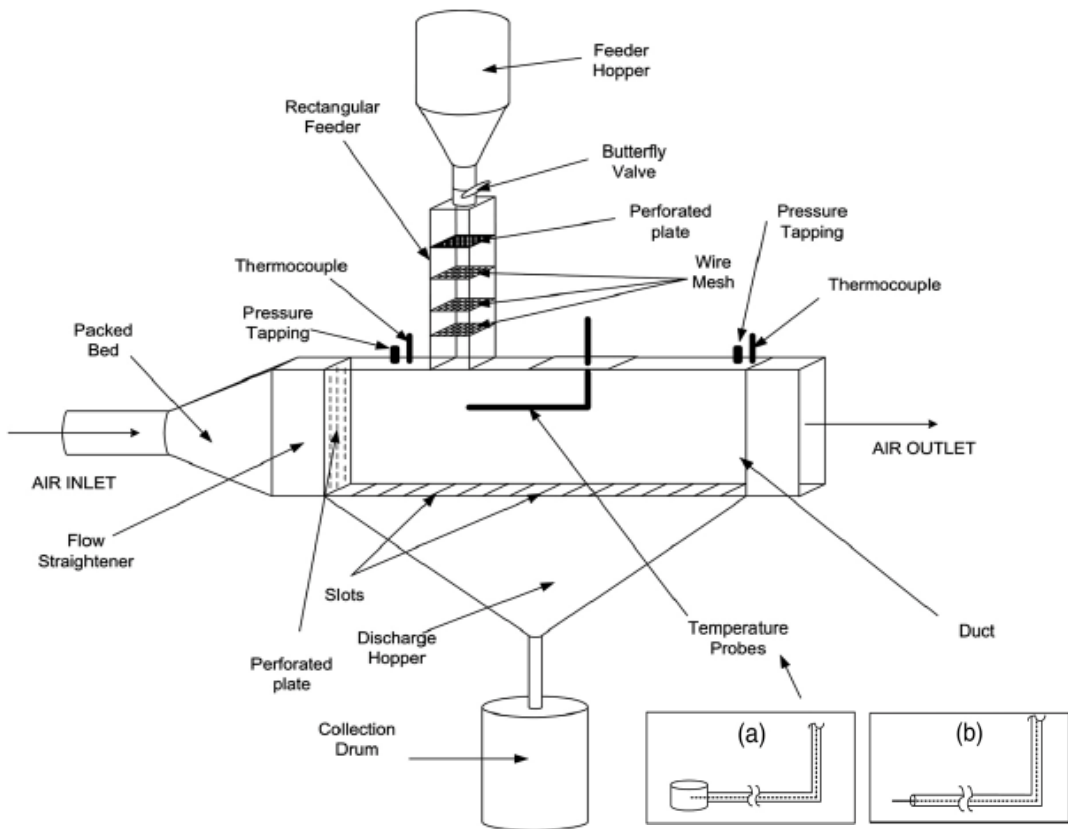


**Figure 2.5:** Schematic diagram of Wardjiman et al.'s experimental setup, also showing the diagram of temperature probes: (a) solid temperature, and (b) gas temperature [19]

In experiments performed by Afshar [9], graphs of the continuous data logging of equivalent temperature probes were presented. Thermocouple readings were a result of averages taken during regions of greatest ‘stability’ emphasized in Figure 2.6. It was evident that thermocouple temperature slowly skewed upward rather than leveling out over time. This trend was due either to the accumulation of particles or the associated rate of heat conduction, an effect that was especially pronounced for larger particle sizes.

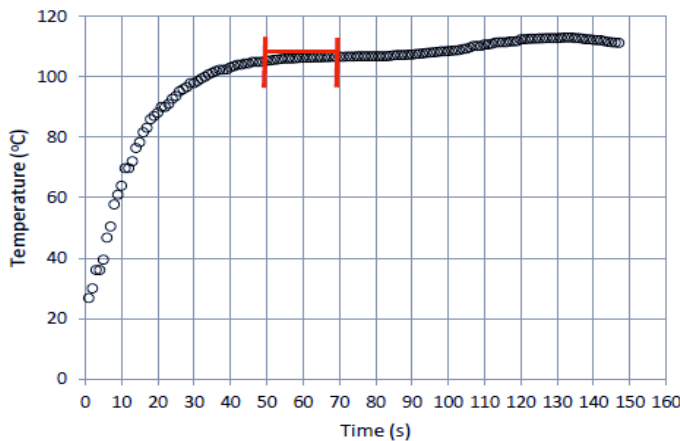


**Figure 2.6:** Direct thermocouple measurements in a particle curtain system [9]

Despite the simplicity of traditional direct temperature measurements, thermocouples are undoubtedly limited to a single discrete data point per experimental run, and also disturb the fluid flow field (i.e. invasive testing). It is clear that an accurate and non-invasive method of determining particle curtain temperature is required to improve the correlation of models that rely on this data.

### 2.3.2 IR Thermal Imaging

In this section, the applications of IR are described. The IR theory surrounding these applications and their operation is outlined in Section 2.4.

IR imaging detects electromagnetic energy emitted by a material and converts it into a surface temperature distribution reading [7]. An IR thermal image is produced by an array of sensors on an IR camera, which individually focus the radiation to produce a matrix of electronic signals indicative of the magnitude of radiation absorbed. Subsequent mathematical processing converts this signal into a visible coloured image by assigning colour to infrared energy levels. These generated images are termed ‘thermograms’ and are largely qualitative, focusing primarily on the relative or ‘spot’ temperatures of the imaged objects (such as in Figure 2.7). Thermal imaging therefore has been used for some time in the civil, energy and processing industries as a form of predictive maintenance and quality control [8]. Only recently has the extraction of quantitative temperature field data from industrial systems been realised.

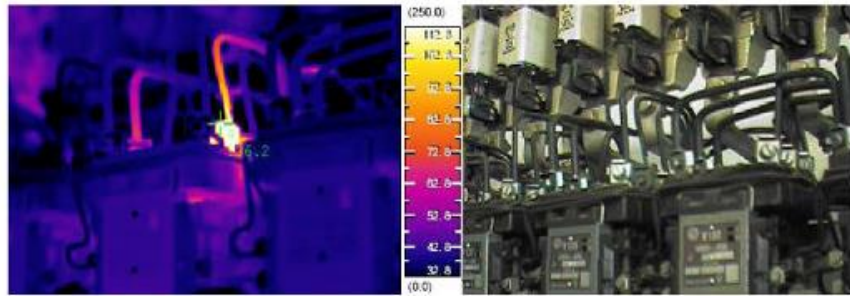


**Figure 2.7:** A faulty circuit breaker amongst an array of visibly identical devices, indicated by the temperature scale [8].

Due to the advancements of infrared systems (boasting larger pixel numbers, higher frame rates and improved thermal resolution [20]) their accessibility has increased, as well as their usage as an analysis tool in a variety of industrial applications. There are numerous benefits of non-invasive IR techniques over direct contact measurements, such as the elimination of influence on the measured object, avoiding hazardous surroundings (i.e. moving objects &/or high-temperatures), facilitating faster recording of data, and no incurred measurement errors due to the limited thermal capacity of contact thermometer [21, 22]. In what follows, applications in particulate multi-phase systems are described.

### 2.3.2.1 Fluidised Beds

Over the last six years, IR techniques have emerged as an effective method for investigating gas-solid fluidized beds [23, 24]. Previously researchers used temperature probes placed inside or on the walls of the beds [25, 26], disturbing the two-phase gas–solid flow they were intended to measure [27]. Dang et al. [10] developed a novel experimental technique for the instantaneous whole-field, non-invasive measurement of gas concentration in fluidized beds using coupled VIS and IR imagery. In their experiments a pulse generator would trigger both cameras simultaneously, and Digital Image Analysis (DIA) was applied to remove entrained particles [10]. This left only the gas phase of interest shown in Figure 2.8(d). A critical component of Dang et al.’s methodology was the use of VIS imagery to filter the IR image. This process was undertaken due to the assumed correlation of the intensity of grayscale VIS images (Figure 2.8(b)) with volume fraction.

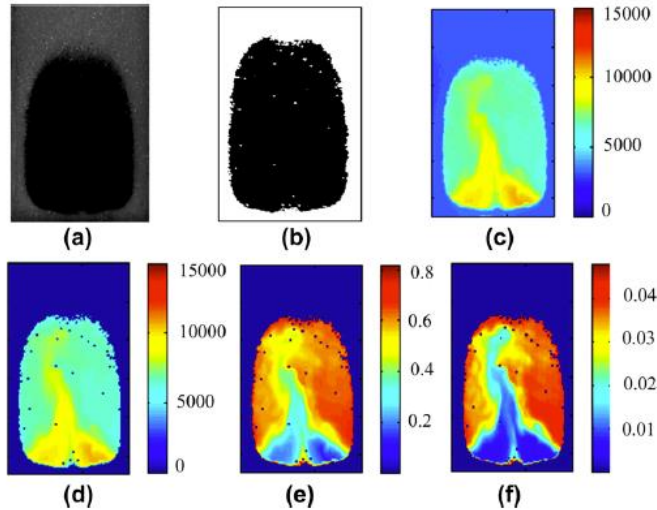


**Figure 2.8:** Steps for gas concentration measurements used by Dang et al. inside gas-solids systems via a combination of VIS and IR images: (a) VIS camera image, (b) particle detection from VIS image, (c) IR camera image, (d) particle removal by stitching VIS-IR image, (e) apparent absorbance, and (f) concentration profile [10]

Patil et al. also applied IR thermography coupled with DIA to fluidised beds and focused on obtaining the particulate temperature field at the microscopic level. The field data produced delivered insightful data sets which could be used to analyse the heat transfer mechanisms inside fluidized beds in more detail, e.g., by comparison with CFD computations [11]. Patil et al's investigation also suggested there is a temperature blurring effect that occurs in IR thermography of multi-phase particle systems. Figure 2.9(a) and (c) illustrate the blurred intermediate temperature region between the background and particle temperature. Introducing a threshold temperature eliminated the reflection of IR radiation from the background wall around the hot particles, shown in Figure 2.9(b) and (d). (For more detail on thresholding, see Section 2.5.1.) Pixels recording less than the threshold temperature were reassigned to be that of the background. This approach also filtered off partly covered pixels, as the intermediate signal intensities also represented partially covered particles. Despite good agreement obtained by alternate methods, without comparison to an accurate measure of temperature within the system, the validity of this threshold technique is uncertain. It was evident however that regions of low particle temperatures result in a failure of the direct filtering threshold approach, when particles resemble background temperatures.

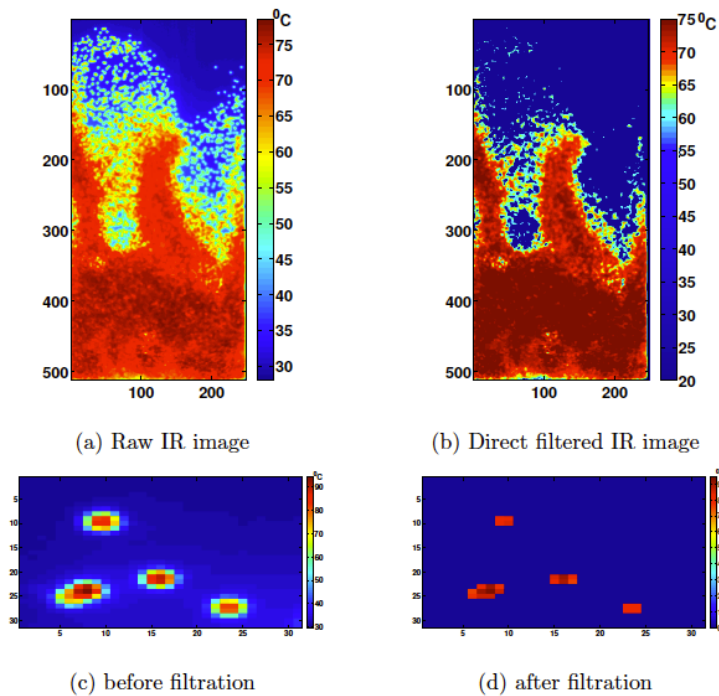


**Figure 2.9:** IR image processing steps showing the raw image (a) that was processed by direct filtering (b). The filter used corrects for wrong temperature readings at particle edges that in fact are due to partly covered pixels, by filtering these pixels off [11].

### 2.3.2.2 Particle Curtains

To date, only one investigation has applied infrared thermography specifically to particle curtains. Afshar [9] used IR thermography to measure the temperature of hot silicon particle curtains in quiescent air. Figure 2.10(a) shows the resulting 2D thermal image of a particle curtain and Figure 2.10(b) the corresponding VIS image.

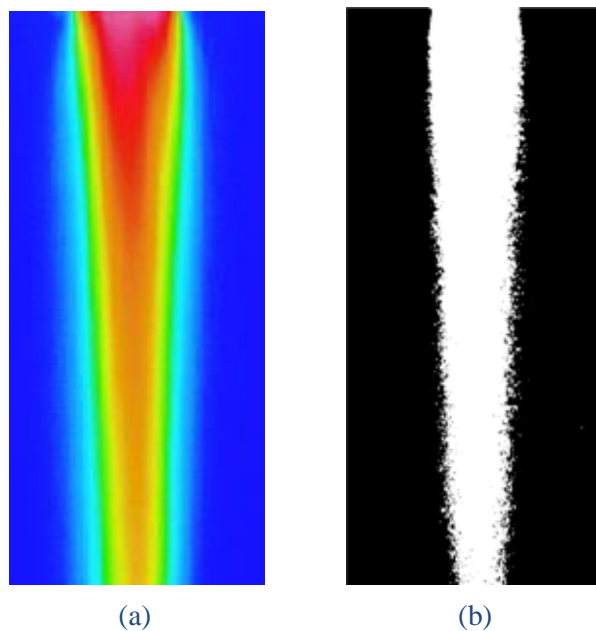


**Figure 2.10:** 2D thermal image of a particle curtain at slot width=60mm,  $d_s=290\mu\text{m}$  and  $m^\circ=0.063\text{kg/s}$

Comparisons with averaged direct thermocouple measurements (shown previously in Figure 2.6) revealed that despite inclusion of standard deviation error, infrared thermography underestimated particle temperature particularly in regions of low solids volume fraction, shown in Figure 2.11(b). Close agreement though was achieved for the smallest particles ( $290\mu\text{m}$ ), at a higher mass flow rate ( $0.15\text{kg/s}$ ) and smaller ( $20\text{mm}$ ) slot width, evident in Figure 2.11(a). This improved agreement was credited to the greater solids volume fraction given by these conditions, minimising influence of background temperature [9].

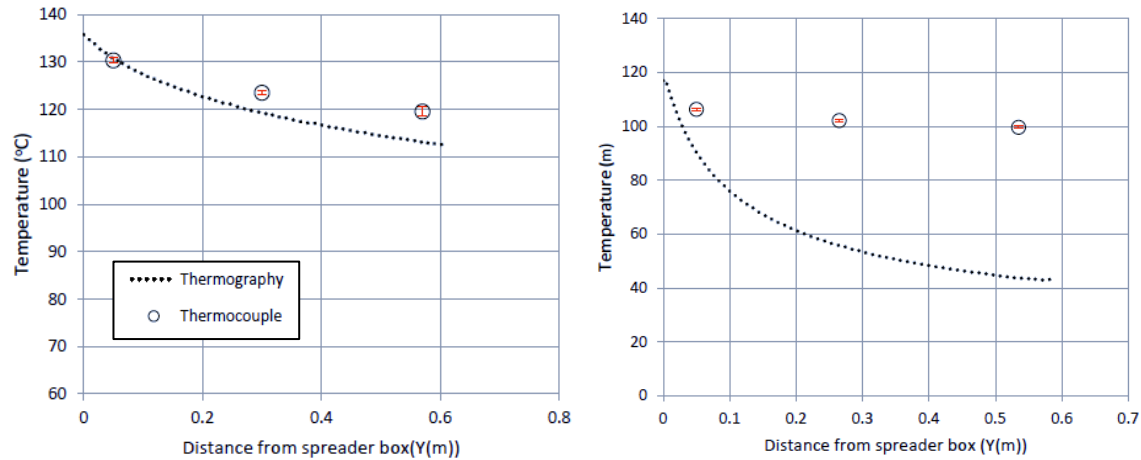


**Figure 2.11:** Thermocouple and infrared temperatures calculated from visible image photography (a)  $d_s=290\mu\text{m}$ ,  $m^o=0.15\text{kg/s}$  and slot width=20mm (b)  $d_s=610\mu\text{m}$ ,  $m^o=0.047\text{kg/s}$  and slot width=60mm. [9]

Solids volume fraction with curtain height is largely affected by curtain behavior. Specifically, particle curtains may exhibit either convergent or divergent behavior with distance from hopper exit (demonstrated by Figure 2.12), dependent on slot width [28].

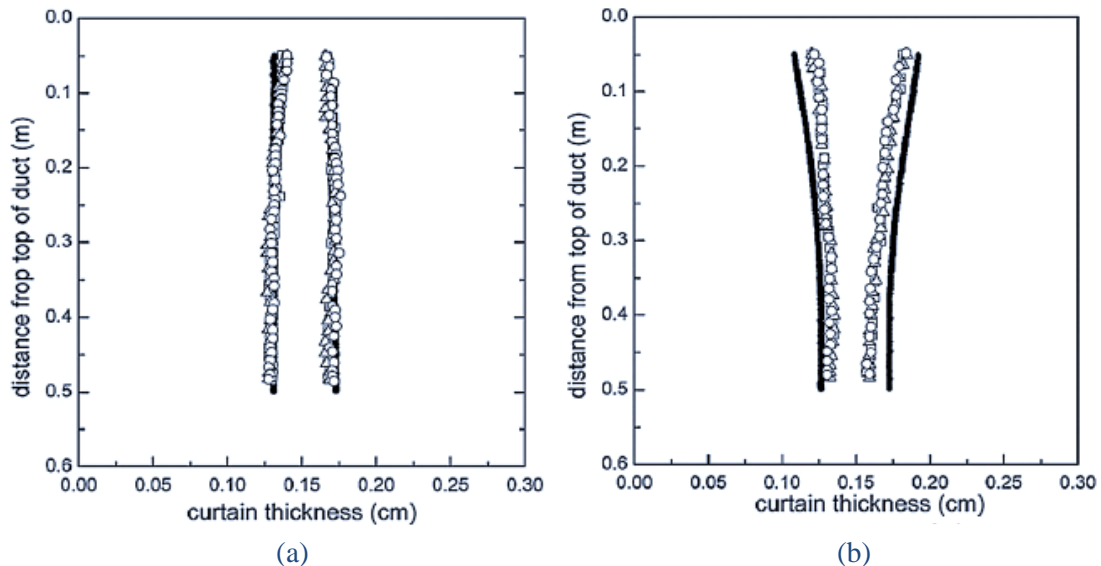


**Figure 2.12:** Particle curtain shape at small particle size,  $d_s=290\mu\text{m}$ , and (a)  $m=0.040\text{kg/s}$  with slot width=20mm, compared to (b)  $m=0.040\text{kg/s}$  with slot width=60mm [28].

IR thermography could potentially be used to measure bulk temperature in convective heat transfer systems. Due to the variety of attainable curtain behaviours, IR could therefore be used to compare the bulk heat transfer between them. Presently investigations have only focused on the effect of initial slot width on centerline curtain temperature [9]. An appreciable difference in centreline temperature versus distance from the spreader box was found for each behavior (divergent for 20mm slot width and convergent for 60mm slot width, observed in Figure 2.13). While bulk thermal effects should not be inferred from centreline temperature profiles, they suggest that the heat transfer is markedly different for each curtain shape on account of the increasing/decreasing solids pressure.

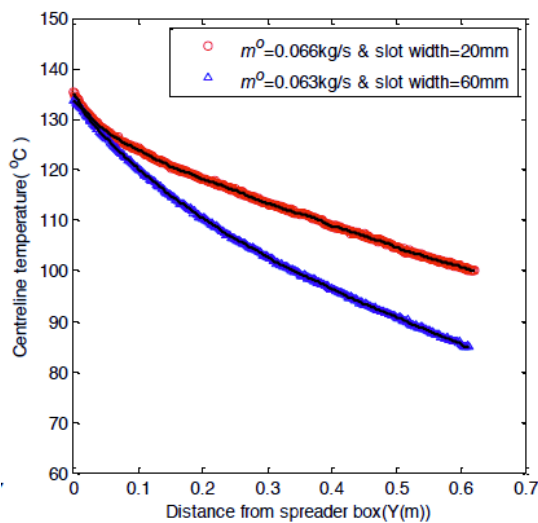


**Figure 2.13:** Effect of slot width on raw IR centerline temperatures at constant  $d_s=290\mu\text{m}$  particle size [9]

## 2.4 Infrared Theory

In order to use IR imaging correctly as well as to draw accurate, qualitative information from the system, it is first necessary to understand the applied optical physics. This section presents the underlying principles of IR thermography and provides a base level understanding of the technical procurement process involved in IR thermography.

### 2.4.1 The Electromagnetic Spectrum

The world we observe is comprised of visible light, a range that fills only a small section of the electromagnetic (EM) spectrum. Wavelengths between  $0.75\mu\text{m}$  and  $1000\mu\text{m}$  are classified as the infrared region (IR). The IR region itself is conveniently subdivided into the *near* ( $0.75\mu\text{m}$  -  $1.5\mu\text{m}$ ), *intermediate* ( $1.5\mu\text{m}$  -  $7\mu\text{m}$ ) and *far* ( $7\mu\text{m}$  -  $1000\mu\text{m}$ ) IR regions [29]. IR radiation has a greater wavelength than visible light, evident from Figure 2.14, allowing it to propagate through gas and dust in space with less scattering and absorption [30]. The emission and absorption of IR radiation occurs through the rotations and vibrations of chemically bonded atoms or groups of atoms [31]. The resulting charge displacement releases ‘EM radiation’ (i.e. photons). All bodies with a temperature above absolute zero emit EM radiation as a wave. Like sound waves, EM waves obey the law of superposition [32]; two EM waves on a collision course will either constructively or destructively interfere when they meet, then exit that region unchanged from their original shape and direction.

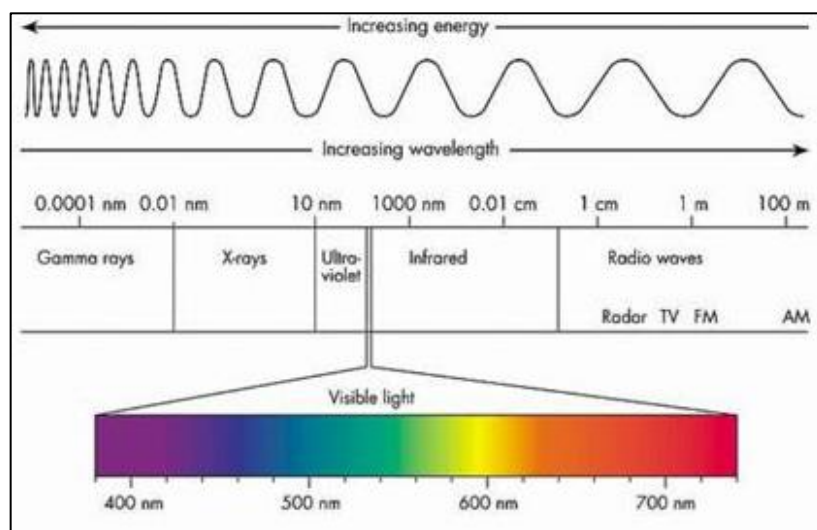


**Figure 2.14:** Location of the infrared region on the electromagnetic spectrum [33]

### 2.4.2 Blackbody Radiation

A blackbody describes an ideal surface wherein all incident radiation is absorbed. By this definition, no surface can emit more energy than a blackbody at the same temperature [30]. These bodies obey Planck's law, which states that the total volume of energy radiated from its surface increases as a function of temperature [8]. Equation (1) outlines this law.

$$M(\lambda, T) = \frac{c_1}{\lambda^5 (e^{c_2/\lambda T} - 1)} \quad (1)$$

where

$M_{\lambda,T}$  – spectral radiant emittance per unit wavelength and unit area [ $W \cdot \text{cm}^{-1} \cdot \mu\text{m}^{-1}$ ]  
 $c_1$  – first radiation constant [ $\text{cm}^{-2} \cdot \mu\text{m}^{-4}$ ]  
 $c_2$  – second radiation constant [ $\text{cm}^{-2} \cdot \mu\text{m}^{-4}$ ]  
 $\lambda$  – wavelength [ $\mu\text{m}$ ]  
 $T$  – absolute temperature [K]

This relationship is depicted graphically in Figure 2.15. As the graph suggests, the spectral emittance of a blackbody increases at all wavelengths when object temperature increases. Additionally, peak blackbody radiation for room-temperature objects occurs in the intermediate to far IR region.

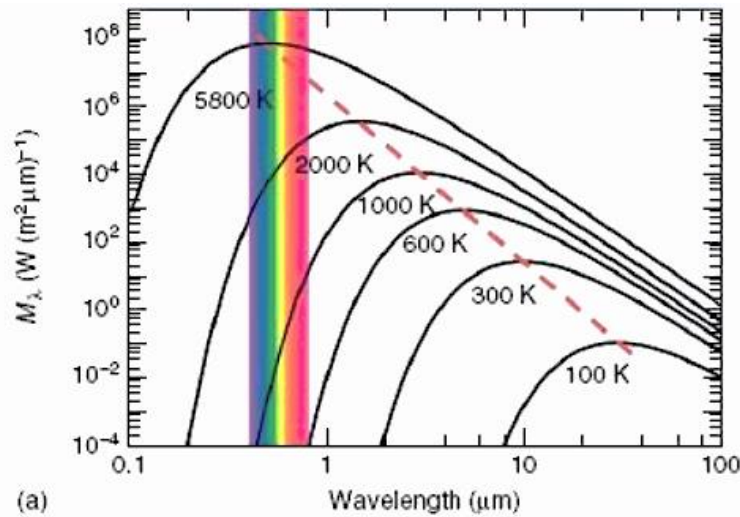


**Figure 2.15:** Spectral emittance of a blackbody on a logarithmic scale, where the coloured region represents the visible wavelengths [34]

This graph may be used to determine the total IR radiation emitted by a black body as a function of absolute temperature of that body, as the emitted radiation from a surface corresponds to the area under its radiation curve. This is described by Stefan-Boltzmann's Law below (Equation (2)), which computes the integral of Equation (1).

$$M(T) = \int_0^{\infty} M(\lambda, T) \cdot d\lambda = \sigma T^4 \quad (2)$$

where

$M_T$  – spectral radiant emittance per unit area [ $W \cdot cm^{-1} \cdot \mu m^{-1}$ ]  
 $\sigma$  – Stefan-Boltzmann constant [ $5.6705 \cdot 10^{-12} W \cdot cm^{-2} \cdot K^{-4}$ ]

The result demonstrates that the emitted radiation increases with the fourth power of temperature. It is this property which thermographic imaging exploits to convert wavelengths previously invisible to the naked eye into a visible image. However, accuracy of surface radiation measured by an IR camera is dependent on a number of other parameters, including emissivity, viewing angle and detector type.

### 2.4.3 Emissivity

Material emissivity is a measure of the ratio of the emitted radiation by a material's surface ( $M_\lambda$ ) to that which is emitted by a blackbody at the same temperature ( $M_{b\lambda}$ ). This is described by Equation (3). The spectral emissivity of a blackbody may be observed in Figure 2.16, contrast with graybody and real surface emission spectra.

$$\varepsilon(T) = \frac{M_\lambda(T)}{M_{b\lambda}(T)} \quad (3)$$

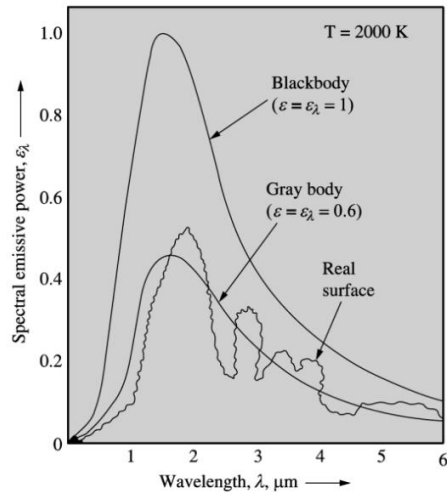


**Figure 2.16:** Comparison of spectral emission for black, gray and real surfaces [35]

From Equation (3), emissivity is thus a measure of absorbance ( $\alpha$ ), as stated by Kirchoff's Law.

$$\varepsilon = \alpha \quad (4)$$

Incident radiation, like light, can be absorbed ( $\alpha$ ), reflected ( $\rho$ ) or transmitted ( $\tau$ ). Hence, the

sum of these three parameters as fractions of incident radiation equates to one. Substitution of Equation (4) yields:

$$\varepsilon + \rho + \tau = 1 \quad (5)$$

Therefore as reflectance and transmittance of a surface increase, emissivity will decrease. As shown in Figure 2.16, spectral emissivity is a complex function of wavelength for some real surfaces [35] due to material molecular structure and surface characteristics. In reality, it is more appropriate to assume surfaces are a ‘graybody’ (i.e. constant emissivity with temperature), however this may have implications in IR thermal imaging as small variations in emissivity can cause large errors in temperature readings [34]. The spectral emissivity, transmittance and reflectance of glass are shown in Figure 2.17. Transmittance is practically zero in the 5-15 $\mu\text{m}$  wavelength range, with emissivity and reflectance remaining fairly constant (i.e. glass is analogous to a graybody in this range).

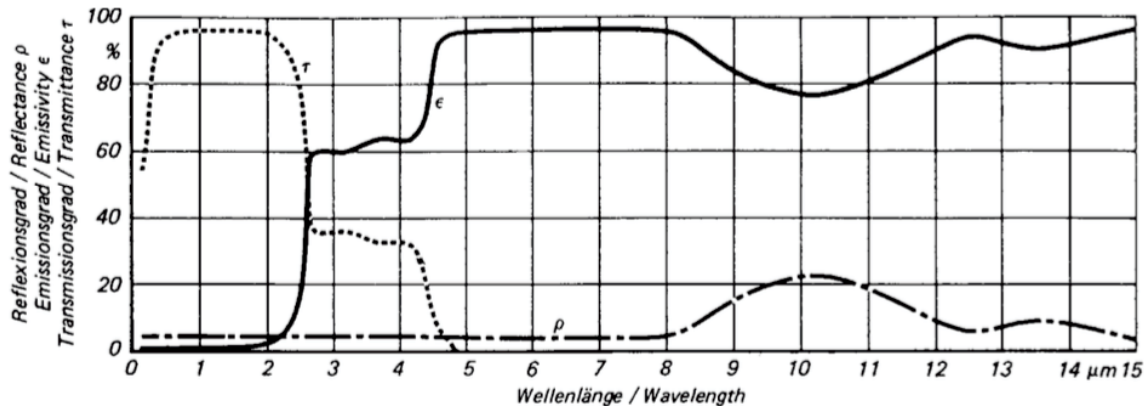
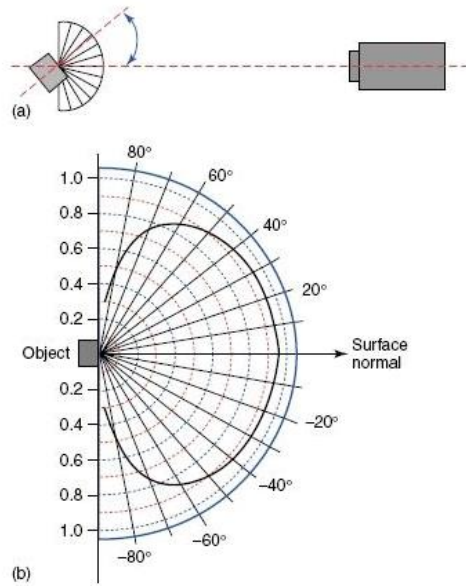


Figure 2.17: Variation of glass spectral properties with wavelength [22]

Viewing angle also has the potential to affect emissivity. An object observed from a direction normal to its surface will emit more radiation than when observed at oblique angles. As reflectance increases at oblique angles, emissivity will decrease as described by Equation (5) and observed in Figure 2.18. Experiments suggest that the recorded emissivity of a flat surface is constant from the normal direction from  $0^\circ$  to roughly  $40^\circ$  (shown in Figure 2.18) [34].



**Figure 2.18:** (a) A non-conducting ‘hot’ object to be studied is placed with its surface normal facing  $90^\circ$  to the IR camera lens. Then, measurements of the emitted radiation are recorded as a function of angle while rotating the object. (b) Actual surface temperature measured by contact thermometry, and emissivity value in the IR camera software is altered until the real temperature is shown (emissivity for correct temperature value given on the y-axis) [34].

#### 2.4.4 Infrared Detectors

The IR detector acts as transducer to convert radiation into electrical signals. The electrical impulses from all micro detectors of the IR camera’s array are stored, and subsequent mathematical processing converts this array of data into a thermogram by assigning a colour to each IR energy level [36]. The properties of IR cameras that affect the measured object temperature most significantly include response time and field of view (FOV). The FOV is the area seen by the camera at a given distance from an object [34]. The greater the FOV, the larger the minimum detectable size (i.e. pixel dimensions, shown in Figure 2.19).

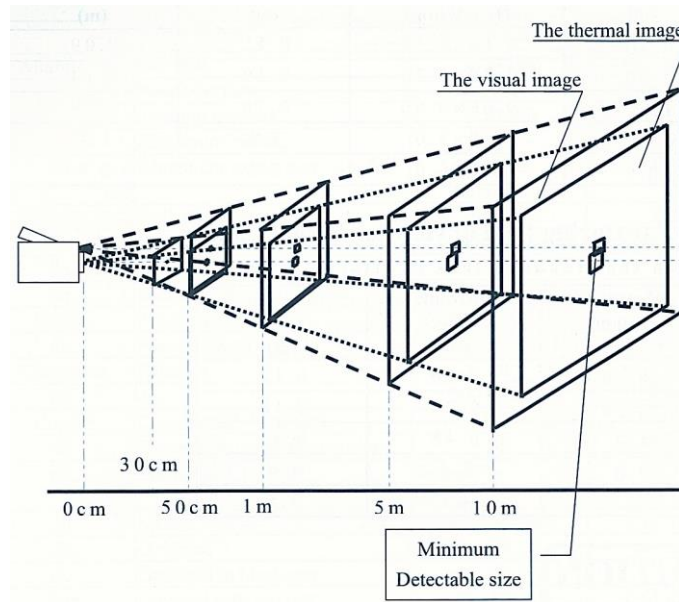


**Figure 2.19:** Effect of FOV on minimum detectable size for an IR camera [37]

The wavelength range of an IR camera specifies the measurable spectral radiant emittance (i.e. the limits on the integral of Equation (2)). Ideally, IR cameras should measure over the widest wavelength range possible to gain the greatest signal from the target [22]. However, as outlined in Section 2.4.4 varying physical properties of surfaces with wavelength may reduce this advantage and produce erroneous readings. In accordance with Stefan-Boltzmann's law, the electric signal of a detector may be expressed as follows.

$$U \sim \varepsilon T_{obj}^4 \quad (6)$$

Considering ambient radiation as well as self-radiation, the detector signal may be expanded to incorporate these influences, as shown in Equation (7) [21]. Here the exponent  $n$  is dependent on the wavelength. Notice the dependence of emissivity on the detector signal; if the surface of a body is assumed to have an emissivity of one, the influence of ambient temperature is eliminated.

$$U = C \cdot [\varepsilon T_{obj}^n + (1 - \varepsilon) \cdot T_{amb}^n - T_{Pyr}^n] \quad (7)$$

where

- $U$  – detector signal [ $Wm^{-2}$ ]
- $T_{obj}$  – object temperature [K]
- $T_{amb}$  – ambient temperature [K]
- $T_{Pyr}$  – camera temperature [K]
- $n$  – wavelength dependent constant ( $\sim 2-14$ )
- $C$  – device specific constant

## 2.5 Image Analysis

Image analysis is an essential tool for processing IR & VIS image data, and is also required for coupling CFD model and experimental data.

### 2.5.1 Image Thresholding

Thresholding within image processing is a simple yet effective tool to separate objects of interest in the foreground from the background [38]. The visible effect of applying thresholding is conversion of the foreground to white and the background to black, or visa versa. All images are essentially matrices comprised of stored numbers. Mathematically, the grayscale value recorded (usually between 1 and 255) in each pixel is converted to a binary value: either 0 or 1. This is achieved by selection of a minimum ‘threshold’ intensity. Any value less than this threshold intensity is set to be the background, providing the user with control over the differentiation between background and foreground.



**Figure 2.20:** Processed VIS images of a particle curtain with various threshold intensities

This technique can be applied to a variety of image types, including visible and IR images. As depicted in Figure 2.20, the threshold intensity selected can significantly affect the foreground selection. In such circumstances, comparison with the VIS image or application of a numerical threshold computation can aid in the decision-making process. A commonly applied and effective method of thresholding is Otsu’s method, a form of automatic clustering based image processing [38]. Selection of the threshold value is accomplished following an assessment of the images histogram. An example histogram is shown in Figure 2.21. Assuming a bimodal histogram distribution, Otsu’s method selects the best threshold value to maximise the variance between the

background mode and the feature mode [39, 40].

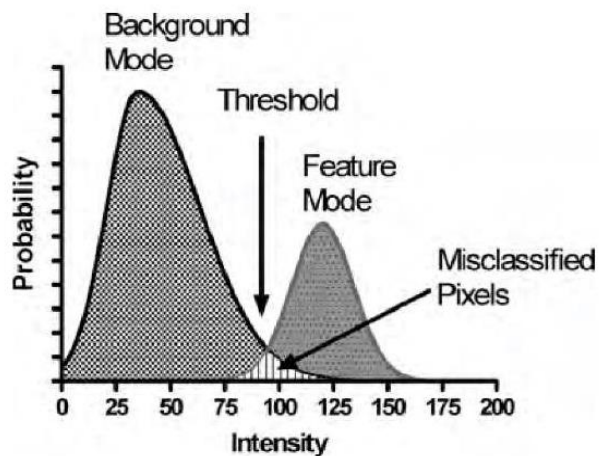


**Figure 2.21:** Ideal biomodal histogram, showing the misclassification of pixels following calculation of the level threshold by Otsu's method [39]

### 2.5.2 Visible Image Analysis

VIS imagery is highly beneficial in the determination of solid volume fraction. Pixel intensities are generally assumed to be directly proportional to the solid volume fraction, particularly at low volume fractions and for short depths of field [9, 41]. Two-dimensional solids volume fraction data is obtained from VIS imagery by conversion of the raw image to grayscale, and subsequent normalisation of intensities between 0 and 1.

VIS image capture is also reported by many studies as the most effective method of locating curtain edges [9, 42]. Wardjiman et al. [42], took visible images using a digital high-speed camera of a particle curtain falling in horizontal gas flow. Figure 2.22 shows the blue ‘tracked’ edges of the curtain that were determined by employing a high-speed digital camera to track particle trajectories frame-by-frame. Boundaries may also be located simply by sight.

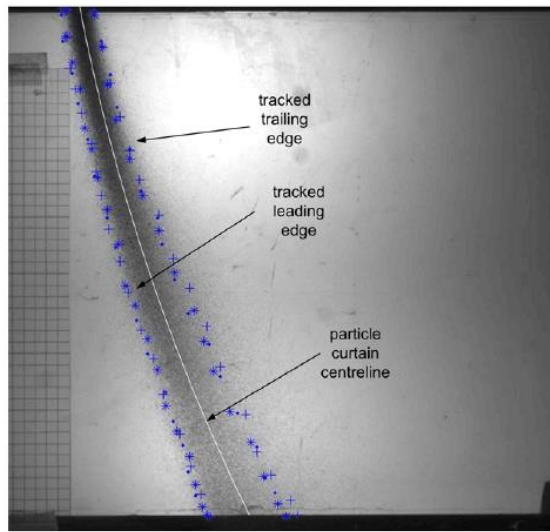


**Figure 2.22:** Image of particle curtain captured at the wall of duct by high-speed camera [42].

A methodology presented by Afshar [9] using an approach widely adopted in image analysis [17] determines the location of particle curtain edges by manipulation of two-dimensional volume fraction data. Using a volume fraction contour field (such as in Figure 2.23(a)), the variation in solids volume fraction ( $\alpha_s$ ) gradient at various heights ( $\frac{\partial \alpha_s}{\partial x}|_y$ ) is plotted (Figure 2.23(b)). The maxima describing the sudden change in volume fraction corresponds to the curtain edge.

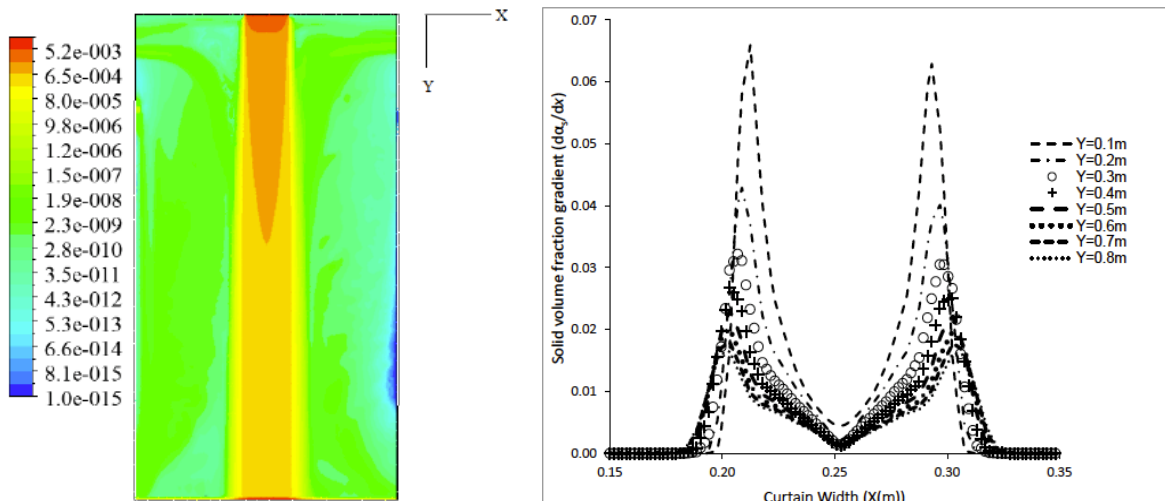


**Figure 2.23:** (a) Solid volume fraction contour of a particle curtain determined by CFD, & (b) solid volume fraction gradient at various heights of the curtain's middle plane [9]

### 2.5.3 IR Image Analysis

IR thermal images may be converted to a two-dimensional array of temperature, which can then be used to compute bulk particulate temperature. Recently analyses of IR images have involved the use of a threshold temperature to remove background reflection, reassigning pixels recording less than this temperature to be equal to the background temperature [11]. To establish the threshold value, a temperature closer to the average particle temperature than to the background must be selected.

Two-dimensional temperature field data has also shown potential in locating particle curtain edges, although comparison to VIS image edge detection methods have not been shown. Afshar [9], using a similar method as described for VIS imagery in Section 2.5.1, numerically differentiated curtain temperature profiles to locate the maxima (Figure 2.24(a)). A “Gaussian Kernel” function ( $\text{Sigma}=1$  and  $\text{Kernel size}=\text{Sigma}\times 6$ ) was used to smooth the raw temperature profiles. After correcting for symmetry, Afshar overlaid the maxima with the original IR image (Figure 2.24(b)) for ease of comparison with CFD profiles.

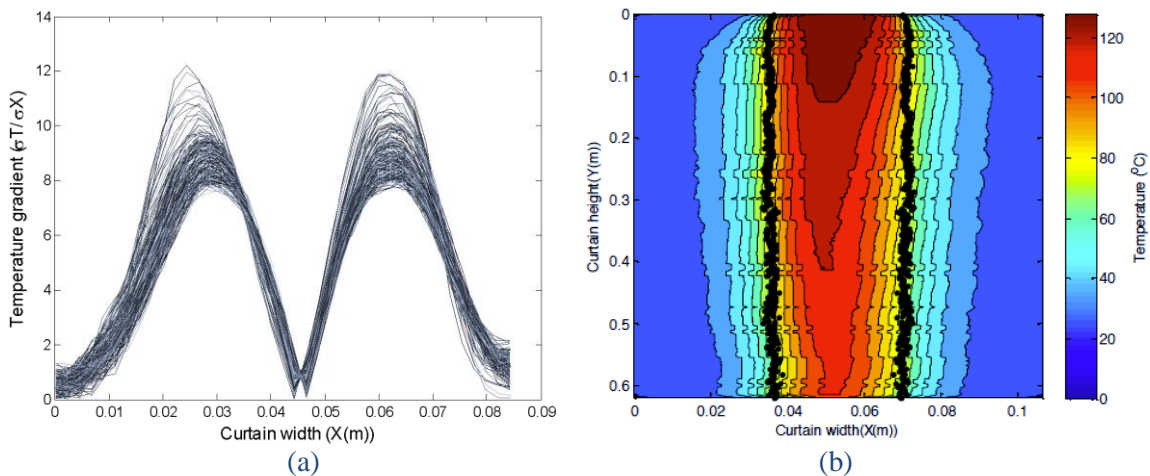


**Figure 2.24:** (a) Temperature gradient profiles and (b) overlaid edges on thermal image,  $d_s=290\mu\text{m}$ ,  $m^*=0.066\text{kg/s}$  and slot width=20mm [9]

## 2.6 Conclusions

The literature review has summarized temperature measurement techniques, emphasizing the applications of particle curtains and need for improved methodologies of acquiring properties. The review identified the limitations of discrete temperature measurement contrasted by the advantages presented by the use of IR thermography. Furthermore, two-dimensional field data could be more easily integrated with CFD modeling. Despite the advantages, extraction of

quantitative temperature field data from IR imaging in two-phase systems is a relatively new concept, and new techniques for image analysis are necessary. A review of applied optical physics has highlighted key experimental factors and material properties to be considered when obtaining accurate thermographical readings. A thorough understanding of these considerations will help to minimize the differences between IR and direct temperature measurement readings and validate IR results. Critically, it has been shown that close agreement of IR with direct temperature measurements is achieved at high solids volume fractions, but fails at low solids volume fractions when using larger particles at reduced mass flow rates.

### 3.0 Methodology

Based upon the conclusions of the literature review, this chapter presents a description of the methodologies used to generate a hot particle curtain with consistent properties. Also described are the methods employed to collect visible images, IR thermal images and direct temperature measurements of the particle curtain system.

The methodologies of this thesis were divided into four distinct phases, summarized in Figure 3.1. Equipment and apparatus was optimised in Phase 1, predominantly by mass flow rate tests performed on a variety of available spreader box components. The goal of these tests was to obtain a divergent and convergent curtain with near-identical mass flow rate to isolate volume fraction effects. The focus of Phase 2 was ensuring the experimental methodology was consistent and produces reliable data. Preferential camera scaling and alignment techniques were also investigated. Phase 3 involves the collection of IR images, VIS images and direct temperature measurements for the converging and diverging curtain. An experiment to compare the bulk curtain heat transfer between each curtain behavior was also undertaken using simple thermochemistry. Ultimately, Phase 4 analyzes the collected images and direct temperature data to assess the strengths and limitations of IR thermography.

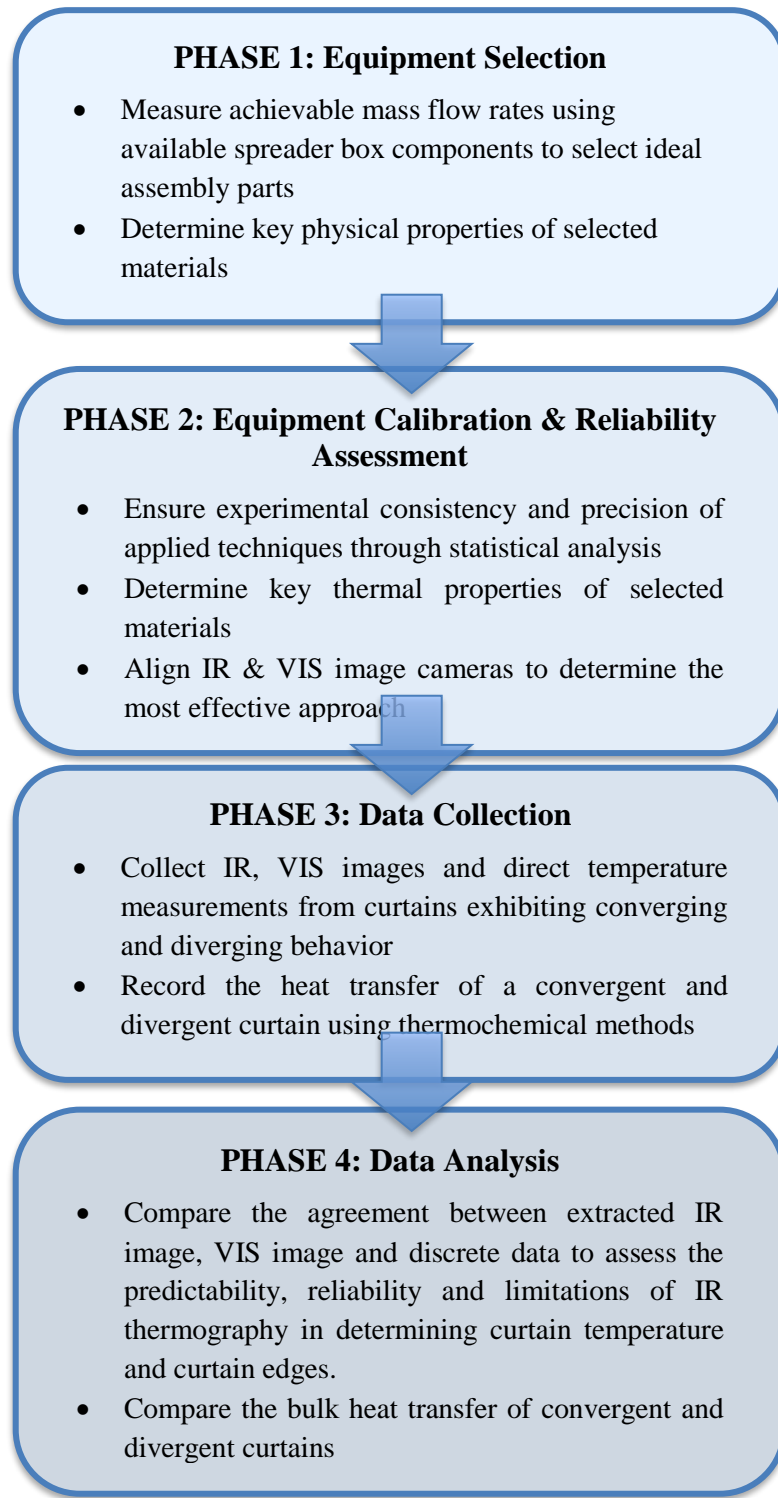


*Figure 3.1: Methodology Overview*

### 3.1 Equipment Selection

This section describes the general equipment used in this thesis and justifications for their selection. Equipment presented includes the apparatus, software and camera specifications.

#### 3.1.1 Particulate Properties

Silica beads, which are frequently used in particle curtain experimentation [6, 9, 28, 43], were selected as the particulate medium. They are favored due to their availability in consistent size and shape, and preferable thermal characteristics. Specifically, silica emissivity is roughly constant over the 8-13 $\mu\text{m}$  wavelengths boundaries imposed by the IR camera (outlined in Section 3.1.4.1). The white glass beads also provide a high level of contrast with black backgrounds to aid in VIS image thresholding.

As concluded from the literature review, it is easier to compare CFD and direct temperature data when a narrow particle size is investigated. Furthermore, smaller sized particles produce the best agreement with CFD modeling and direct temperature measurements. The smallest available particle available from Potters Industry® was therefore used in all further experiments. A preliminary particle size distribution analysis was performed on the smallest available silica beads. This was accomplished using a Malvern Mastersizer 3000, ideal for nanometer to micrometer particle sizes. A risk assessment for this procedure is included in Appendix 1. The Mastersizer determined the volume diameter of the particles using laser diffraction by analysing the intensity of the scattered light passing through the dispersed sample [44]. Ultrasonic vibrations were applied to reduce agglomeration, resulting in the symmetric particle size distribution curve shown in Figure 3.2. The mean particle size was determined to be 257 $\mu\text{m}$ , exhibiting a standard deviation of 89.7 $\mu\text{m}$  with low skewness of 0.683 (moderately to the left)

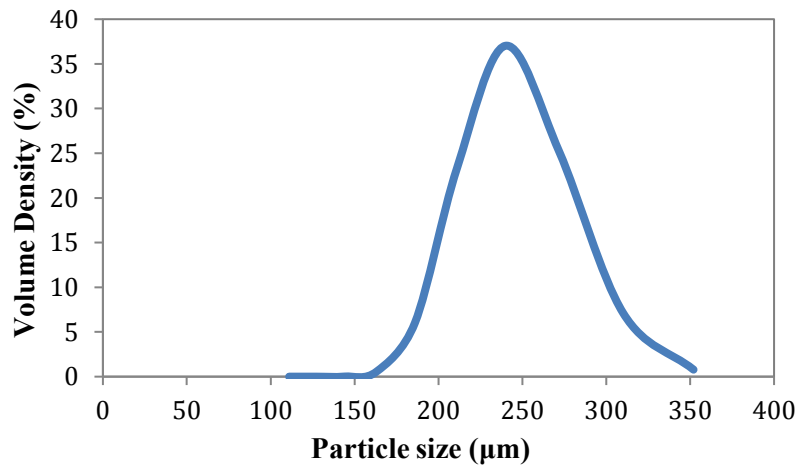


**Figure 3.2:** Particle size distribution produced by Malvern Mastersizer 3000, giving mean particle diameter,  $d_s=257\mu\text{m}$

### 3.1.2 Experimental Apparatus

The experimental apparatus used in this thesis was fully designed and fabricated in house for Afshar's [9] investigations into experimental characterization of hot particle curtains. The set-up is shown schematically in Figure 3.3. It consists of an insulated wedge hopper, black background, spreader box, perforated plates, wire mesh screens, a scale indicator, oven, IR camera, high speed VIS image camera and laptop. All experiments for this thesis were undertaken in a fully enclosed laboratory. This room was solely illuminated by artificial light and contained an ambient air velocity of 0m/s. The initial particle temperature was set to be 120°C due to oven limitations. The hopper, containing approximately 4.2kg of silica beads, was placed in an oven and heated to this temperature prior to experimentation.

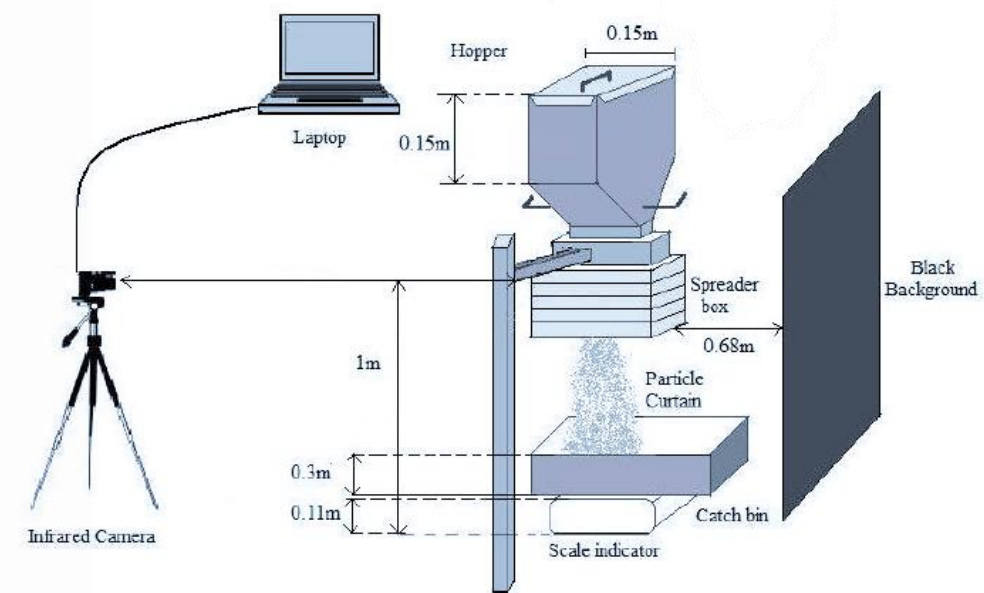


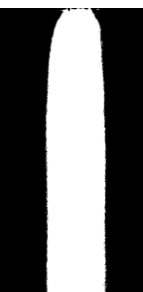
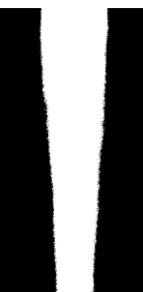
**Figure 3.3:** Side view of experimental apparatus with relative dimensions (Afshar [9])

#### 3.1.2.1 Slot Width & Spreader Box Assembly

As highlighted in the literature review, converging and diverging particle curtains can be generated by varying slot width [28]. Varying slot width will change the curtain behavior to exhibit different initial solid volume fractions. That is, particles are more closely packed at the outlet of a smaller slot width compared to a wider one. To isolate the influence of volume fraction effects, two unique slot widths producing the same mass flow rate were selected: a 20mm x 160mm and 60mm x 160mm slot width (hereafter called 20mm and 60mm respectively). These metal casings (based on designs presented by Dawson et al. [45]) generated a uniform particle curtain. To obtain the same mass flowrate from the 20 and 60mm slot widths, the flowrate was manipulated by changing the perforated plates enclosed within the spreader box

casing (see Appendix 3). Flow rate was influenced by the number of perforated plates, the number of holes on the plate, and the hole diameters. New plates were constructed to obtain close flow rates between the 20mm and 60mm slot widths. Additionally, wire mesh was included in the casing (to improve uniformity at the slot width exit) and wire railings (to better spread particles into the wider 60mm slot width). The final equipment pieces selected are listed in Table 1. Estimated flow rates were determined by tests run at ambient conditions by fitting the hopper (full of silica beads) into the spreader box, then manually opening the valve fully. For specific dimensions of the spreader box assembly and specification of the perforated plates  $\alpha$  and  $\beta$ , see Appendix 3. Repeatability of the achieved flow rate is outlined in Section 4.1.2.

**Table 1:** Spreader box assembly components for nominated curtains

Slot Width	20mm	60mm
Curtain Behaviour	Divergent	Convergent
<b>Curtain Appearance</b>		
Mass flow rate (kg/s)	0.160	0.166
Perforated Plates	$1 \times \alpha$ plate	$1 \times \beta$ plate
Wire Mesh	20mm wide mesh	60mm wide mesh
Rails	nil	yes

### 3.1.3 Direct Temperature Measurement

#### 3.1.3.1 Sampling Cups

Direct curtain temperature values were taken with a device of similar design to that used by Hruby et. al [16], Wardjiman and Rhodes [42] and Afshar [9]. The device is composed of a T type bead thermocouple (having an accuracy of  $\pm 0.1^\circ\text{C}$ ) fitted into a small cup with a hole in the base (Figure 3.4). A data logger thermometer (SE-378) was then connected to the thermocouple probes to store the temperature data on the laptop at one-second intervals. Based on recommendations suggested by Afshar [9], a number of changes were made to improve accuracy. Eight new sampling cups were constructed from the hemispheres of melon-ballers, each with a unique hole-size in their base tailored for specific mass flow rates (i.e. curtain sampling location).

The new smaller diameter cup shown in Figure 3.4 minimized the dead zone hold-up around the inner surface and improved the precision and accuracy of measurement.

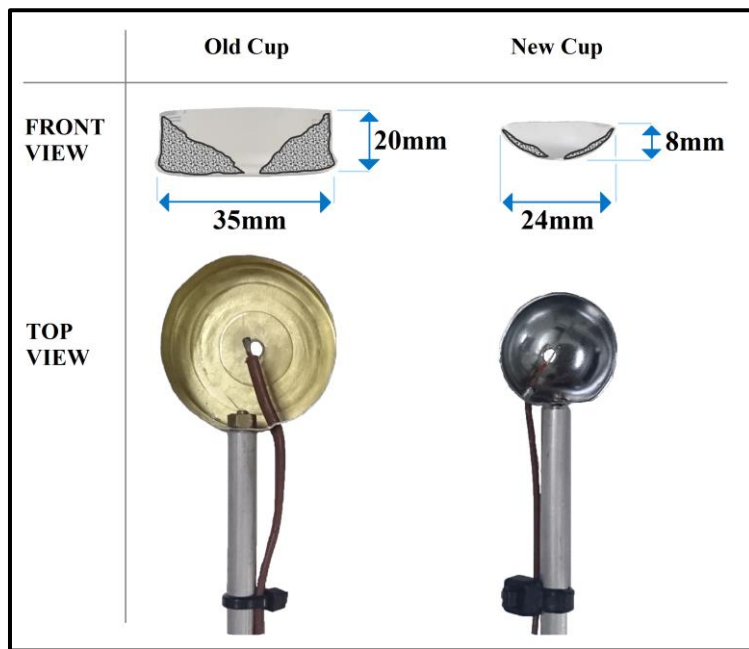


**Figure 3.4:** Comparison between the old thermocouples used by S. Afshar [9] and the new cups developed in this thesis

Sampling cup hole-size was dependent on the height at which samples were taken and was gauged by trial and error. Correct selection of hole-size in the sampling cup was found to be pivotal in achieving temperature stabilisation. This was because a sufficient mass hold-up in the sampling cup was required to ensure a fast thermocouple response (Figure 3.5). If any direct thermocouple temperature trend did not indicate a good mass hold-up, the test was repeated at the same height with a smaller cup size.

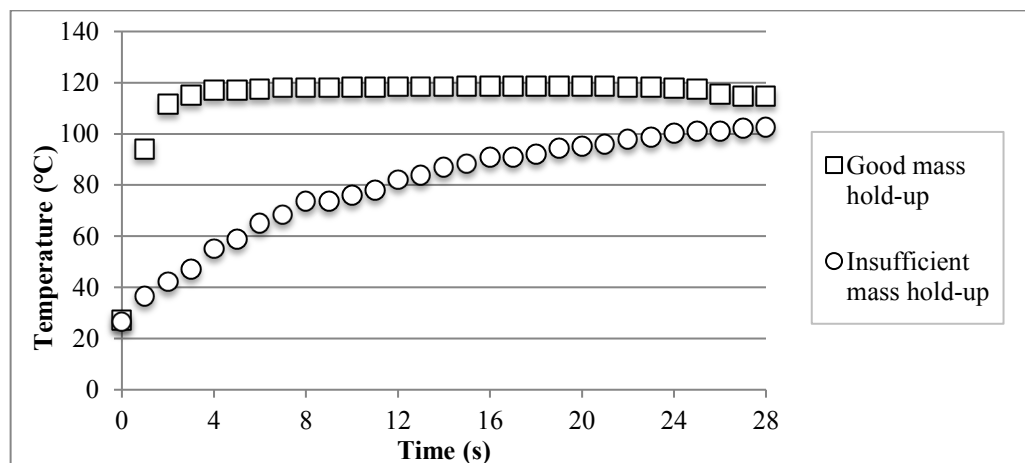


**Figure 3.5:** Comparison of two sampling cup hole sizes, one too wide (i.e. insufficient hold-up)

Alignment of the sampling cup with respect to the spreader box is described in Figure 3.6. All thermocouple measurements were taken with the sampling cup centered over the frontal width (for centerline temperatures). As depicted in the side view, the cup's center was aligned with the edge of the mesh screen, 2.2cm from the spreader box front. This point had important implications in subsequent camera focusing, and is hereon referred to as '*zero depth*'. The vertical distance from the spreader box exit was taken from the base of the rod nearest the cup, which aligned with the resting height of the thermocouple bead tip.

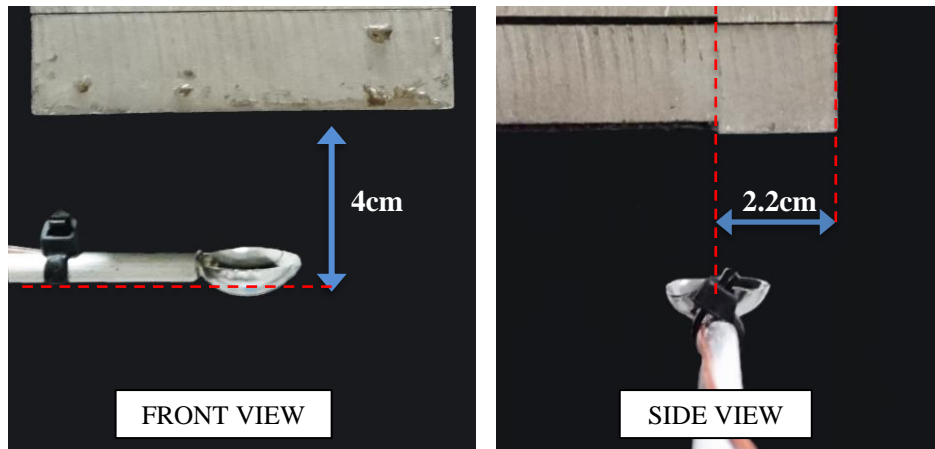


**Figure 3.6:** Sampling cup alignment with spreader box slot opening, for a height of 4cm and depth of 0cm.

### 3.1.3.2 Sampling Locations

To assess the ability of IR thermography to capture particle curtain temperature, thermocouples recorded temperature directly at nine locations below the spreader box exit, given in Figure 3.6. Data was collected using a single thermocouple per run, and was undertaken for both the 20mm and 60mm slot width. In addition to direct measurements with curtain height, a series of samples were taken with curtain depth at the top and bottom of the curtain. This was vital for comparison with IR spot temperatures due to the potential of IR imaging to integrate surface temperature readings from particles at greater depths in the curtain with those in the forefront. Curtain temperature was recorded at five discrete depths within the 20mm and 60mm slot width curtain. This was undertaken at both a vertical distance of 4cm and 60cm below the spreader box.

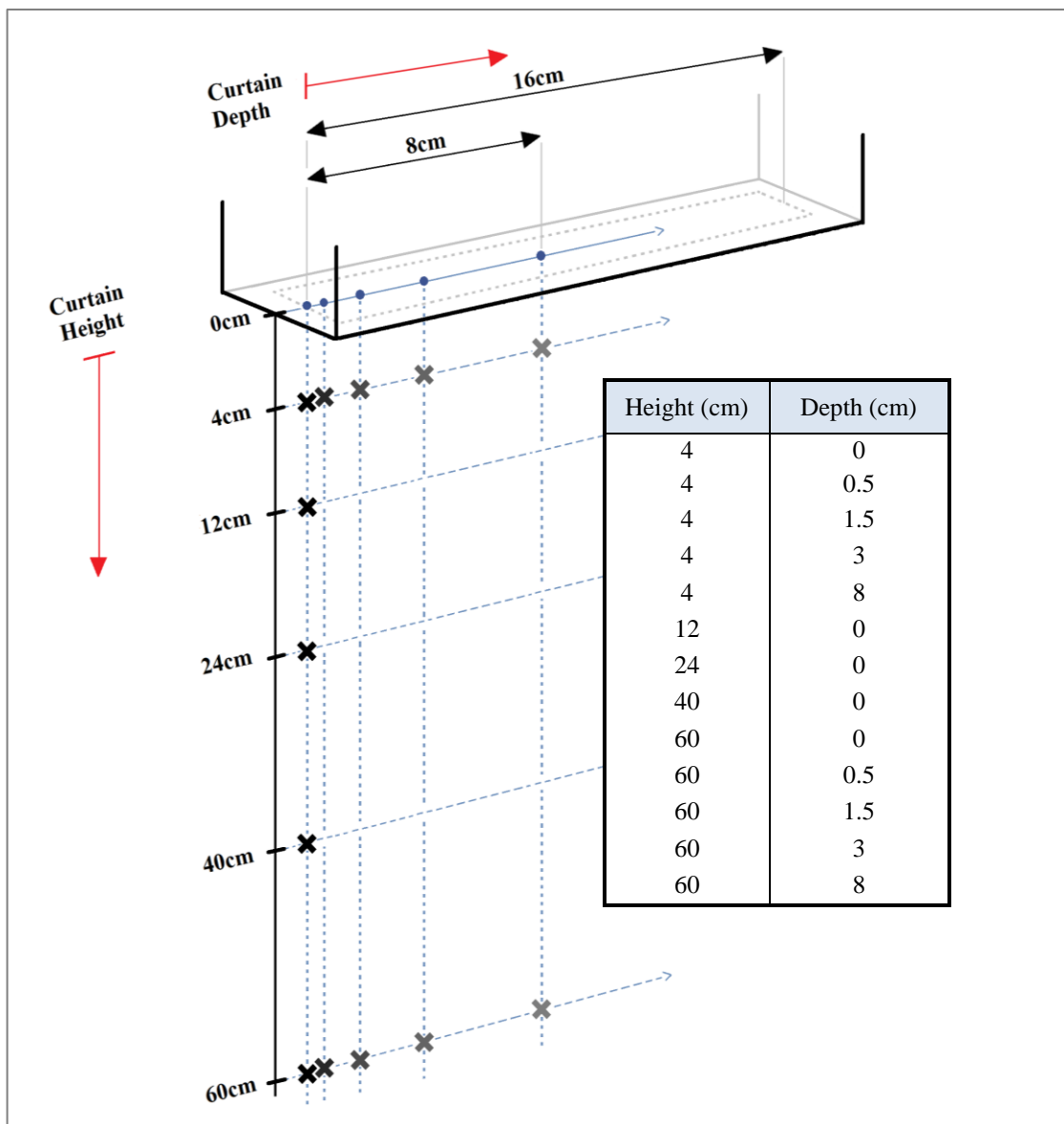


**Figure 3.7:** Sampling locations for assessing IR and discrete temperature agreement (curtain height axis not to scale). See Appendix 3 for more detail on spreader box dimensions. 33

### 3.1.3.3 Thermometer Equilibration

To prevent misalignment of the various direct temperature measurement devices, all were placed side-by-side and left to equilibrate in an ambient environment. Their relative deviations were recorded such that all subsequent measurements could be normalized.



**Figure 3.8:** Testo 610 humidity sensor (left) with a temperature reading greater than that of three attached thermocouples to the data logger thermometer (SE-378) (right)

### 3.1.4 Imaging

For both the 20mm and 60mm slot width, IR and VIS imagery imaging tests were performed independently to mitigate parallax error. The converging and diverging curtain behavior induced by these slot widths contained regions of high and low solids volume fraction, providing a good basis on which to assess the various curtain edge detection methods of IR and VIS imagery.

#### 3.1.4.1 IR Camera Imaging

To capture thermal images of particle curtains, a NEC Avio H2600 Series IR camera, having properties of Table 2, was employed.

**Table 2:** Specifications of NEC Avio H2600 Series IR camera

<b>Distance from Spreader Box</b>	2.79m
<b>Measuring Range</b>	0°C ~ 500°C
<b>Min Detectable <math>\Delta T</math></b>	0.12°C at (30°C)
<b>Resolution</b>	640×480 pixels
<b>Spectral Range</b>	8-13μm
<b>Frame Rate</b>	1/30 sec (i.e. 0.033 sec intervals)
<b>Measurement Accuracy</b>	±2°C or ±2% (reading)
<b>Applied Temperature Corrections</b>	Ambient, humidity, background, object distance and emissivity (0.10 to 1.00)

Prior to IR image capture, an in-camera reflection calibration and background compensation procedure was performed. Steps to achieve this are outlined in the NEC Avio H2600 Series Operation Manual [37]. In-camera calibration was followed by manual adjustments to the atmospheric temperature and humidity within the IR camera (for the cameras automated compensation value). These readings were acquired using a Testo 610 humidity sensor having an accuracy of  $\pm 2.5\%$  RH and  $\pm 0.5^\circ\text{C}$ . To input the thermographic images to the laptop, an IEEE 1394 cable was connected between the IR camera and the laptop IEEE 1394 port. Avio NEC NS9500 InfRec Analyzer Professional software then recorded the thermal images in SVX file format. Temperature data was captured in SVX file format and then exported to an excel spreadsheet before MATLAB processing.

### **3.1.4.2 VIS Camera Imaging**

A Nikon D80 camera will be used to capture 2D pixel intensity of particle curtains. The settings selected for VIS image capture are described in Table 3. Settings were selected to provide optimal exposure of the image in the absence of an applied flash, while maintaining a shutter speed small enough to produce a non-blurred image. Upon initial set-up, a lighting calibration procedure was undertaken (outlined in Section 3.3.2). Lighting equipment in the form of six 500W spotlights on tripod stands were placed around the curtain to give an even light distribution. This calibration process is outlined in Section 3.2.5.2. Captured images were saved to an SD card in JPEG format and imported to the laptop for MATLAB processing following experimentation.

**Table 3:** Specifications and settings of Nikon D80 VIS image camera

<b>Distance from Spreader Box</b>	1.30m
<b>Resolution</b>	3872×2592 pixels
<b>Shutter Speed</b>	1/60 sec
<b>Focal Length</b>	18mm
<b>Aperture</b>	3.5
<b>Mode</b>	Continuous operation, grayscale

## 3.2 Experimental Procedures

This section describes the processes involved in collecting multiple IR images, VIS images and direct temperature measurements for a converging and diverging particle curtain. Also outlined are the procedures followed to assess the repeatability (i.e. absolute error and standard deviation) of these measurements. Preliminary repeatability results are presented in this section with their method descriptions for ease of reference. The selection of experiments was designed to assess the ability of IR thermography to capture characteristics of hot particle curtains, as well as to assess the minimum quantity of data that must be collected to have confidence in the resulting measurement. Descriptions of camera alignment and scaling techniques using the selected software are also presented.

The general experimental procedure followed to create a hot particle curtain began by filling the hopper with silica beads, then placing it in an oven to reach thermal equilibrium. Once data recording had been initiated (i.e. scale indicator and temperature data logger), the hopper was removed from the oven and immediately placed in the spreader box. Manual release of the hopper valve began the flow of particles (marked time ‘zero’). For more detail on this methodology, see Appendix 4. The corresponding risk assessment for this procedure is provided in Appendix 5.

### 3.2.1 Initial Thermal Conditions

Obtaining accurate experimental data depended heavily on maintaining consistent initial thermal conditions. Such conditions included commencing tests with hopper contents of uniform temperature, in addition to consistency of the particulate temperature at the time of valve release.

#### 3.2.1.1 Oven Conditions

Experiments required that the hopper and its contents were of a uniform temperature. A test to determine the waiting period to allow the hopper to reach equilibrium was performed. A full hopper (containing 4.2kg of silica beads) was placed in a LABEC general-purpose fan forced oven set at 120°C. Temperature was then regularly sampled at three locations (shown in Figure 3.9) within the hopper using a thermocouple. At the required setting the ‘stable’ temperature was estimated to be 124.8°C, shown in Figure 3.10. Accordingly, the hopper was left in the oven for at least 10 hours prior to experimentation.

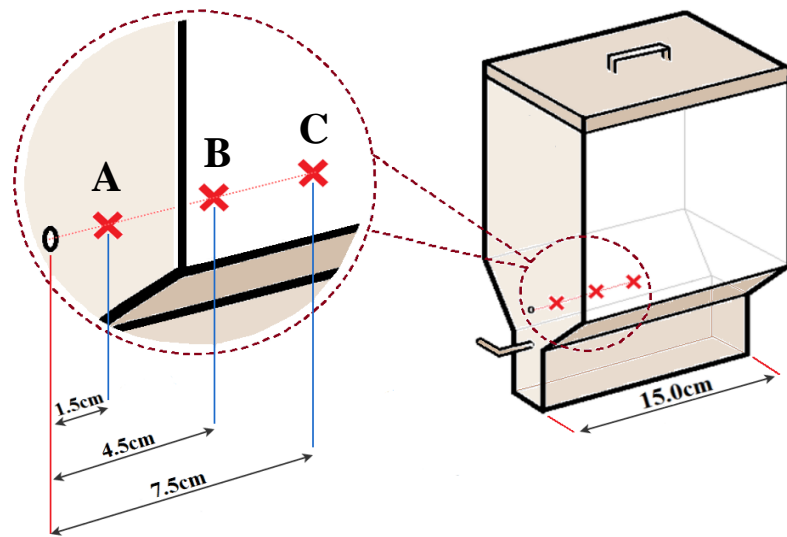


**Figure 3.9:** Sampling location and depth of measurement for points A, B and C measured using a thermocouple

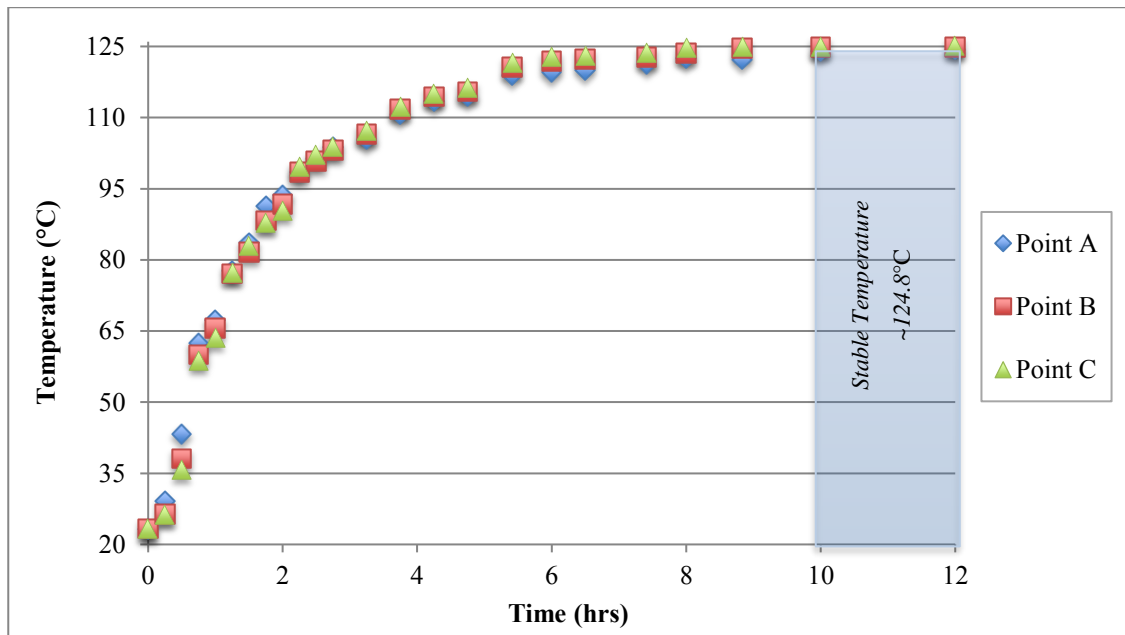


**Figure 3.10:** Plot of internal hopper temperature in 120°C oven at Points A, B and C over a 12-hour period

### 3.2.2 Mass Flow Rate

A series of five tests were completed to assess the standard deviation of mass flow rate. To mimic experimental conditions, the spreader box assembly was deconstructed prior to each test (required for alternation of slot sizes). A digital scale indicator residing below the catch bin, pictured earlier in Figure 3.2, determined mass flow rate. This scale was connected to a R40

viewer device, and linked to a laptop using a USB Rinlink cable. The RinstrumView400 software interface controlled the device to precisely measure the mass of the falling particles over time. Following data collection, a linear correlation was used to determine the average mass flow rate during each run. All tests produced  $R^2$  values greater than 0.9994, with the majority given a 1. Examples of this linear correlation are shown below in Figure 3.11 for the 20mm (0.166kg/s) and 60mm (0.160kg/s) slot width respectively.

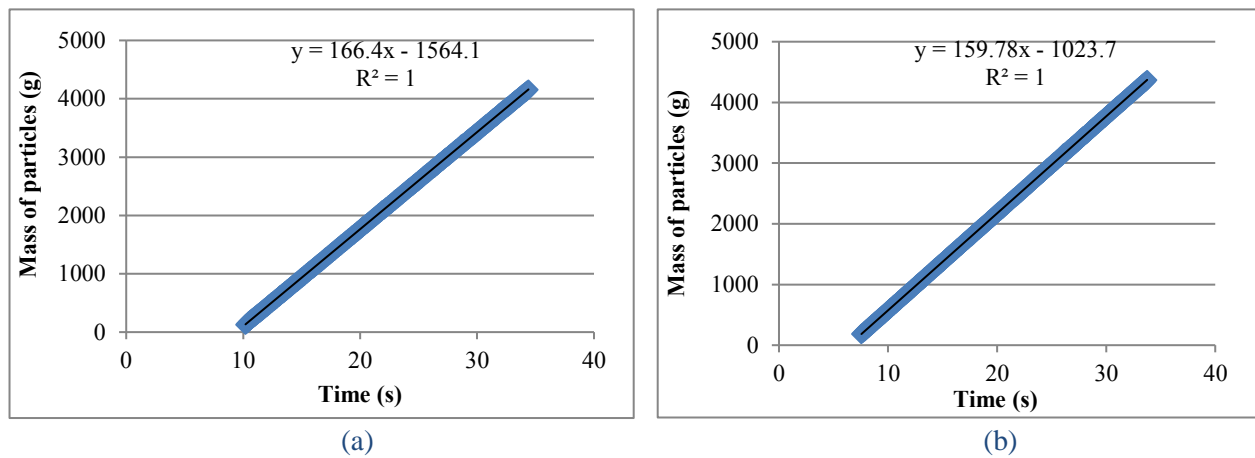


**Figure 3.11:** An example of a mass flow rate calculation for the 20mm (a) and 60mm (b) slot width

Results from the analysis of mass flow rate standard deviation are presented in Appendix 6. Mass flow rate at ambient conditions showed particularly high consistency, with a low standard deviation at the 95% confidence interval (0.000548 kg/s). This was due in part to the thorough cleaning regime introduced following the observation that insufficient cleaning around the hopper valve obstructed its range of movement. Tests were run at ambient conditions due to the 10-hour turnover between hot tests (outlined in Section 3.2.1.1). It was predicted that heating the hopper would impact the mass flowrate, but not the relative magnitude of the standard deviation. To confirm this, the mass flowrate was monitored during all experimental tests (thermocouple, IR and VIS).

### 3.2.3 Hopper and Curtain Temperature

Hopper temperature was recorded simultaneously with sampling cup temperatures to generate a plot similar to that of Figure 3.12. After placing the hopper in the spreader box, a temperature probe (with an accuracy of  $\pm 0.1^\circ\text{C}$ ) was inserted through a hole directly above the hopper valve. This permitted the internal hopper temperature, and its uniformity, to be monitored.

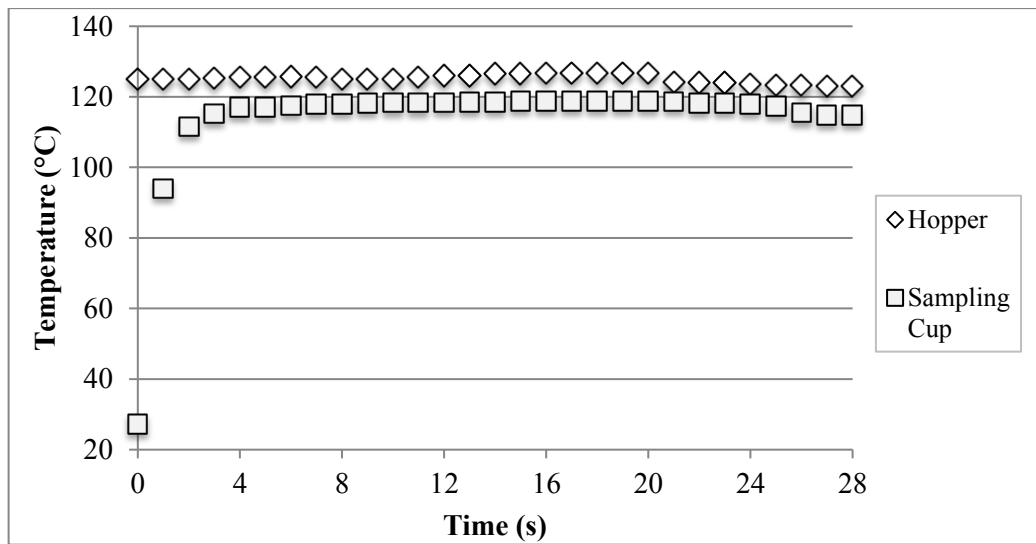


**Figure 3.12:** Example of hopper and sampling cup temperature recorded during direct sampling cup measurements

Extraction of singular curtain spot temperatures were a result of averages taken over the region of greatest stability (as described by Afshar [9]). Figure 3.13 presents the temperature profiles measured using the new sampling cups for five separate runs. All observed a consistent stabilisation period of between 10 and 20 seconds after valve release. The average temperature during this time frame therefore was recorded as the stabilised sampling cup temperature. Importantly, it was clear that the data did not skew upwards substantially, as was observed by Afshar [9] (shown previously in Figure 2.6). This can be attributed to the thorough methodology put in place to ensure the hopper contents were in thermal equilibrium.

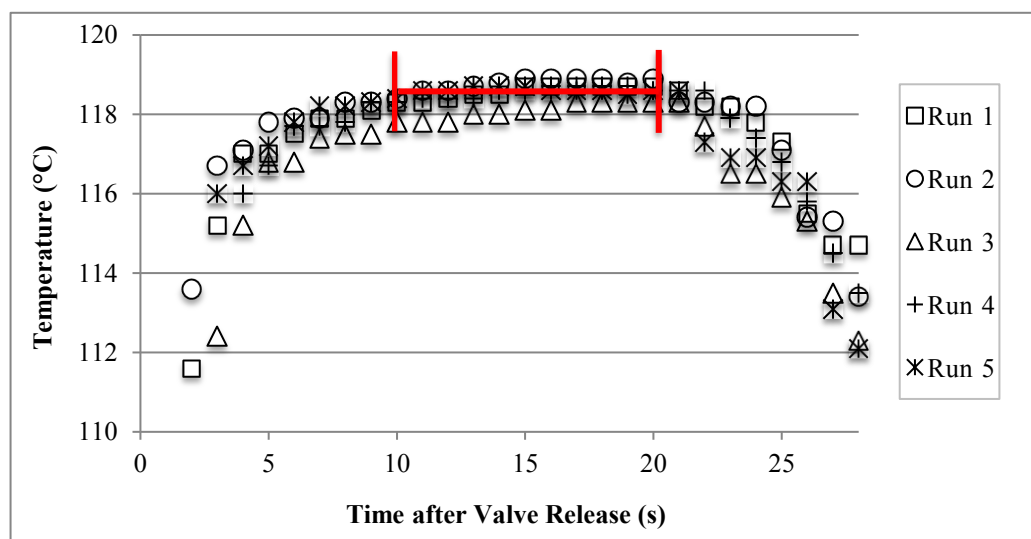


**Figure 3.13:** Plot of five repeat thermocouple data trends for 60mm slot width, taken at 8cm depth and 4cm height

Key parameters of the five data sets are listed in Table 4. For each run, the average temperature was determined using data between 10 and 20 seconds (the ‘stabilisation period’). The results of each test were used to compute the sample standard deviation. Treatment of the data as 50 individual data points produced the same 0.3°C standard deviation as using the five average temperatures presented in Table 4. The data suggests that the variability was primarily a result of marginal changes in the internal hopper temperature and/or mass flowrate. The internal hopper temperature and mass flowrate were subsequently recorded during all thermocouple tests for monitoring purposes.

**Table 4:** Direct thermocouple consistency assessment for 60mm slot width, width, taken at 8cm depth and 4cm height

Run No.	Stabilised Sampling Cup Temperature (°C)	Maximum Hopper Temperature (°C)	Mass flow rate (kg/s)
1	118.6	126.0	0.164
2	118.8	126.1	0.164
3	118.1	125.5	0.161
4	118.6	125.7	0.163
5	118.6	125.7	0.164
<i>Average</i>		125.8	0.163
<i>Std. Deviation</i>		0.2	0.0015

It was hypothesised that the temperature deviation presented in Table 4 would increase nearer the edge and the base of the curtain, where fluctuations in the curtain (i.e. ‘wobbling’) could affect the uniformity of the mass hold-up. Thermocouple temperatures recorded at all locations yielded an identical standard deviation of 0.3°C when analysing their variability within the stabilisation period. The exception however were temperatures recorded at zero depth; it was observed that as height increased, the standard deviation grew steadily from 0.3°C to 1.5°C at 60cm. Sampling points taken at zero depth were therefore assumed to have a linearly increasing standard deviation with curtain height, given in Equation (8). Additionally, to account for error in the positioning of the sampling cup, a margin of ±5mm error was included for all measurements of distance (depth/height), corresponding the length of the thermocouple bead tip.

$$\sigma(h) = 0.021h + 0.21 \quad (8)$$

### 3.2.4 Bulk Curtain Heat Transfer

The literature review revealed an absence of knowledge about the comparative bulk heat transfer exhibited by converging and diverging particle curtains. A simple experiment was therefore designed to compare each curtain behaviors' bulk heat transfer. The equipment setup substituted the catch bin for a similarly shaped esky 15L (of dimensions 25cm × 32cm × 23cm high). The standard experimental procedure was repeated, however the esky was filled with 10.0L of water and fitted with a thermocouple. The esky was placed precisely 60cm below the spreader box outlet, and it was subsequently assumed that the vast majority of falling silica beads were caught in the opening. The known specific heat capacity of water (4.186J/g°C) and silica (J/g°C) was then used to back-calculate the temperature change of silica during each curtain run. The bulk curtain temperature change was then inferred from Equation (9), and thus the comparative heat transfer, Q, could be estimated from Equation (10). Here the specific heat capacity of silica was assumed to be that of polycrystalline silicon dioxide: 0.745J/g°C at 300K [46].

$$m_{silica} \ C_{p,silica} \ \Delta T_{silica} = m_{H_2O} \ C_{p,H_2O} \ \Delta T_{H_2O} \quad (9)$$

where,

$$\Delta T_{silica} \propto Q \quad (10)$$

#### 3.2.4.1 IR & VIS Image Capture

Previous research by Afshar [9] into coupling IR with VIS imaging particle curtains involved the analyses of singular images. This thesis shall collect multiple IR and VIS images to provide realistic averages of curtain trends. A series of 30 images were processed for both IR/VIS imaging (taken at the onset of the stabilization period) to generate a smooth 'average' 2D temperature profile/curtain width. These averages were then compared with their constituent data sets to produce a height-dependent standard deviation profile. All images were taken 10 seconds after valve release to align with the onset of the stabalisation period, determined in Section 3.1.3.1. IR camera software allowed thousands of images to be captured in series at 1/30 fps. For all IR tests, 1200 frames were recorded, which covered the 30-second runtime of the particles' descent plus frames before and after valve release. These helped assess the changing environmental influences (i.e. heating of the backdrop) as a potential error source. Repeat VIS images were captured by in continuous shooting mode by holding down the shutter button, recorded at 1/60 fps.

To prevent angular deviation, IR and VIS images were not recorded simultaneously. The IR camera was placed on a tripod at a perpendicular distance of 2.79m from the spreader box, while

during VIS image capture the camera was placed at 1.30m (shown previously in Figure 3.3). These distances represented the minimum offset at which the full 60cm below the spreader box was observed in the FOV, without angling the camera downward. The tripod was adjusted so that the camera's direct line of sight was aligned with samples taken at a height of 4cm.

### 3.2.5 Image Calibration

Methods applied to calibrate imaging equipment, as well as to determine their associated error, are presented in this section. Also included are the steps taken to determine the thermal properties of the silica beads.

#### 3.2.5.1 Emissivity

Emissivity has been established as an important parameter to determine prior to operation of the IR camera. In-camera calibration [22, 34] was chosen as the method to achieve this. Typically the sample in question is first heated to a known temperature. The IR camera is focused on the sample, then the camera's emissivity value is adjusted until the correct spot temperature reading of the sample is displayed. Importantly this calibration cannot be performed at ambient conditions because when an object and ambient temperature are equal, the dependence of the detector signal on emissivity is eliminated (Equation (7)). In this thesis, a heat lamp was employed to heat a sample of silica beads from behind a barrier, which was fitted with a sampling cup containing the beads (shown in Figure 3.14). Two bulbs, 200W and 275W, were used in combination to generate 3 different surface temperatures. A cylindrical aluminium container, shown in Figure 3.15, was placed over the sample. This minimized heat loss to keep the particles at the sample surface closer to that of the bulk particle temperature. A hole in the end of the cylinder allowed the IR camera direct line-of-sight to the sample surface (Figure 3.15).

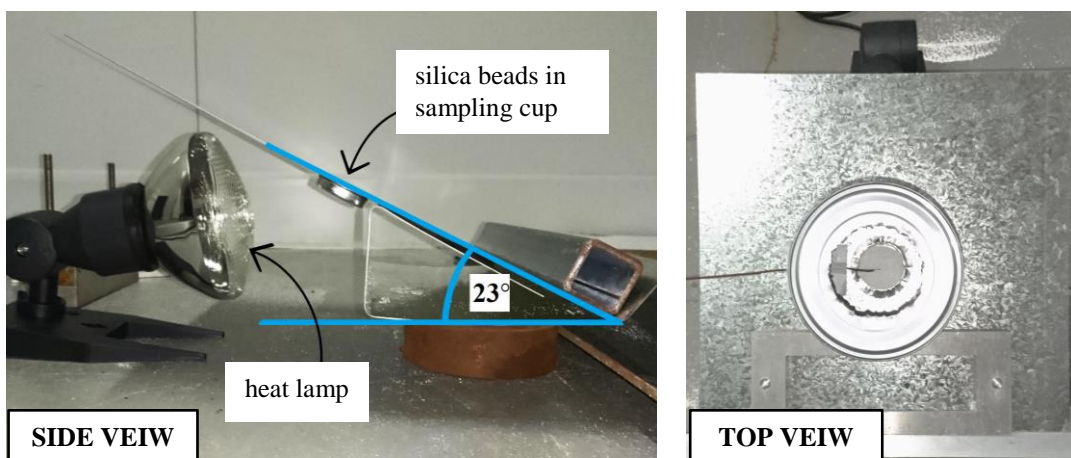


**Figure 3.14:** Setup of heat lamp positioned behind metal barrier to heat the silica bead sample

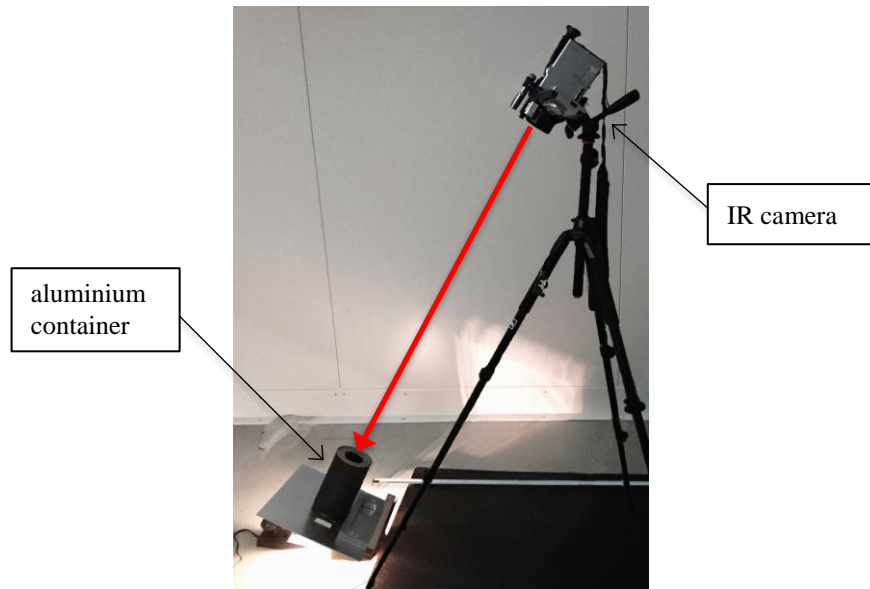


**Figure 3.15:** Set-up of IR camera relative to sample, line of sight directed through the aluminum container onto the sampling cup

To ensure a quality reading [34], the camera was positioned such that its line of sight resided within a  $40^\circ$  angle to the normal of the bead surface (assuming the surface was flat). To minimize the required height of the IR camera from the ground, the platform was designed to hold the silica beads at their calculated angle of repose,  $23^\circ$ . The center of the sampling cup was then made the spot target temperature of the IR camera. It was assumed that after sufficient time the beads reached thermal equilibrium, at which time the tip of a T-type bead thermocouple was used to record the surface temperature. Variability in the surface temperature was anticipated to arise and depended on the specific placement of the thermocouple tip, described in Figure 3.16. The temperature of the sample was taken to be the average of the temperature recorded at these two locations.

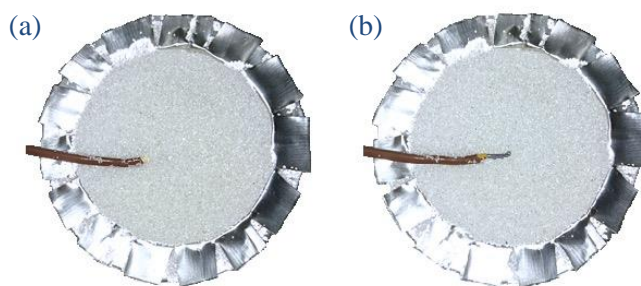


**Figure 3.16:** Optional thermocouple placements in silica bead sample: with tip submerged until just concealed (a), and with the tip resting against the surface (b).

Emissivity was adjusted in the IR camera between 1.00 and 0.80, and the IR recorded temperature was noted at 0.01 intervals. See Appendix 7 for a detailed procedure on the iterative adjustments made to calculate the emissivity of the silica beads. Figure 3.17 provides an example of the raw data collected from one of three emissivity tests performed.

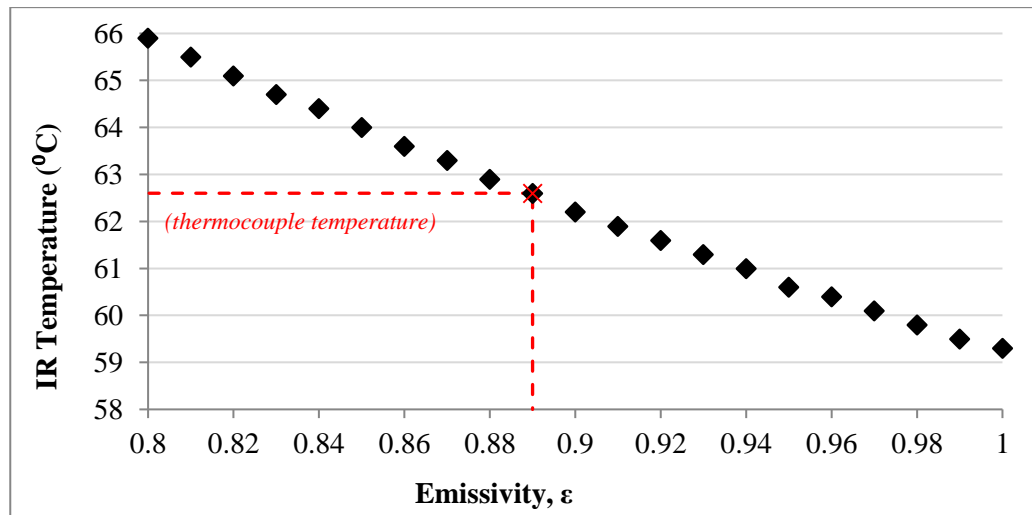


**Figure 3.17:** Run 3 from emissivity test. Direct temperature of the silica bead surface was recorded by thermocouple at 62.6°C.

A simple interpolation at the 62.6°C recorded surface temperature gave an emissivity ( $\epsilon$ ) of 0.89. Three separate tests at different surface temperatures (46.6 °C, 55.4°C and 62.6°C) yielded the same result (between 0.88 and 0.90, shown in graphs provided in Appendix 8). This value is supported by literature, which suggests the emissivity of silica varies between 0.80 and 0.95 over the 8-15 $\mu$ m wavelength range of the IR camera [22]. The IR thermography temperature is greatly influenced by emissivity, changing by ~6°C between the emissivity range of 0.80 to 1.00 at a 62.6°C thermocouple surface temperature. It is important to note that assuming  $\epsilon = 1.0$  would lead to a recorded IR temperature that is less than the direct temperature measurement of the particles. Previous work has made this assumption, [9], and could have contributed to the underestimation which was observed when the IR temperature was compared to the direct thermocouple temperature.

Although the data in Figure 3.17 appears perfectly linear, according to Equation (6) it is more appropriate to plot inverse of emissivity against the fourth power of temperature, as shown in Figure 3.18. A linear interpolation yielded high R<sup>2</sup> values (>0.9978) for all three tests, indicating an excellent match to theory.

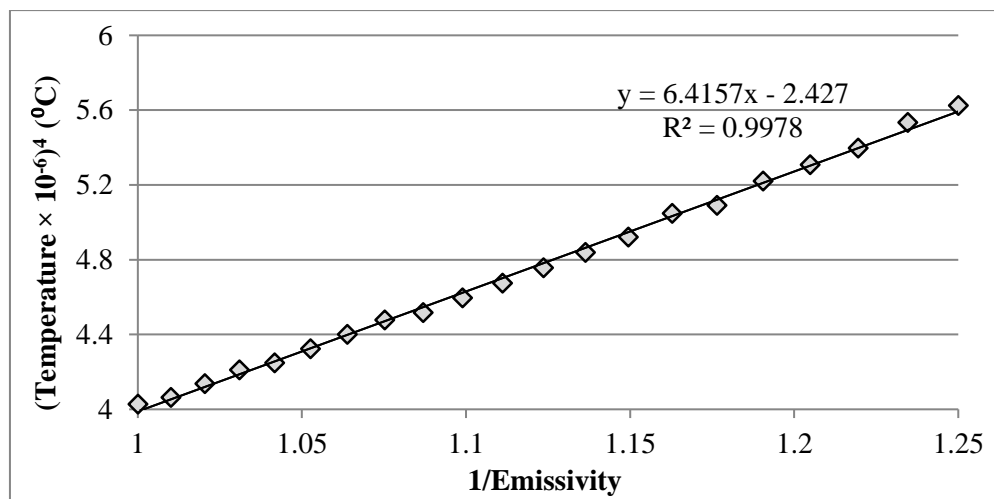


**Figure 3.18:** The linear correlation between the inverse of emissivity and the fourth power of temperature at 62.6°C surface temperature

To generate an approximate error margin in the recorded emissivity, the previously determined maximum and minimum temperature recorded by the bead tip thermocouple had their respective emissivity's found by interpolation of Figure 3.17. Table 5 compiles the absolute error of emissivity observed for all three measurements. It was evident that error in the recorded surface temperature increased with the sample temperature. Despite this, the magnitude of error in the emissivity measurement decreased with increasing surface temperature. Due to practical limitations on obtaining higher, controlled surface temperatures, the absolute error in the emissivity approximation was hereafter quantified as 0.04 (or  $\pm 0.02$ ). This corresponded to the smallest confidence interval obtained at the hottest surface temperature.

**Table 5:** Recorded sample surface temperature and corresponding absolute emissivity error

Run No.	Thermocouple Temperature		IR Camera Emissivity	
	T <sub>average</sub> (°C)	ΔT (°C)	ε	Δε
1	46.6	1.1	0.89	0.06
2	55.4	1.2	0.89	0.05
3	62.6	1.4	0.89	0.04

### 3.2.5.2 Light Intensity Calibration

It was essential to avoid the influence of external radiance on pixel intensity during VIS image capture. To ensure an even light distribution across the relevant area, a piece of white rectangular cardboard was placed at 0cm depth below the spreader box (Figure 3.19(a)). VIS images were then taken of the area and processed in MATLAB. Image normalization following Gaussian smoothing produced a 2D intensity profile, such as in Figure 3.19 (b). The standard deviation ( $\sigma$ ) of intensity was also generated for reference. Lighting equipment was subsequently arranged around the spreader box, and iterations of image capture and lighting equipment adjustments proceeded until pixel intensity was consistent and  $\sigma$  was negligible (Figure 3.19 (c)). Alternate calibration methods were investigated to accelerate this time-consuming process. The subtraction of ‘noise’ (inconsistent regions of intensity) from the captured VIS image was trialed, but proved ineffective due to its assumption of equivalent material reflectivity between the cardboard and the silica beads.

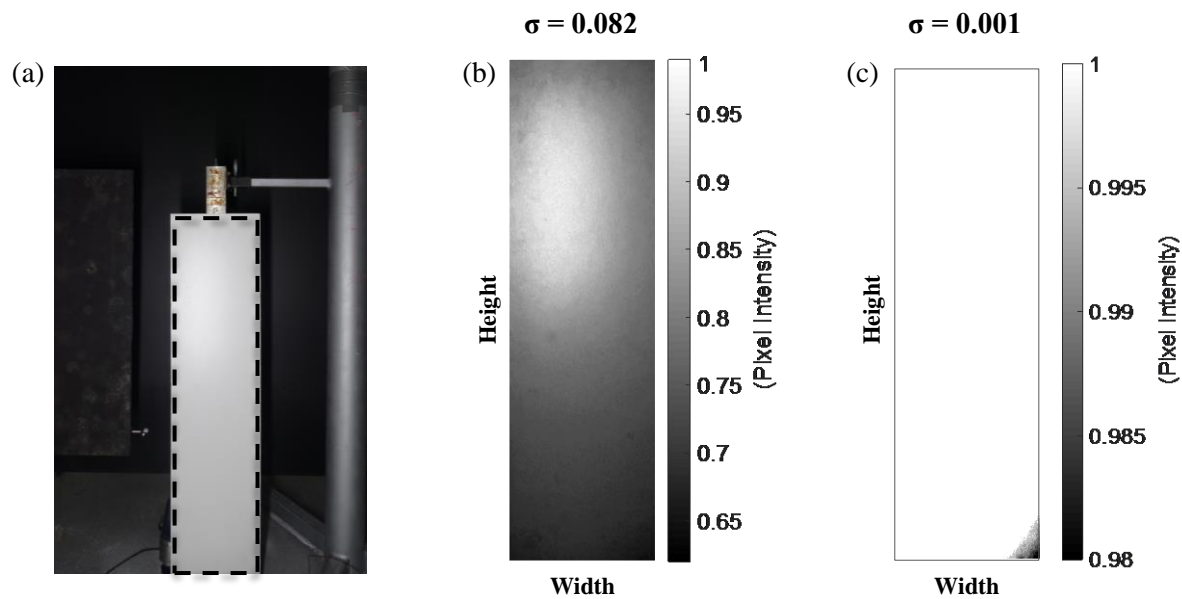


**Figure 3.19:** Images describing the iteration procedure employed to generate a consistent pixel intensity distribution. Initially image (a) is captured and processed in MATLAB to give profile (b) and repeated until  $\sigma$  approaches zero, profile (c).

### 3.3 Image Analysis

This section outlines the methodologies and types of statistical analyses applied to analyze IR thermography's ability to determine particle curtain edges and temperature. Once again, preliminary consistency results are presented together with their method descriptions, for ease of reference. The selected analysis routes were also designed to explore how the magnitude of data collected influence the quality of the result.

#### 3.3.1 MATLAB Code Development

MATLAB (matrix laboratory) was the primary software utilized for image processing and analysis. The following section outlines the general methodologies followed in the software both to pre-process and analyse direct thermocouple measurements, VIS, and IR images.

##### 3.3.1.1 Curve-fitting Thermocouple Data

MATLAB's curve-fitting tool (available exclusively with the *curve-fitting toolbox*) was used to fit various standard and custom models to the data in pursuit of the best fit. Figure 3.20 shows an example of the interface, and the generation of equation coefficients and  $R^2$  values. For assessment of the curtain temperature with height, additional weighting matrices were incorporated to the regression analysis. These weights ( $w$ ) were equal to the inverse of variance for each data point, (i.e. the inverse of standard deviation squared,  $\sigma^2$ , shown in Equation (11)). Weighted curve-fitting factors in the various levels of confidence held in discrete data points, such as the direct thermocouple's measurement versus height (described in Section 3.2.3).

$$w_i = 1/\sigma_i^2 \quad (11)$$

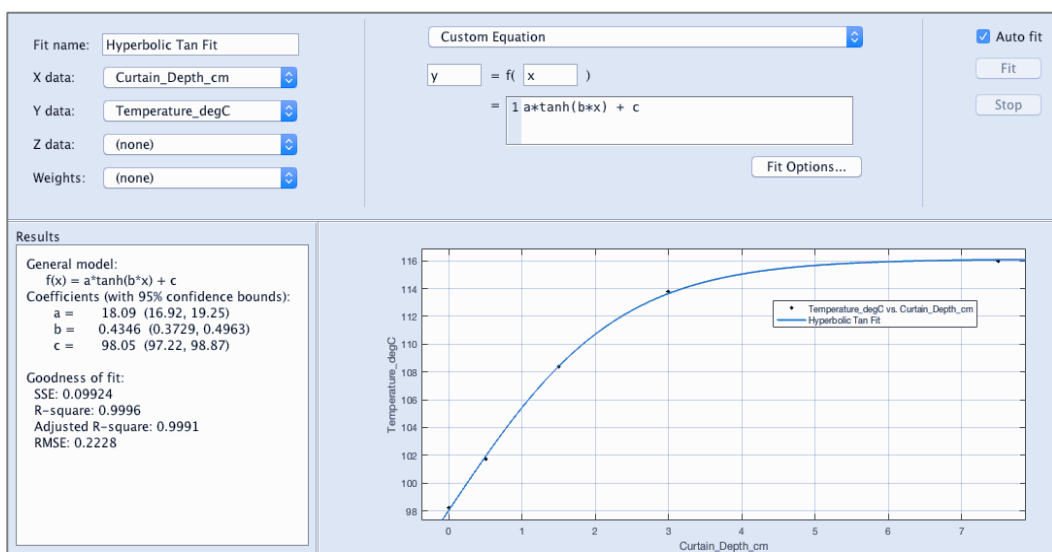


**Figure 3.20:** MATLAB's curve-fitting interface, used to show the goodness of fit for the curtain temperature with depth.

As taking multiple direct samples from two independent slot width curtains was a lengthy process, methods of interpolating temperature with curtain depth were investigated. The hyperbolic tan function, while a good fit, introduced three coefficients. Plotting new parameter,  $\phi$ , versus depth, subsequently normalized the temperature scale. It was then assumed that the remaining two coefficients in Equation 12,  $a$  and  $b$ , were solely dependent on curtain height.

$$\phi(h) = \frac{T - T_{min}}{T_{min} - T_{max}} = a \tanh(bx) \quad (12)$$

### **3.3.1.2 Image Scaling & Alignment**

Particle curtain VIS and IR image scaling methods have previously involved capturing objects of known length in an image and applying ImageJ software to calculate a scale factor (in pixels/cm) [9]. Whilst this method is efficient for the analysis of single images, this thesis shall involve the pre-processing of numerous IR and VIS images. Between runs, the camera positioning and angle are unlikely to remain perfectly constant (i.e. affected by battery removal). To best mitigate these influences, an efficient scaling process was developed with MATLAB's image processing toolbox. A detailed description of this code and each line's function are included in Appendix 9. To start, the user is prompted to select the outline of the spreader box face (Step 2 in Figure 3.21). Conversion of pixels to length follows from knowledge of the spreader box dimensions, yielding a scaling factor. Once the user has confirmed the selection of the spreader box midpoint and exit (Step 3), the 'area of interest' (AOI) is selected. The AOI represents the area 60cm below the curtain and 16cm in width, scaled in both directions. This process can also correct for angular deviations. If images are taken in series, the process outlined in Figure 3.21 is undertaken for the first image, whose relative AOI location is applied to all subsequent images. This fast and efficient pre-processing can be applied to both VIS and IR images. Comparisons with traditional ImageJ scaling validated the accuracy and consistency of this method.

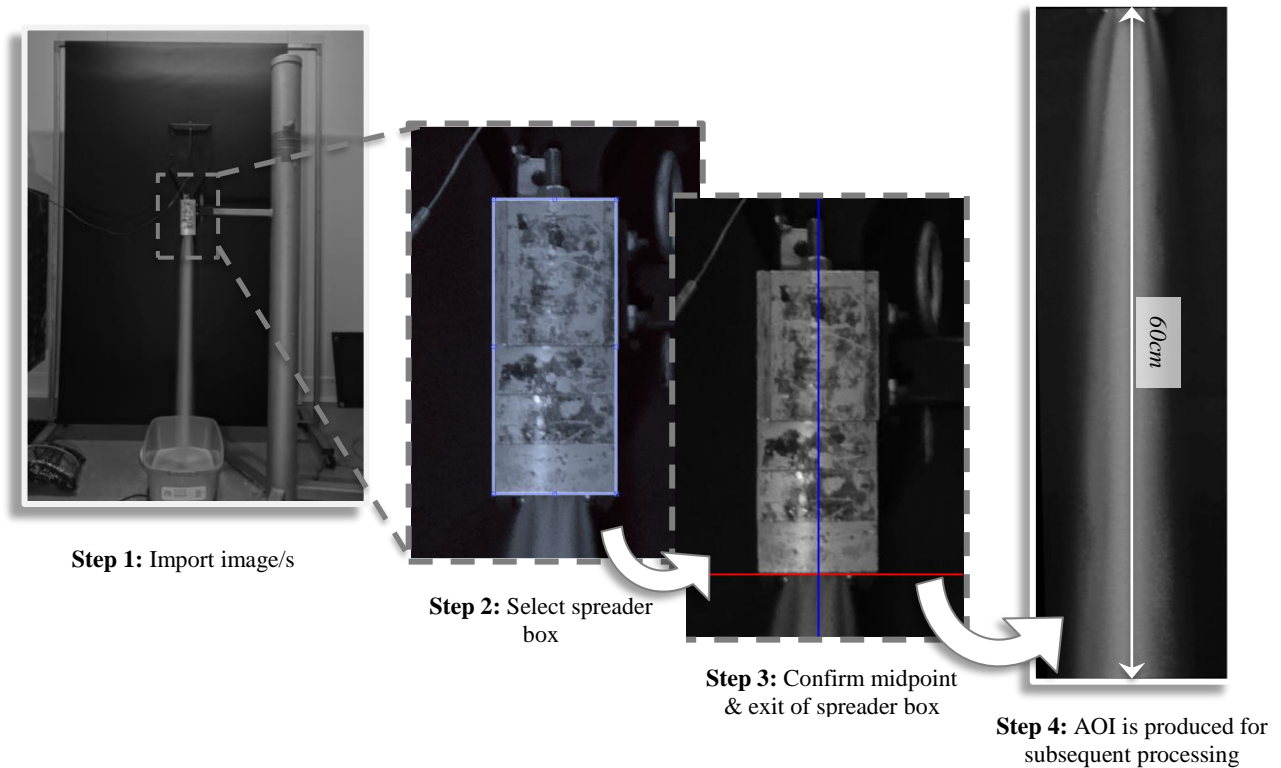


**Figure 3.21:** Pictorial description of the steps taken to scale images in MATLAB. Shown for VIS images.

### 3.3.1.3 IR & VIS Edge Detection

A variety of edge detection techniques applied to IR and VIS images are outlined in this section.

#### 3.3.1.3.1 Image Thresholding

The first step in image thresholding is determining the threshold value. As outlined in the literature review, this can be achieved using Otsu's algorithm. Specifically, a two-level threshold was chosen to account for the observation of hazy areas of intermediate intensity in the VIS images outlining the curtain (Figure 3.22(a)). This method best represented what was observed by eye, and reduced ambiguity in the distinction of the curtain edge. The threshold function was applied after Gaussian filtering ( $\text{Sigma}=1$  and  $\text{Kernel size}=\text{Sigma}\times 6$ ) using MATLAB's image processing toolbox. This separated pixels into three regions of intensity (white, gray, and black) shown in Figure 3.22(b). The grey area, or “fuzz”, represents an intermediate level of solids volume fraction.

To assess whether the 2D profile of the VIS image differed if run at ambient hopper temperatures (time-saving), a T-test was performed at the 95% confidence interval on both hot and cold

curtains to observe if the ratio of area assigned to high (*white*) and intermediate (*grey*) solids volume fraction were equivalent. As outlined in Appendix 10, a statistically significant difference was found to exist between the five hot and cold images collected from separate experimental tests. Assuming that intensity is proportional to volume fraction, this result implied that the volume fraction distribution is dependent on curtain temperature. Thus, the thermal conditions for IR & VIS images must be kept consistent. These images are also presented in Appendix 10 with their corresponding thresholded images.

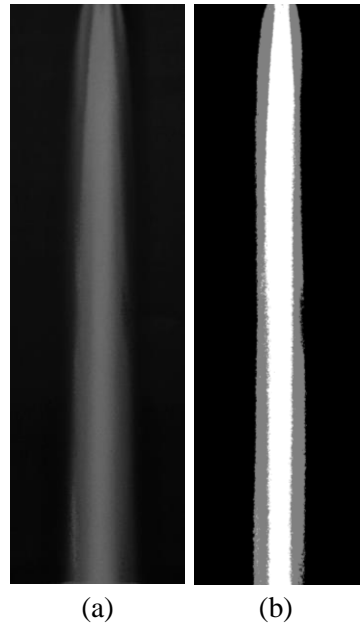


*Figure 3.22: Raw VIS image (a) and Gaussian filtered image with two-level threshold (b)*

To approximate curtain edges using thresholding, each row of image intensity is differentiated with respect to the horizontal direction:  $\left( \frac{\partial I}{\partial x} \right|_y \right)$ . Maxima are then identified, which were taken to be the curtain edges. An example of the inner and outer curtain widths produced using this method are shown in Figure 3.23. Due to the inherent image noise produced with high-resolution VIS images, edges determined by VIS thresholding were smoothed in the vertical direction using a 1D Gaussian filter. See Appendix 9 for code details.

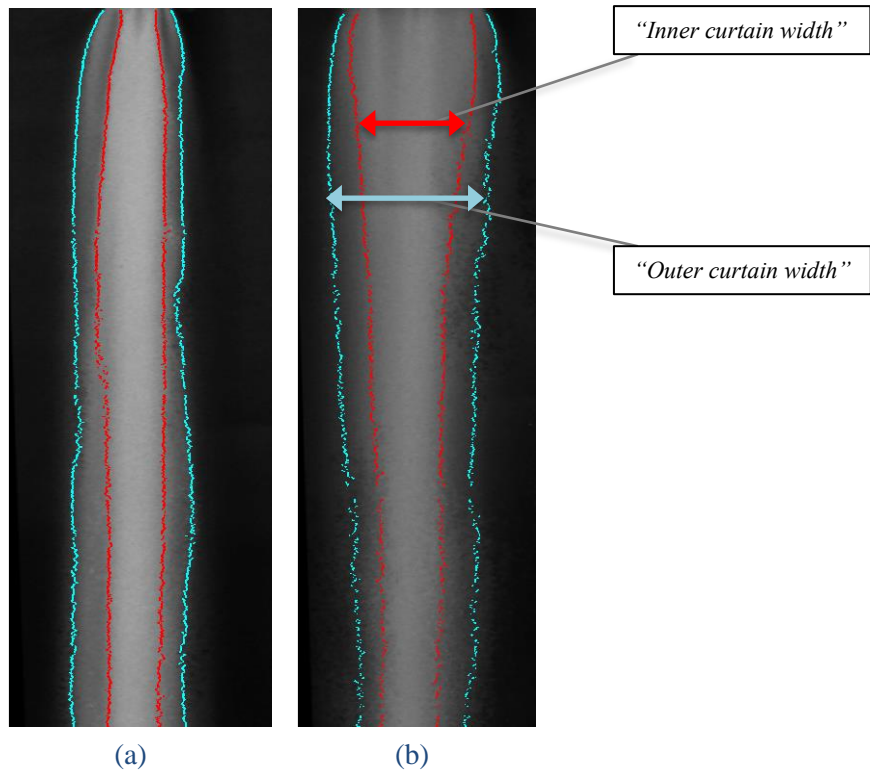


**Figure 3.23:** Edge detection result for 20mm (a) and 60mm slot width (b), overlaid on original grayscale, Gaussian smoothed images. Colours correspond to inner (•) and outer (•) edges.

### 3.3.1.3.2 VIS Edge Repeatability

Quantifying the repeatability of the curtain edge predicted by VIS image thresholding is crucial for later comparison with IR images. The following comparative plot was constructed to convey the degree of consistency of this technique (presented in Appendix 11):

- Inner and outer curtain width versus height for four individual frames, overlaid with their average profiles (of 30 frames)

Results concluded that the curtains showed a high degree of consistency in width leaving the spreader box outlet. Beyond a height of 10cm however, the widths began to undulate erratically, steadily worsening as height increased. The standard deviation applied in subsequent image comparison was consequently a dynamic function of height. Undoubtedly this was due in part to the increased curtain ‘wobbling’ as particles descended. Fluctuations could alternatively have been attributed to inconsistencies in the chosen thresholding prediction method. Particles travelled too far in the time-lapse interval to observe the gradual development of crests/falls in the profile to remove this as a potential error source. Nevertheless, the resultant average widths produced from the integration of 30 frames were reasonably smooth, as predicted.

### 3.3.1.3.3 Temperature Gradient (IR) Curve-fitting

Curtain edges were also approximated by differentiation, where it is assumed that the steepest gradient of temperature change corresponds to the curtain edge. The raw IR temperature versus curtain width in the  $x$  direction initially resembles Figure 3.24(a). Naturally, the curve sees a single peak in the center, corresponding to the maximum temperature in the curtain. Splitting the data into left and right side of the curtain, the curves of Figure 3.24(a) were differentiated at discrete heights,  $\left(\frac{\partial T}{\partial x}\Big|_y\right)$ . Second order polynomials were then fit to the derivative using MATLABs *polyfit* function. This yielded maxima akin to those shown in Figure 3.24(b). The ability of this method to distinguish between inner and outer curtain edges was investigated by inclusion of both polynomial roots (two for each second order polynomial), to observe if the second aligned with what has been defined as the outer edge.

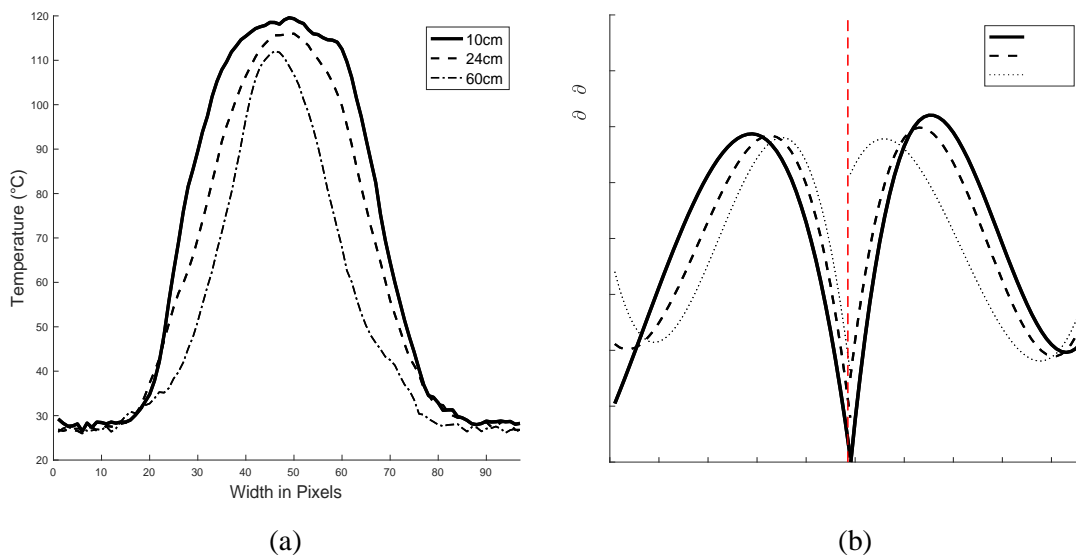


**Figure 3.24:** (a) Temperature versus width at three different heights of the middle plane, with (b) their corresponding curve-fitted temperature gradients found using a second order polynomial fit. Note (---) indicates the separation of left and right polynomials.

### 3.3.2 IR and Direct Thermocouple Temperature Alignment

From direct temperature measurements outlined in 3.1.3.2, a t-test analysis was carried out to assess the quality of match between IR and thermocouple measurements. This analysis was repeated with temperature data collected with curtain depth. The aim was to identify where the thermocouple and IR temperature observed the best quality of match. The principal conclusion to be drawn from this assessment was at what depth the IR camera actually measured, due to its potential to integrate temperature with depth. It is important to acknowledge that the chosen definition of ‘centerline temperature profile’ presented in this thesis differs from that presented

by Afshar [9]. Rather than a 3-pixel average, the chosen IR temperature is presented as the average of pixels spanning the width of the sampling cup inlet diameter (~24mm). This has significant implications on the resulting temperature profile, shown in Figure 3.25, however it was assumed this would provide a more accurate measure of temperature as seen by the sampling cup.

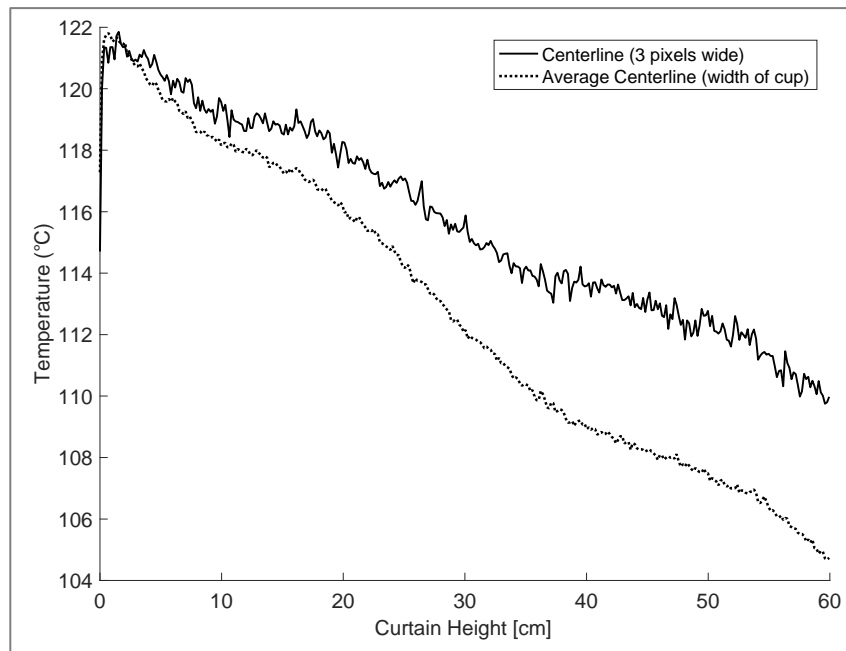


**Figure 3.25:** Comparison of centerline temperatures taken as a 3-pixel average (approach taken by Afshar [9]) versus profile averaged over the sampling cup width.

### 3.3.2.1 IR Centerline Temperature Repeatability

Two key plots were constructed to convey the degree of consistency between centerline temperature profiles (presented in Appendix 12):

- Centerline temperature at 5-second intervals for a single test to distinguish time-dependencies
- Centerline profiles for three distinct experimental tests to assess consistency between tests

As predicted, results showed that the centerline temperature profile remained reasonably consistent between 10 and 20 seconds following valve release. At the 25-second mark the temperature dropped significantly, which may be attributed to the release of particles into the curtain that have been cooling prior to release. Two of the three average centerline temperatures for distinct experimental tests (each the product of 30 sequential frames) exhibited an excellent degree of correlation. A closer inspection of the test yielding a notable offset revealed that

despite the consistency of flow rate (0.163 kg/s), the maximum hopper temperature was 0.8°C less than for the two alternate tests. As previously shown, this falls outside the standard deviation for maximum hopper temperature (0.2°C). This was sufficient evidence to exclude the dataset as an outlier.

### ***3.3.3 Summary***

Highly positive preliminary results confirmed flow rate, direct thermocouple measurements, VIS images and IR images are highly repeatable when following the outlined methodology. Discrete and dynamic variability of each technique has been successfully quantified for subsequent analysis of data. Furthermore, improved confidence is held in the ability of established indicators (i.e. internal hopper thermocouple) to exclude datasets falling outside the established variability.

## 4.0 Results & Discussion

Following confirmation of obtained system measurements and image consistency, the ability of IR imaging to capture the characteristics of a hot particle curtain was examined. This chapter emphasizes how physical differences, observed between curtains generated with a 20mm and 60mm slot width, influence the thermographical measurement. Analysis of temperature variation with depth is presented first. This section intends to highlight the comparative heat transfer mechanisms observed for each slot width condition, as well as elude to the potential limitations of applying IR imaging on such systems. Next, a brief interpretation of pixel intensity profiles will propose the height-dependent volume fraction effects of each slot width. This is followed by comparison of direct temperature and IR centerline temperature. Knowledge of previously explored characteristics of each slot width was applied to justify temperature alignment/misalignment. Lastly, the strengths and limitations of various edge detection methods (using both IR and VIS imagery) are presented, with particular focus on the relative ease of obtaining each approximation.

### 4.1 Temperature Variation with Curtain Depth

Temperatures recorded at five discrete depths within the 20mm and 60mm slot width curtain are shown in Figure 4.1 and Figure 4.2 respectively. MATLAB's curve-fitting tool found the hyperbolic tan function produced the best fit to the raw temperature data. A considerable difference was observed in the curtain temperature nearest a depth of 0cm. The favourable heat transfer experienced here likely resulted from increased ambient air contact. At greater depths, particles become 'shielded' in an environment of similarly hot particles. For both slot widths, the temperature converged to the maximum at a shallower depth nearer the spreader box (i.e. zero depth). Observed thermocouple data is very typical; the heat transfer of surrounding particles influences the heat transfer experienced by a single particle. This is via all forms of heat transfer, including convective (by heating of the surrounding air), conductive (direct contact), and radiative (EM radiation). As the outer-edge particles cool, this encourages a greater cooling of adjacent particles, moving inwards with a domino effect. Logically the 60mm slot width produces a greater temperature difference between the zero and 8cm depth than for the 20mm curtain. This is because the wider 60mm slot width reduces the proximity of particles to one another (i.e. volume fraction), thus reducing the magnitude of conductive and convective heat transfer.

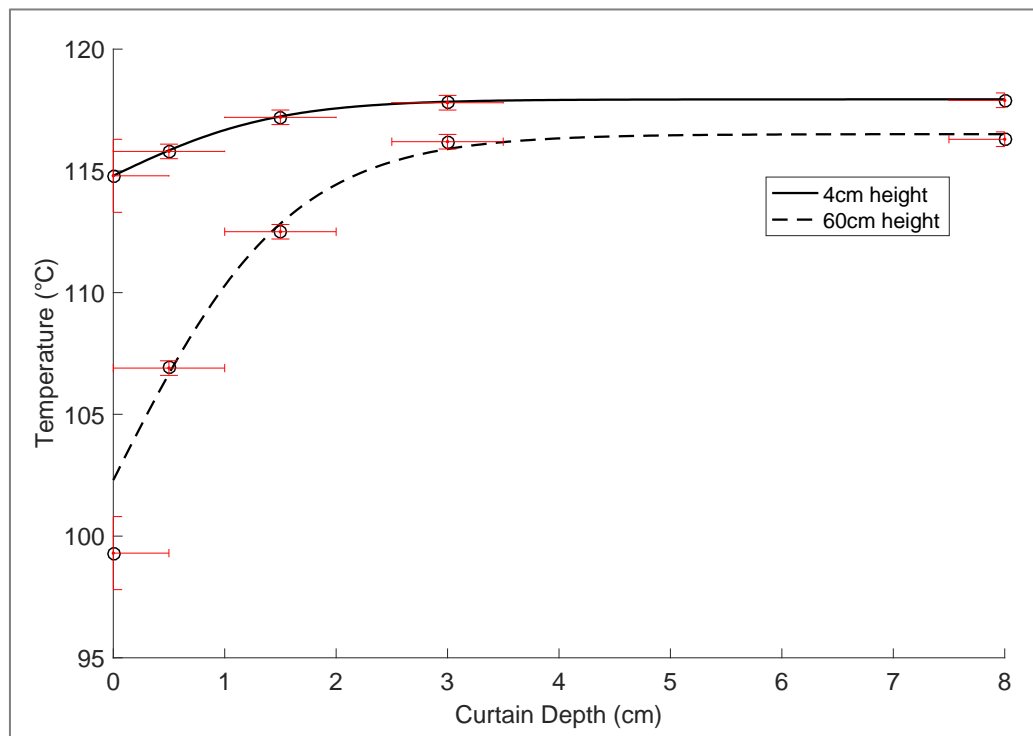


**Figure 4.1:** Thermocouple temperature profiles for 20mm slot width as a function of curtain depth

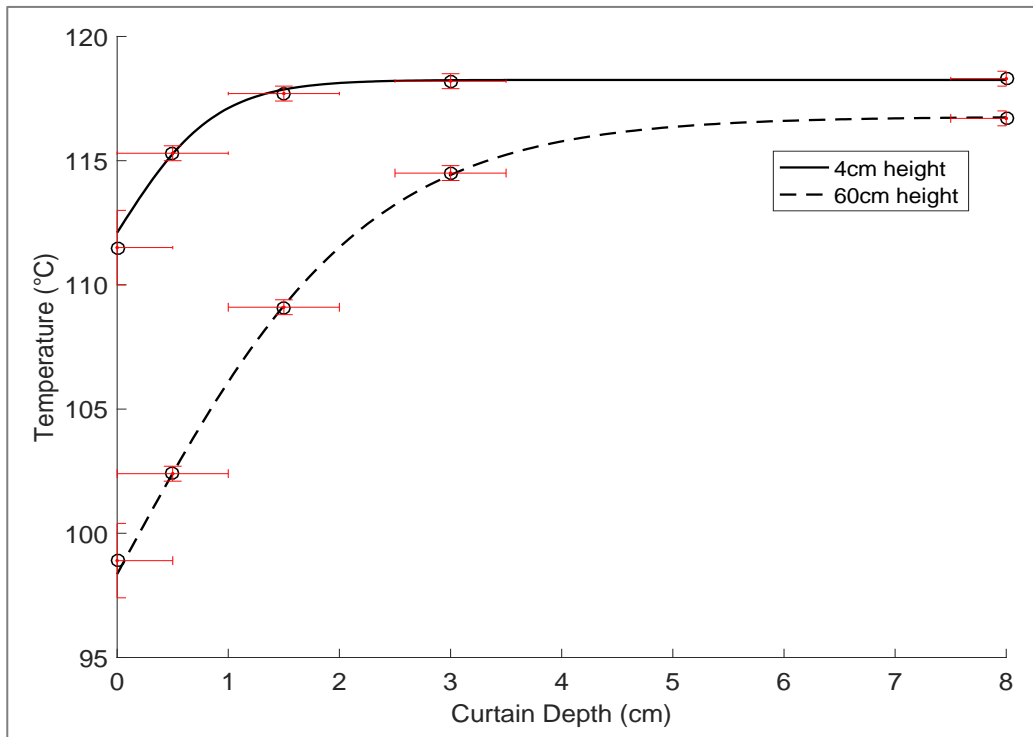


**Figure 4.2:** Thermocouple temperature profiles for 60mm slot width as a function of curtain depth

The curves presented were subsequently normalized for clearer evaluation of the temperature profile curvature (Figure 4.3 and Figure 4.4 for the 20mm and 60mm slot width respectively). This revealed an interesting property of the 20mm slot width curtain: the normalised temperature profile was virtually consistent with curtain height. In contrast, the temperature gradient of the 60mm slot width became smaller and more uniform as height increased. These images imply what has already been suggested: that each slot width condition, that is divergent (20mm), and convergent (60mm) particle curtains, undergo distinctly different modes of heat transfer during their descent. Additional curve-fitting techniques produced interpolated models of the 60mm normalized depth profiles. This was achieved by fitting the data to the model  $a \tanh(bx)$ , outlined in Section 3.3.1.1, where the ‘ $a$ ’ parameter remained constant and the ‘ $b$ ’ parameter was assumed to change linearly with height. Following the success of this modeling, it was noted that - provided the maximum and minimum temperatures ( $T_{min}$  &  $T_{max}$ ) were determined at these intermediate heights - models could be ‘de-normalised’ to give actual temperature estimations.

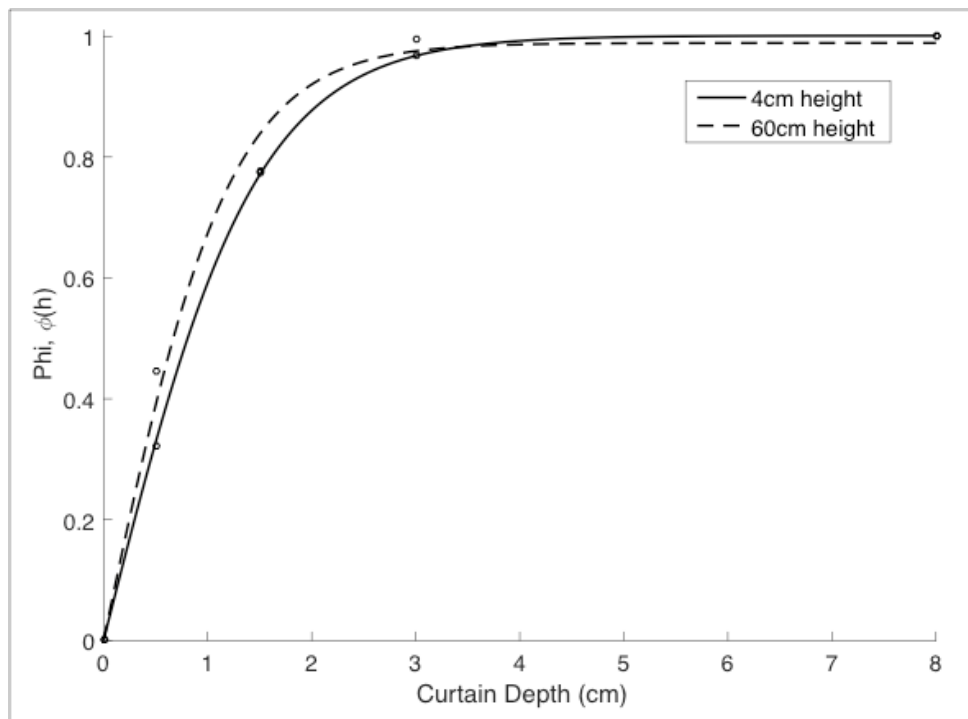


**Figure 4.3:** Normalised temperature profile where  $\phi(h) = (T - T_{min}) / (T_{max} - T_{min})$  for 20mm slot width curtain

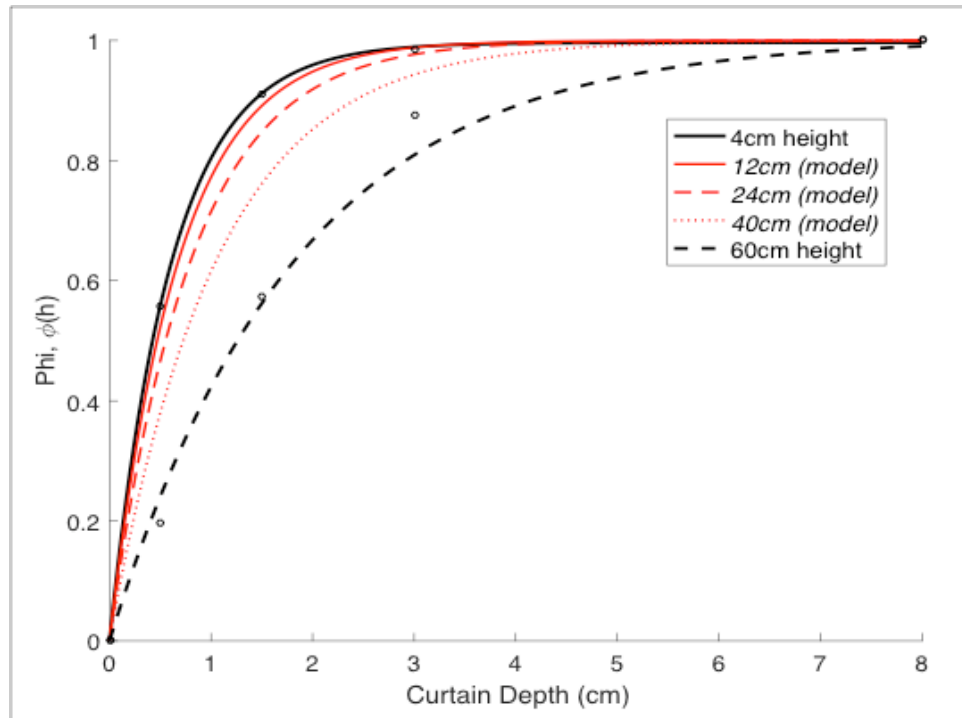


**Figure 4.4:** Normalised temperature profile where  $\phi(h) = (T - T_{min}) / (T_{min} - T_{max})$  for 60mm slot width curtain, with interpolated profiles for additional key heights

These results illuminate the additional challenges imposed on IR thermography. The temperature recorded by the IR camera within each pixel represents an average of the EM radiation received in that area (Figure 4.5). Results have confirmed there exists a considerable temperature difference between particles on the curtain edge and those at greater depths. A frontal view of the spreader box would result in cooler particles residing in the forefront of the curtain bulk, depicted in Figure 4.5. At curtain regions where the volume fraction is high, the pixel FOV will become saturated with particles at a shallower depth. Let it be assumed that the final temperature output for a given pixel is the area-weighted average temperature over the pixel. If the temperature gradients with curtain depth were also identical between curtain widths, a high solids volume fraction would output a lower curtain temperature reading. This also assumes that the reading is instantaneous (i.e. shutter speed is infinitely small). In reality, particles will travel on average through  $\sim 6$  pixels in the time it takes to record a single IR image. The phenomenon pictured in Figure 4.5 also explains the previously observed downfalls of IR imaging as applied to hot particle curtains. That is, IR thermography has ‘failed’ at low solids volume fractions, due to its integration of temperature from the background.

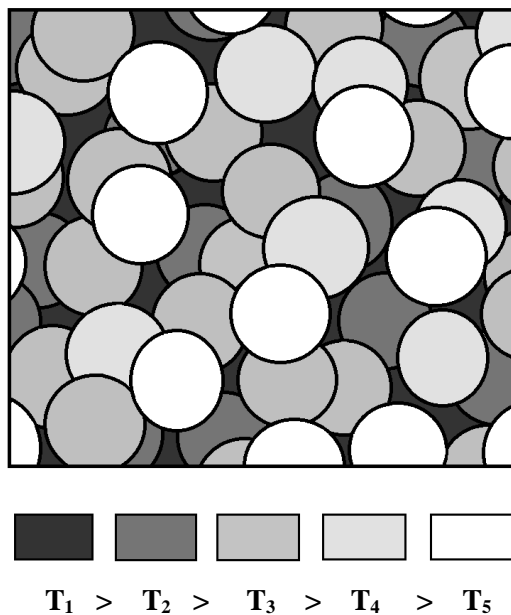


**Figure 4.5:** Pictorial description of a single IR pixel and the relative temperatures of perceived particles (drawn roughly to scale).

## 4.2 VIS Image Intensity vs. Height

Pixel intensity as a function of height for both slot width conditions is presented in Figure 4.6. It is very clear that identical gradients exist for both conditions. This insinuates that the separation effect of the particles during their descent, as they reach terminal velocity, is identical. The normalized intensity is undeniably greater for the 20mm slot width curtain. However, it is their specific offset that is of particular interest. Previously, particle curtain investigations have adopted theory which suggests that the VIS image pixel intensity is directly proportional to solids volume fraction, especially at low solids volume fractions [41]. In this thesis, the magnitude of the 60mm slot width pixel intensity is roughly 96% of the 20mm. For intensity to be proportional to solids volume fraction, this percentage should be significantly lower ~33%. Therefore, this result validates that this technique does not hold true for high mass flow rate conditions. Nevertheless, it can be hypothesized that an IR camera observing the 60mm slot width at the same height is more likely to integrate temperature to a greater depth than the 20mm slot width. Likewise, it is theorized that the thermographic temperature profile will overestimate the 60mm slot width centerline temperature reading further into curtain depth where hotter particles reside.

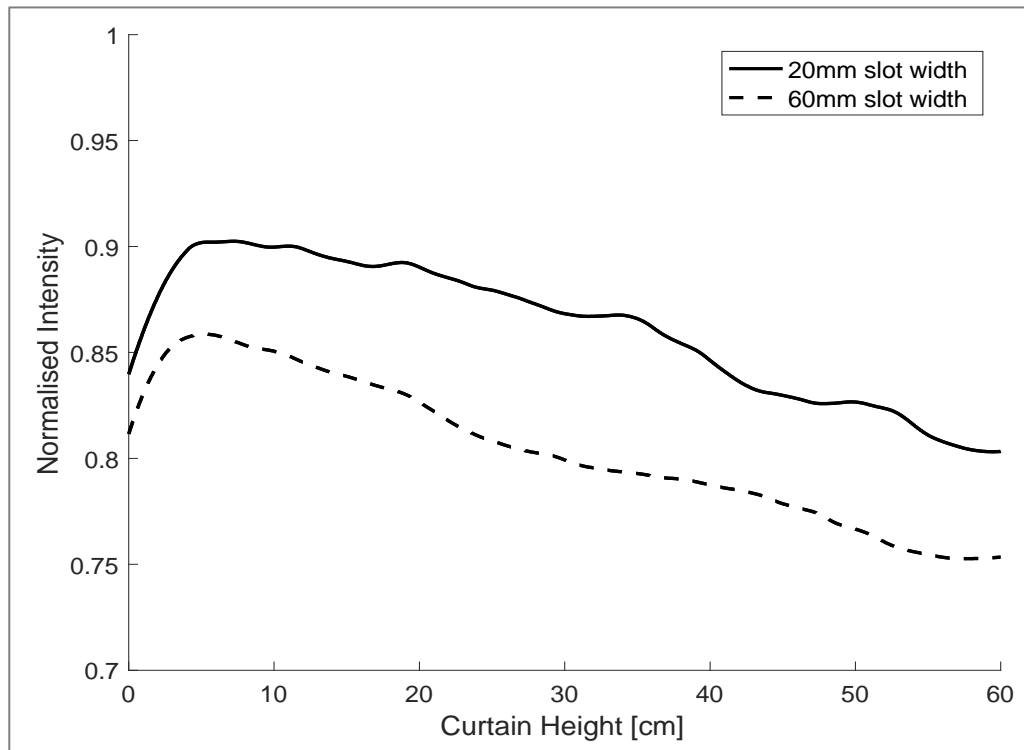


**Figure 4.6:** Normalised VIS image intensity centerline profile for 20mm and 60mm slot widths

### 4.3 Comparison of IR and Thermocouple Temperature

This section summarises the resulting agreement of IR thermography and direct thermocouple measurements in their prediction of curtain temperature. Firstly, Figure 4.7 presents the 30-frame average 2D temperature field profiles for each slot width condition. These images make very clear the divergent and convergent contour of the 20mm and 60mm slot widths respectively. Of particular interest were inconsistencies in curtain symmetry, for example, the asymmetric outlet temperature (labelled point [1]) at the 20mm slot width exit. Inconsistencies in the wire mesh pattern of the spreader base exit were determined to be the cause of variation, encouraging particles to favour the left side.

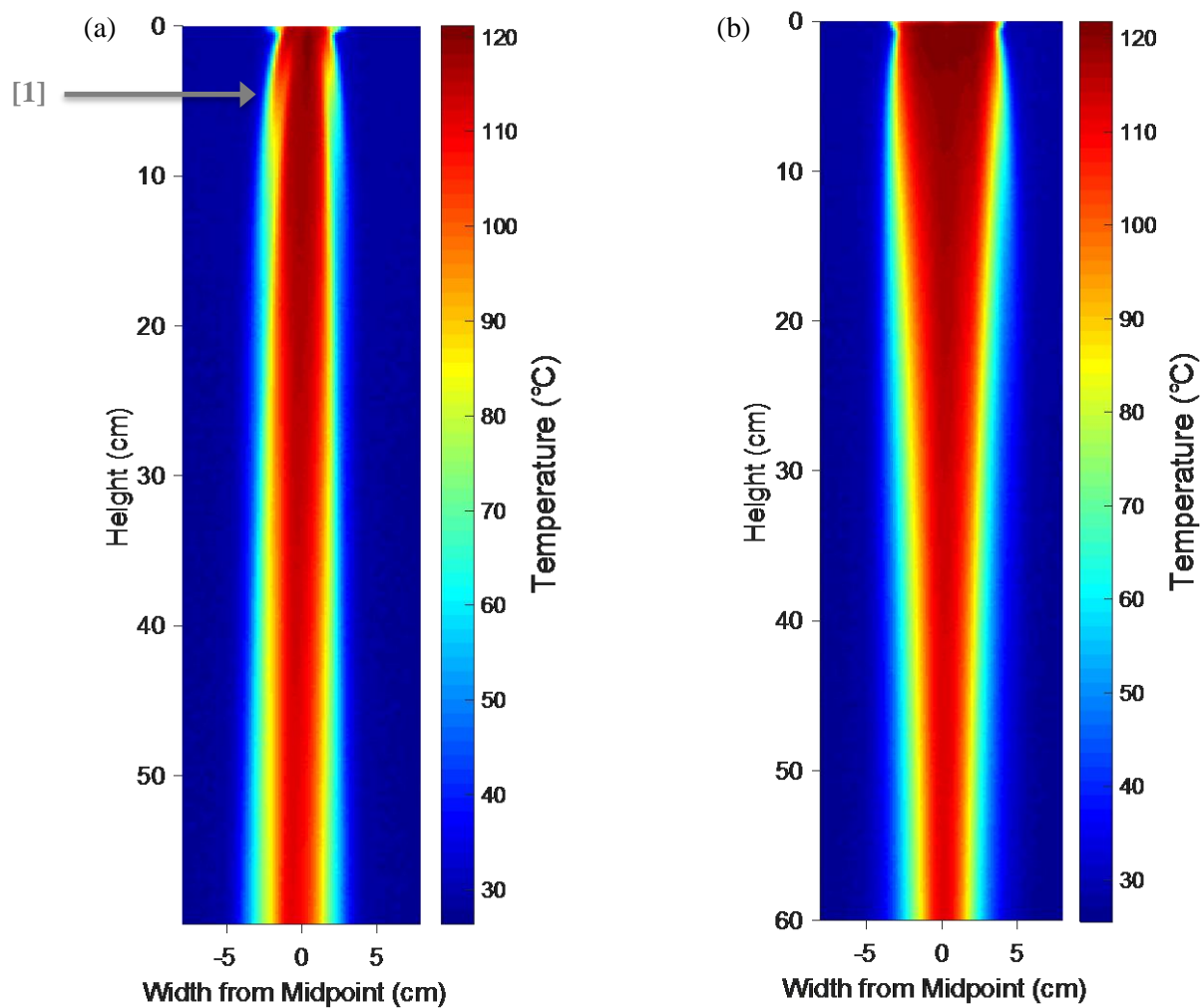


*Figure 4.7: IR average temperature field data for the 20mm(a) and 60mm (b) slot width curtain*

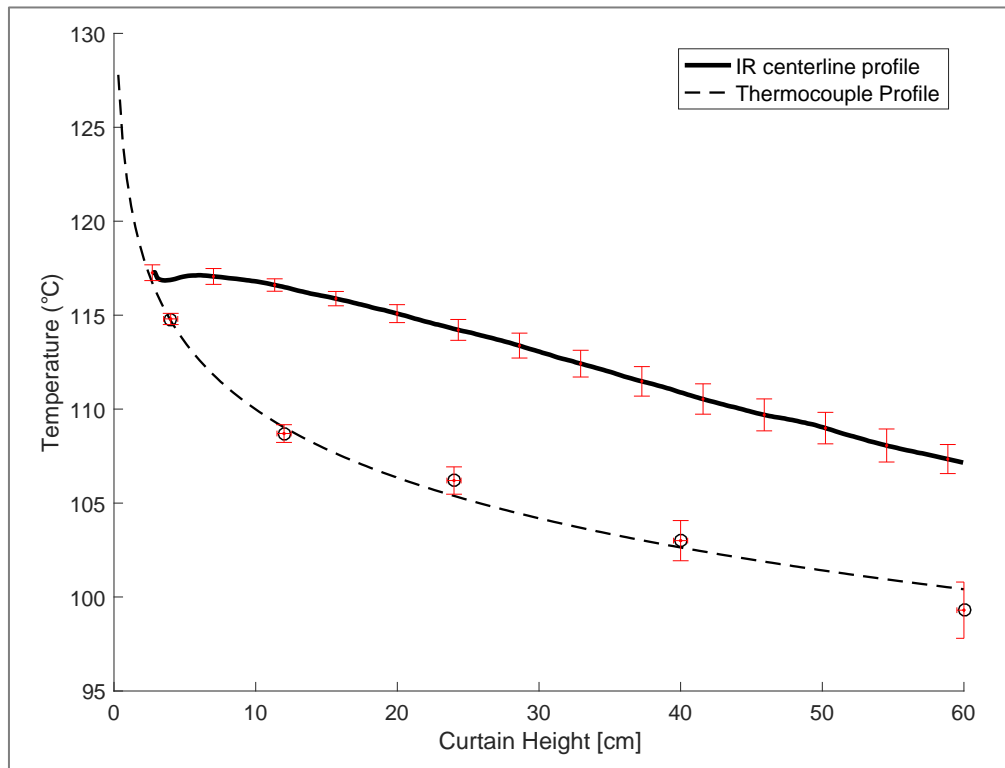
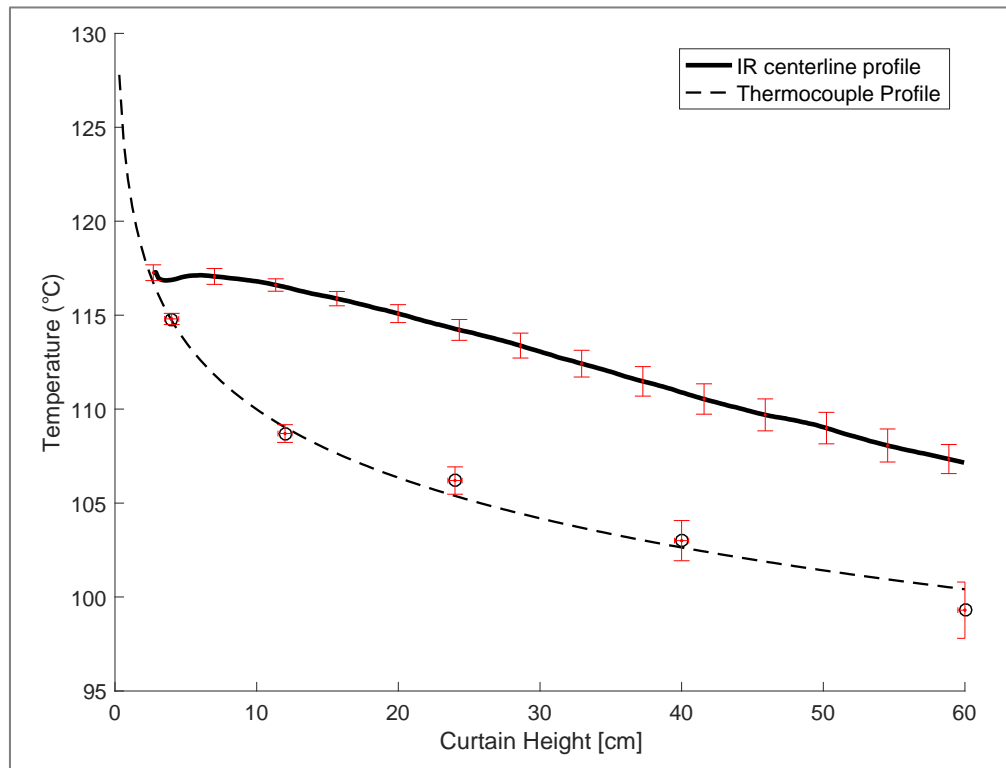
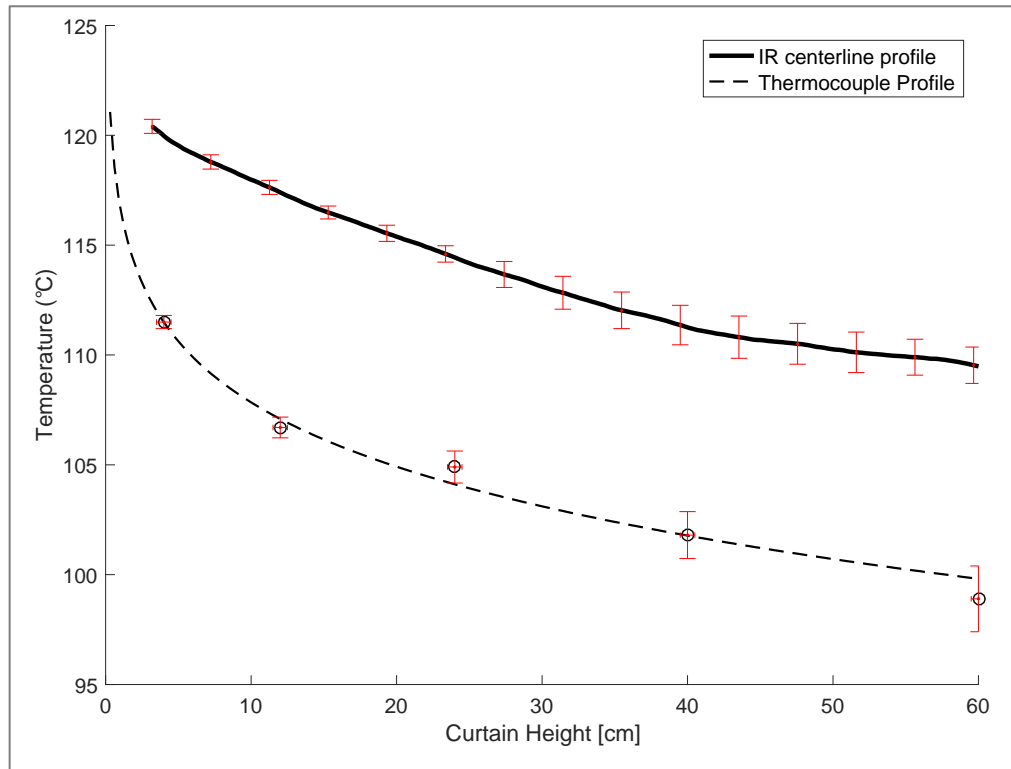


Figure 4.8 and 4.9 present the results of the direct thermocouple and IR temperature profile comparison. Standard deviations (|-|) are included for both measurements. As predicted in Section 4.2, the IR centerline temperature appears to correlate more closely with the 20mm slot width than the 60mm slot width. This was attributed to the comparatively greater solids volume fraction of the 20mm slot width, inhibiting integration of curtain temperature with depth. Due to the IR reading's consistent overestimation of curtain temperature with height, it is strongly implied that temperature is integrated with curtain depth in both scenarios. Crucial elements of this plot include the small 'dip' in the IR centerline profile recorded for the 20mm slot width. This slight divergence at the 4cm mark aligns with the asymmetrical temperature flow observed in Figure 4.7 at point [1]. This further validates that the average 2D temperature field data is a true representation of the system.



**Figure 4.8:** Comparison of IR and thermocouple profile temperatures (with discrete temperatures, 'o') for **20mm** slot width with curtain height.



**Figure 4.9:** Comparison of IR and thermocouple profile temperatures (with discrete temperatures, 'o') for **60mm** slot width with curtain height.

It is also worthy of note that despite uncertainty of the extrapolated ‘zero’ depth for the 20mm slot width, the 60mm IR centerline temperature approaches the same 122°C intercept of the thermocouple profile. Considering the internal hopper temperature was recorded at 124.8°C, this suggests that particles cool by roughly 2.8°C travelling through the 16cm tall spreader box assembly. Recall that the primary influence of taking centreline temperatures equal to the width of the sampling cup was an increase in the temperature gradient with respect to height (Figure 3.25). It is assuring therefore, and particularly useful, to note that the gradients of IR temperature align with those of the thermocouple profiles in Figure 4.8 and 4.9.

To assess where geographically the IR centerline and direct thermocouple temperatures were equal, a two-tailed t-test analysis performed at the 95% confidence interval was undertaken. The dynamic standard deviation was incorporated for the analysis, taken to be that produced from 30 ‘samples’/frames. Table 6 and Table 7 on the following page compile the results of the t-test, which include all direct thermocouple datasets (inclusive of height and depth). If the P-value was greater than 0.5, the null hypothesis was not be rejected and the ‘no’ indicated statistical equivalence between IR and the direct temperature measurement. It can be seen that for both slot widths there was good agreement between the IR centerline temperature and all direct temperatures at a 4cm height. This is unsurprising, as Section 4.1 outlined the marginal temperature difference of both slot width temperatures at this height. However, the best match between datasets at a height of 60cm occurred at different depths. The 20mm IR temperature best aligned with the temperature at 0.5cm depth, whereas the 60mm slot width aligned with the temperature at 1.5cm depth. It is important to recognize that it is inaccurate to assume that the 20mm and 60mm slot width were reading at depths of 0.5cm and 1.5cm respectively. They are in fact the IR camera will sample slightly further into the curtain. The reading is reduced from the cooler particles residing in the forefront of the curtain. However, this outcome suggests that at lower mass flow rates the integration depth will become far more significant.

**Table 6:** T-test results comparing 20mm slot width thermocouple and IR temperatures

Depth of Thermocouple Measurement (cm)	Height (cm)	Temperature (°C)	T-stat	P-Two-tail	Null Hypothesis Rejected?
0	4	114.8	0.41	0.71	<b>no</b>
	12	108.7	3.02	0.01	yes
	24	106.2	7.85	0.00	yes
	40	103.0	16.55	0.00	yes
	60	99.3	20.27	0.00	yes
0.5	4	115.8	0.21	0.85	<b>no</b>
	12	-	-	-	-
	24	-	-	-	-
	40	-	-	-	-
	60	106.9	0.73	0.47	<b>no</b>
1.5	4	117.2	0.07	0.95	<b>no</b>
	12	-	-	-	-
	24	-	-	-	-
	40	-	-	-	-
	60	112.5	13.67	0.00	yes
3	4	117.8	0.19	0.86	<b>no</b>
	12	-	-	-	-
	24	-	-	-	-
	40	-	-	-	-
	60	116.2	23.19	0.00	yes
8	4	117.9	0.21	0.85	<b>no</b>
	12	-	-	-	-
	24	-	-	-	-
	40	-	-	-	-
	60	116.3	23.45	0.00	yes

**Table 7:** T-test results comparing 60mm slot width thermocouple and IR temperatures

Depth of Thermocouple Measurement (cm)	Height (cm)	Temperature (°C)	T-stat	P-Two-tail	Null Hypothesis Rejected?
0	4	111.5	1.61	0.17	<b>no</b>
	12	106.7	4.31	0.00	yes
	24	104.9	7.27	0.00	yes
	40	101.8	20.65	0.00	yes
	60	98.9	33.52	0.00	yes
0.5	4	115.3	0.89	0.41	<b>no</b>
	12	-	-	-	-
	24	-	-	-	-
	40	-	-	-	-
	60	102.4	22.46	0.00	yes
1.5	4	117.7	0.44	0.68	<b>no</b>
	12	-	-	-	-
	24	-	-	-	-
	40	-	-	-	-
	60	109.1	1.29	0.22	<b>no</b>
3	4	118.2	0.35	0.74	<b>no</b>
	12	-	-	-	-
	24	-	-	-	-
	40	-	-	-	-
	60	114.5	15.77	0.00	yes
8	4	118.4	0.31	0.77	<b>no</b>
	12	-	-	-	-
	24	-	-	-	-
	40	-	-	-	-
	60	116.7	22.72	0.00	yes

### 4.3.1 Influence of Emissivity

As previously discussed, emissivity can have a significant impact on the obtained IR temperature. A reflection is presented here on the influence of the chosen emissivity, post data analysis. A single IR test was run with the in-camera emissivity set to 1.00, in place of the determined 0.89 (Figure 4.10). Comparison of the two profiles revealed exceptionally different trends: a substantial 8°C difference at 4cm height, narrowing to 2°C at 50cm. Unknowingly, the apparent intercept of the curves with the zero point actually validated the experimentally determined emissivity. This is because the hopper contents were equilibrated to 124.8°C, and intercepts of direct temperature measurements suggested a temperature at zero height lies around 122°C (some minor cooling occurs whilst passing through the spreader box). This corresponds to the intercept of the 0.89 emissivity curve when extrapolated. Once confidence is held in the direct temperature measurements of the particle curtain therefore, this method could be used as an alternative and/or supplementary method to calibrate particulate emissivity.

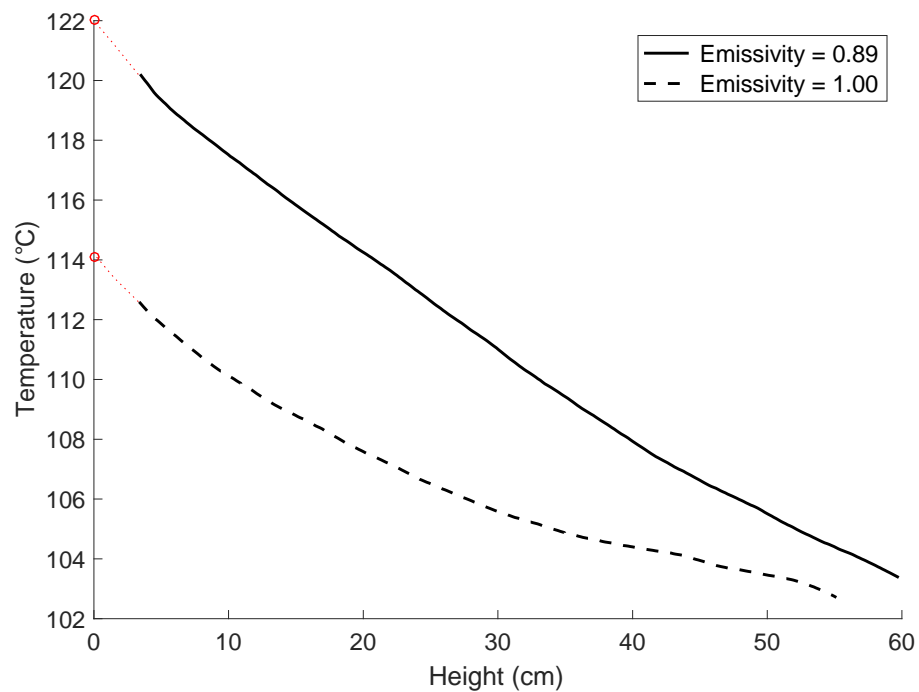


**Figure 4.10:** Adjusted IR centerline temperature from change in emissivity value. Extrapolated intercepts, ‘o’, also presented.

## 4.4 Edge Detection Methods

This chapter presents raw IR and VIS images with various edge detection methods overlaid on them, to see if a superior edge detection technique could be found.

### 4.4.1 VIS Image Edges via Thresholding

Figure 4.11 compares the two-level thresholded images for the 20mm and 60mm curtain. As predicted from the literature review, the larger slot width induced convergent curtain behavior and the smaller slot width induced divergent behavior. It is also apparent that despite the same Gaussian smoothing applied to each, the outer curtain edge of the 60mm slot width (Figure 4.11(b)) appears more irregular. The reduced ability of Ostu's thresholding method to distinguish between the particles and background suggest that the volume fraction declines more steadily from the curtain centerline outwards for the 60mm than for the 20mm slot width. This could evolve as a limitation of the technique when applied to wider slot widths.



**Figure 4.11** Two-level threshold image of 20mm slot width (a) and 60mm slot width (b) curtain

## 4.5 VIS Image Edges vs. IR Image Edges

The results of the VIS Image edges as determined by thresholding are presented in Figure 4.12. These plots are primarily used to distinguish the uniformity of the temperature segregation over the edges. That is, the consistency in the temperature and therefore colour at the location where the edge was anticipated. For both the 20mm slot width (Figure 4.12(a)) and the 60mm (Figure 4.12(b)) it was very clear that the inner curtain edges produced by the threshold method aligned consistently with the hot internal curtain region, where  $T > 110^{\circ}\text{C}$ . Unlike the outer curtain edge prediction, the inner edge closely tracked the  $110^{\circ}\text{C}$  curtain interface, except nearest the spreader box outlet. Comparatively the outer width incorporated more inconsistencies: the intermediate solids volume fraction region generally lumped temperatures of  $70\text{-}90^{\circ}\text{C}$ , but stoops to a lower  $60^{\circ}\text{C}$  on the left-hand side. The VIS edge cannot be guaranteed to work within 3cm of the spreader box outlet due to parallax error.

The IR curtain edges found by differentiation of the temperature data and subsequent curve fitting (described in Section 3.3.1.3.3) exhibit distinctive behavioural changes to the VIS image edges. Firstly, they are incapable of detecting the existence of a second intermediate region of solids volume fraction in the enclosing the curtain. These are represented by the white lines shown at an offset to the curtain in Figure 4.12(c) and (d), which are the second polynomial root solutions and as shown are physically meaningless. Secondly they predict the location of the curtain edge to be between the inner and outer curtain edge predicted by the thresholding technique.

Visible image thresholding methods appear to provide a noteworthy advantage in their distinction of asymmetries in the particulate flow; the averaged VIS images distinguish that at 8cm height there is a notable re-entry of particles from the outer curtain width to the inner on the right-hand side (Figure 4.12(a)). It was therefore theorised that the VIS image threshold technique responds better to the irregularities of the system, in comparison to the IR predicted edges.

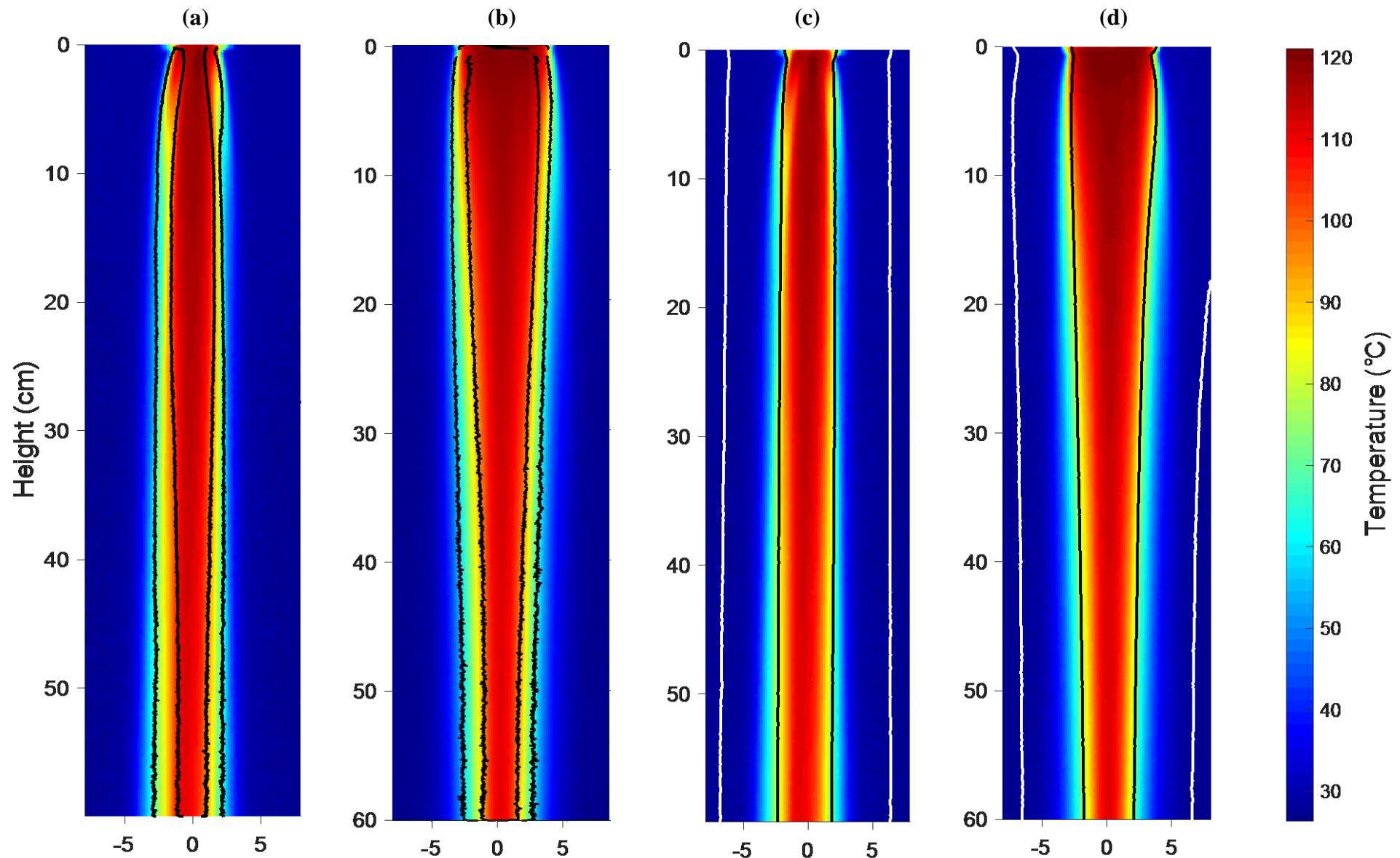


**Figure 4.12:** VIS edge detection via thresholding for 20mm (a) & 60mm (b) slot width, overlaid onto raw IR image. Also IR edges predicted via 70 temperature differentiation for 20mm (a) & 60mm (d), where black and white lines correspond to 1<sup>st</sup> and 2<sup>nd</sup> roots of the polynomial respectively.

## 4.6 Bulk Curtain Temperature

The centerline temperature profiles of the 20mm and 60mm slot width are presented in Figure 4.13. Centerline temperatures performed exactly as expected, with the 60mm curtain improving the heat loss experienced by the centerline particles due to its lower solids volume fraction. However, comparisons of the bulk heat transfer have, up until now, remained unknown.

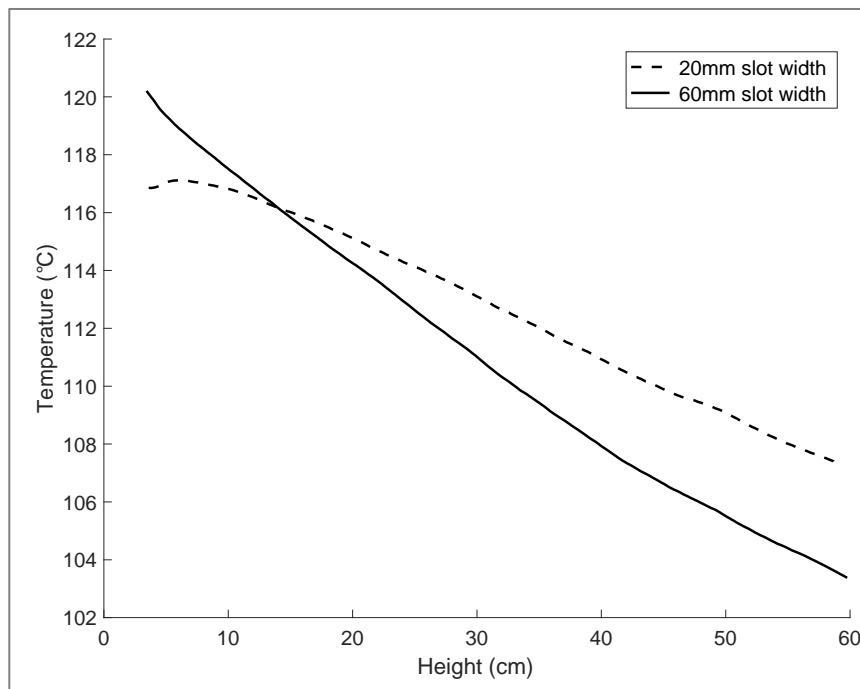


**Figure 4.13:** Centerline profile of the convergent (60mm) and divergent (20mm) particle curtain

Results of the thermochemical experiment into the bulk heat transfer are listed in Table 8. Since the 20mm curtain transferred the least heat to the water sample during the test, it must have experienced the best overall heat transfer. Subtraction of the bulk temperature change in the water from the approximate initial particle temperature at the outlet ( $122.0^{\circ}\text{C}$ ) gave rough values for the particles' heat loss during descent. Results have proved that despite the preferable centerline temperature cooling shown by the 60mm slot width (Figure 4.13), practically the 20mm slot width will achieve superior particulate heat transfer at the experimental conditions applied in this thesis. From the results, the validity of the chosen silica bead heat capacity appears to be a good approximation (since  $\Delta T \approx 10^{\circ}\text{C}$ ). Heat loss effects by heat transfer during the test to the atmosphere are not quantified, however should be considered in future thermochemical experiments. Unfortunately due to the availability of silica beads, this test could not be repeated and the result statistically confirmed. This small experiment does confirm however that thermochemical methods can be explored in future investigations.

**Table 8:** Results of assessment of silica temperature change during descent

Slot Width	Ambient Temperature (°C)	Relative Humidity (%)	ΔT Water (°C)	Bulk ΔT of Silica in H <sub>2</sub> O (°C)	Bulk ΔT of Silica during fall (°C)
20mm	24.0	81.8%	8.7	111.1	10.9
60mm	24.6	79.5	9.2	117.5	4.5

## 4.7 Summary

The effect of slot width on IR imaging, such as temperature integration by the IR camera, has been explored and confirmed. Various image edge detection methods were also completed with reasonable success. A new approach taken to determine the edges of two-level image thresholding by Otsu's method captured and new, previously undefined curtain characteristics. Finally, thermochemical assessment of the bulk curtain heat transfer in comparison to the IR centerline temperatures of each slot were completed. These suggest that the diverging 20mm slot width behavior is the preferable choice to optimize heat-exchanging applications.

## 5.0 Conclusions and Recommendations

Concluding this investigation, there is undoubtedly improved confidence in the presented methodologies to capture particle curtain characteristics. Experimental apparatus modified from previous research into particle curtain behavior was confirmed to have improved consistency.

Analysis into equipment practices followed to obtain uniformly heated silica samples eliminated variability in subsequent experiments. For example, previously observed upwards sloping of direct thermocouple temperature after apparent stabilisation was completely eliminated. The new sampling cups tailor-made for specific mass flow rates (i.e. locations within the curtain) improved the consistency of mass hold-up, as well as the speed at which temperature stabilised. Accordingly, relatively small standard deviations were recorded in these typically sensitive parameters. This, in turn, meant subtle fluctuations in curtain properties were identifiable. For example, the addition of the internal hopper thermocouple became extremely valuable in excluding sensitive outlying datasets.

A strong focus on the applied optical physics regarding IR thermography led to a renewed focus on camera calibration techniques. Specifically, approaches to determine emissivity were described in detail. This was because methodologies that may be used to obtain emissivities of power-like samples not commonly investigated without specialised equipment and at relatively low temperatures. An accurate but seemingly imprecise value of 0.89 for particulate emissivity was determined using a simple in-camera calibration technique. To the credit of later image analysis however, the extrapolation of IR centerline profiles taken at an emissivity of 0.89 aligned with the hypothesized outlet temperature from the spreader box ('zero' height). This provided renewed confidence in the original measurement.

The effect of slot width on IR imaging, such as temperature integration by the IR camera, has been explored. Even at relatively high mass flow rates used in this thesis ( $\sim 0.160\text{kg/s}$ ), the tendency of curtains to decrease solids volume with descent lead to distinctly different integration depths. That is, a statistical analysis performed on the agreement of IR centerline temperature with curtain depth revealed the IR camera was integrating at a greater depth than for the 20mm slot width. This brings into question the validity of IR imaging at small mass flow rates and small particle sizes; a single camera pixel's FOV will be too small to detect any meaningful temperature data, as the background integration will be incredibly high.

Image processing techniques, such as two-level image thresholding, have demonstrated great potential in describing the characteristic behavior of particle curtains. Specifically, this technique showed great promise in distinguishing inner and outer edges of both convergent and divergent

particle curtains.

Various image edge detection methods were also completed with reasonable success. New approaches, such as two-level image thresholding by Otsu's method, captured new and previously undefined curtain characteristics. It was difficult however to compare the validity of the edges without CFD modeling. Finally, thermochemical assessment of the bulk curtain heat transfer in comparison to the IR centerline temperatures of each slot were completed. These confirmed that the diverging 20mm slot width behavior is the preferable choice to optimize heat-exchanging applications.

The application of MATLAB software and image processing toolboxes were successfully employed to develop efficient VIS and IR image scaling processes. Moreover, MATLAB proved to be an invaluable tool in analyzing and integrating multiple images simultaneously. The applied image integration technique was shown to mitigate the effects of curtain 'wobbling' in smoothed 2D field profiles and average curtain edges.

The conclusions of this thesis align with those of previous studies undertaken in this area; namely that the inherent nature of IR imaging is likely to make obtaining accurate thermographic data under certain conditions (i.e. low mass flow rates difficult). Nevertheless, new approaches to accurately determine the bulk behavior of particle curtains were highly successful.

Based on the findings discussed in this thesis, the following recommendations have been made.

- Two-level thresholding has highlighted that converging behavior is present in both the converging and diverging curtains (20mm and 60mm slot width). This behavior has previously been ignored as the particles simply shift from intermediate to high solids volume fraction, which is imperceptible when a single threshold value is applied. Distinguishing between the curtain bulk and the fuzz could have important implications in characterising curtain trends.
- The methodology behind the developed image scaling procedure should be applied in subsequent investigation into conducting image analyses of particle curtain. MALTAB image scaling processes could be easily converted to a guided user interface (GUI). This would make the process user-friendlier, thereby not requiring knowledge of the programming language to make adjustments.

- Curve-fitting techniques performed in MATLAB to generalize thermocouple temperature trends was highly successful. The potential for the program to incorporate weighted datasets (i.e. variable levels of confidence for various data points) in the regression analysis could be highly beneficial in this area
- Monte Carlo simulation could be used to model and draw conclusions on the true integration depth of the IR camera. Such methods could also be used to determine the critical mass flow rate at which the background significantly influences the thermographical measurement
- The edge detection of particle curtains using standard image capture (red-green-blue: RGB) as opposed to grayscale should be assessed. If results are positive, then video capture should be used in place of image capture. This format offers faster frame speed that could be used to perform complex time-dependent analyses, which can confirm the accuracy of two-level threshold techniques.

## 6.0 References

- [1] A. Lee, "Modelling the solids transport phenomena within flighted rotary dryers," James Cook University, 2008.
- [2] M. E. Sheehan, P. F. Britton, and P. A. Schneider, "A model for solids transport in flighted rotary dryers based on physical considerations," *Chemical Engineering Science*, vol. 60, pp. 4171-4182, 8// 2005.
- [3] J. Christian and C. Ho, "System design of a 1 MW north-facing, solid particle receiver," *Energy Procedia*, vol. 69, pp. 340-349, 2015.
- [4] P. Viebahn, Y. Lechon, and F. Trieb, "The potential role of concentrated solar power (CSP) in Africa and Europe—A dynamic assessment of technology development, cost development and life cycle inventories until 2050," *Energy Policy*, vol. 39, pp. 4420-4430, 8// 2011.
- [5] A. Oles, "Modeling of Falling-Particle Solar Receivers for Hydrogen Production and Thermochemical Energy Storage," 2014.
- [6] S. Afshar and M. Sheehan, "Using cfd to simulate heat transfer in particle curtains," 2012.
- [7] M. Giot, F. Mayinger, and G. Celata, "INFRARED THERMOGRAPHY AND CONVECTIVE HEAT TRANSFER," 1997.
- [8] J. Živčák, R. Hudák, L. Madarász, and I. J. Rudas, *Methodology, Models and Algorithms in Thermographic Diagnostics* vol. 5: Springer Science & Business Media, 2013.
- [9] S. Afshar, "Modelling and Infrared Thermal Imagery of Hot Particle Curtains," Doctor of Philosophy, College of Science, Technology and Engineering, James Cook University, 2015.
- [10] T. Dang, T. Kolkman, F. Gallucci, and M. van Sint Annaland, "Development of a novel infrared technique for instantaneous, whole-field, non invasive gas concentration measurements in gas–solid fluidized beds," *Chemical Engineering Journal*, vol. 219, pp. 545-557, 2013.
- [11] A. V. Patil, E. A. J. F. Peters, V. S. Sutkar, N. G. Deen, and J. A. M. Kuipers, "A study of heat transfer in fluidized beds using an integrated DIA/PIV/IR technique," *Chemical Engineering Journal*, vol. 259, pp. 90-106, 1/1/ 2015.
- [12] M. Lisboa, D. Vitorino, W. Delaiba, J. Finzer, and M. Barrozo, "A study of particle motion in rotary dryer," *Brazilian Journal of Chemical Engineering*, vol. 24, pp. 365-374, 2007.
- [13] N. Siegel, M. Gross, C. Ho, T. Phan, and J. Yuan, "Physical Properties of Solid Particle Thermal Energy Storage Media for Concentrating Solar Power Applications," *Energy*

- Procedia*, vol. 49, pp. 1015-1023, // 2014.
- [14] G. J. Kolb, R. B. Diver, and N. Siegel, "Central-station solar hydrogen power plant," *Journal of Solar Energy Engineering*, vol. 129, pp. 179-183, 2007.
  - [15] R. Bradshaw and R. Carling, "A review of the chemical and physical properties of molten alkali nitrate salts and their effect on materials used for solar central receivers," Sandia National Labs., Livermore, CA (USA)1987.
  - [16] J. Hruby, R. Steeper, G. Evans, and C. Crowe, "An experimental and numerical study of flow and convective heat transfer in a freely falling curtain of particles," *Journal of fluids engineering*, vol. 110, pp. 172-181, 1988.
  - [17] O. Ajayi and M. Sheehan, "Design loading of free flowing and cohesive solids in flighted rotary dryers," *Chemical engineering science*, vol. 73, pp. 400-411, 2012.
  - [18] B. R. Munson, T. H. Okiishi, W. W. Huebsch, and A. P. Rothmayer, *Fundamentals of Fluid Mechanics*, 6 ed.: Wiley, 2012.
  - [19] C. Wardjiman and M. Rhodes, "Heat transfer in a particle curtain falling through a horizontally-flowing gas stream," *Powder Technology*, vol. 191, pp. 247-253, 2009.
  - [20] A. Rogalski, "Infrared detectors for the future," *Acta Physica Polonica-Series A General Physics*, vol. 116, p. 389, 2009.
  - [21] "Basic Principles of Non-Contact Temperature Measurement," Optis Infrared Thermometers, Ferdinand-Buisson-Str.14 Berlin Germany2008.
  - [22] K.-D. Gruner, "Principles of Non-Contact Temperature Measurement," R. GmgH, Ed., ed. Berlin, Germany: Raytek(R), 2013.
  - [23] S. L. Brown and B. Y. Lattimer, "Transient gas-to-particle heat transfer measurements in a spouted bed," *Experimental Thermal and Fluid Science*, vol. 44, pp. 883-892, 2013.
  - [24] T. Tsuji, T. Miyauchi, S. Oh, and T. Tanaka, "Simultaneous measurement of particle motion and temperature in two-dimensional fluidized bed with heat transfer," *KONA Powder and Particle Journal*, vol. 28, pp. 167-179, 2010.
  - [25] V. Borodulya, V. Ganzha, Y. S. Teplitskii, and Y. G. Epanov, "Heat transfer in fluidized beds," *Journal of Engineering Physics and Thermophysics*, vol. 49, pp. 1197-1202, 1985.
  - [26] J. Valenzuela and L. Glicksman, "An experimental study of solids mixing in a freely bubbling two-dimensional fluidized bed," *Powder technology*, vol. 38, pp. 63-72, 1984.
  - [27] T. Pugsley, H. Tanfara, S. Malcus, H. Cui, J. Chaouki, and C. Winters, "Verification of fluidized bed electrical capacitance tomography measurements with a fibre optic probe," *Chemical Engineering Science*, vol. 58, pp. 3923-3934, 2003.
  - [28] C. Wardjiman, A. Lee, M. Sheehan, and M. Rhodes, "Shape of a particle curtain falling in stagnant air," *Powder Technology*, vol. 192, pp. 384-388, 6/25/ 2009.
  - [29] S. Ray, *Scientific photography and applied imaging*: CRC Press, 2015.
  - [30] F. P. Incropera, A. S. Lavine, T. L. Bergman, and D. P. DeWitt, *Principles of heat and*

- mass transfer*: Wiley, 2013.
- [31] E. Gregersen, *The Britannica guide to sound and light*: Britannica Educational Publishing, 2010.
- [32] F. T. Ulaby, E. Michielssen, and U. Ravaioli, *Fundamentals of Applied Electromagnetics 6e*: Prentice Hall, 2001.
- [33] Cyberphysics.com.uk. (2016). *The Electromagnetic Spectrum: the family of light*. Available: <http://www.cyberphysics.co.uk/topics/light/emspect.htm>
- [34] M. Vollmer and K.-P. Möllmann, *Infrared thermal imaging: fundamentals, research and applications*: John Wiley & Sons, 2010.
- [35] M. M. Rathore and R. Kapuno, *Engineering heat transfer*: Jones & Bartlett Publishers, 2011.
- [36] R. Usamentiaga, P. Venegas, J. Guerediaga, L. Vega, J. Molleda, and F. G. Bulnes, "Infrared thermography for temperature measurement and non-destructive testing," *Sensors*, vol. 14, pp. 12305-12348, 2014.
- [37] L. NEC Avio Infrared Technologies Co., "Infrared Thermography H2600 Series Operation Manual."
- [38] M. Sezgin, "Survey over image thresholding techniques and quantitative performance evaluation," *Journal of Electronic imaging*, vol. 13, pp. 146-168, 2004.
- [39] (2016, 6/10/16). *Intensity-Based Segmentation (Thresholding) (Biomedical Image Analysis)*. Available: <http://what-when-how.com/biomedical-image-analysis/intensity-based-segmentation-thresholding-biomedical-image-analysis/>
- [40] B. S. Morse, "Lecture 4: Thresholding," *Brigham Young University*, 2000.
- [41] M. S. van Buijtenen, M. Börner, N. G. Deen, S. Heinrich, S. Antonyuk, and J. Kuipers, "An experimental study of the effect of collision properties on spout fluidized bed dynamics," *Powder technology*, vol. 206, pp. 139-148, 2011.
- [42] C. Wardjiman, A. Lee, M. Sheehan, and M. Rhodes, "Behaviour of a curtain of particles falling through a horizontally-flowing gas stream," *Powder Technology*, vol. 188, pp. 110-118, 2008.
- [43] R. Goetsch and J. Regele, "Discrete element method prediction of particle curtain properties," *Chemical Engineering Science*, vol. 137, pp. 852-861, 2015.
- [44] (2016, 26th April 2016). *Mastersizer 3000*. Available: <http://www.malvern.com/en/products/product-range/mastersizer-range/mastersizer-3000/>
- [45] S. Dawson, B. Harris, and C. Davies, "Characteristics of Venturi feeders for powders," in *Chemeca 89: Technology for Our Third Century; the Seventeenth Australasian Chemical Engineering Conference*, 1989, p. 890.
- [46] F. Kreith, R. M. Manglik, and M. S. Bohn, *Principles of heat transfer*: Cengage learning, 2012.

*This page is left intentionally blank.*

## Appendix 1, Risk Assessment for Mastersizer3000



Townsville Campus

College of Science, Technology and Engineering

**Risk Assessment**
**Name of Test:** Using the Mastersizer to measure the size of silica bead samples

<b>Purpose:</b> Thesis Testing				
<b>Operator:</b> Laura Kuskopf	<b>Duration:</b> March 2016			
<b>SDS Attached:</b> (Tick one) <input checked="" type="checkbox"/> Yes	No	N/A		
<b>Major Hazard Types:</b> (Tick at least one)				
Chemical	Mechanical			
<input checked="" type="checkbox"/> Electrical	Thermal			
<input checked="" type="checkbox"/> Environmental	Other:			
<b>SUMMARY OF RISKS</b>				
Specific Task/Activity	Potential Hazards/Consequences	Assessed Risk	Risk Control Measures	Reassessed Risk
Use of silica beads / solutions	They may make the floors slippery if sample spills (TRIP HAZARD) Broken glassware could cause injury.	MEDIUM	- Contain particles in beaker - Handle glassware with care & tread responsibly - Maintain good housekeeping - Wear appropriate PPE (safety glasses, lab coat, enclosed shoes)	LOW
Use of electrical equipment (Mastersizer)	Electrocution	MEDIUM	- Dry surfaces - Maintain good housekeeping - Check test and tag is current	LOW

**SUMMARY OF REQUIREMENTS**

<b>Personal Protective Equipment</b>	Safety glasses, enclosed shoes, lab coat
<b>Is Training Required</b>	No
If YES, please state requirements	

**SUMMARY OF ACTIVITY**

- Diluting a sample of the silica beads
- Calibrating the machine and entering necessary data into the software program
- Running sample through the Mastersizer
- Rinsing the machine
- Cleaning & packing away all glassware

**ASSESSMENT:****OPERATOR** (Student or Technician):Laura Kuskopf

Name



Date: 8/03/16 Contact No: 0438306943

**SUPERVISOR:**Madoc Sheehan

Name



Date: 8/03/16 Contact No: 47814153,

Signature

**SAFETY ADVISOR:**Ruiyan Liu

Name



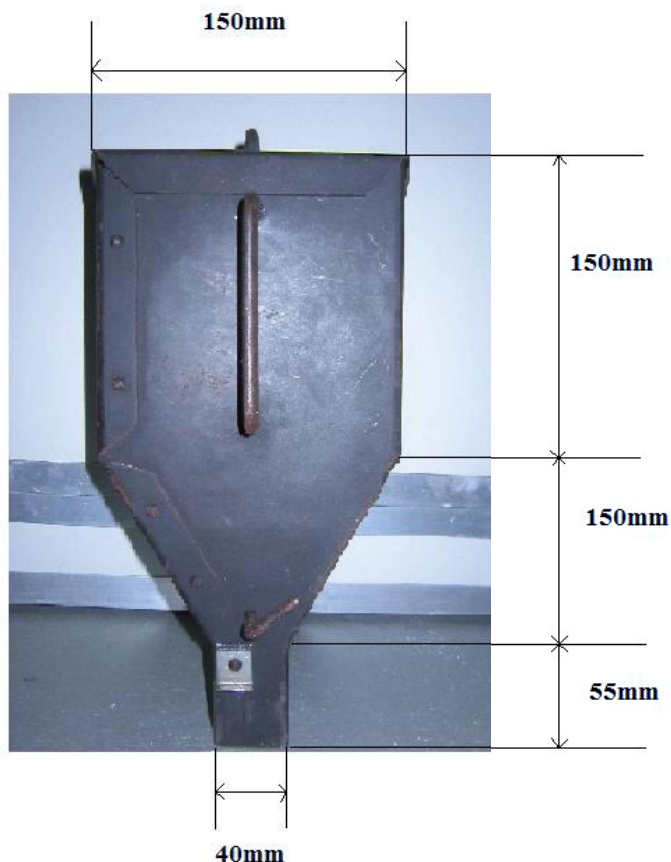
Date: 8/03/16 Contact No: 47814752

Signature

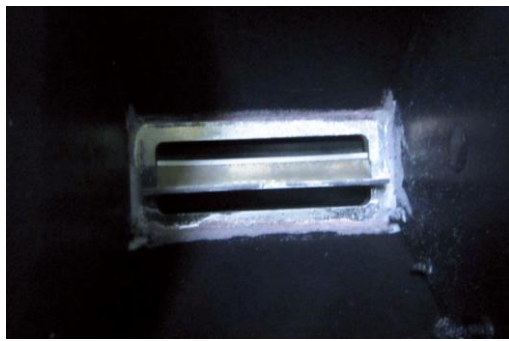
THIS FORM IS TO BE DISPLAYED IN THE IMMEDIATE VICINITY OF THE EXPERIMENT BEING UNDERTAKEN

## Appendix 2, Hopper Specifications

Hopper Dimensions



Opened Hopper Valve

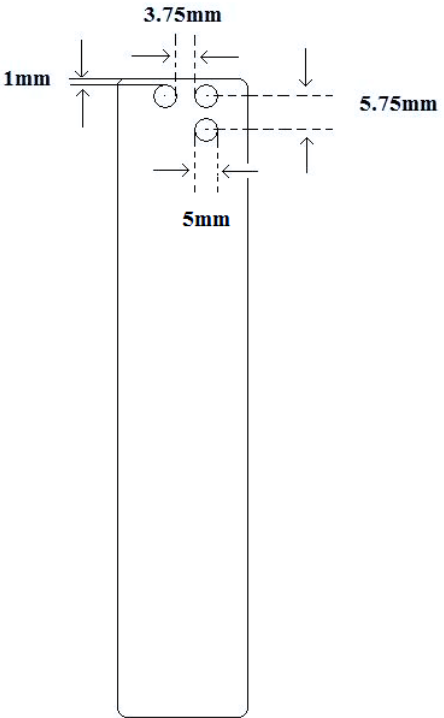
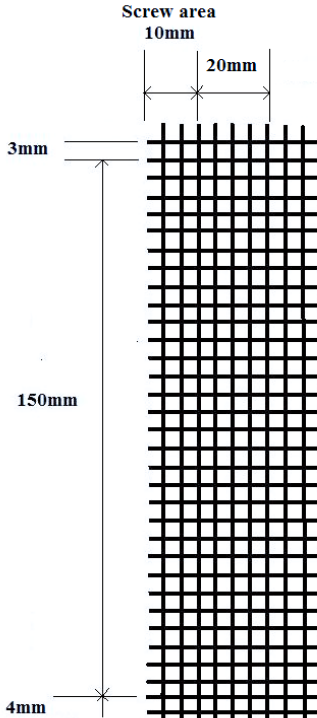


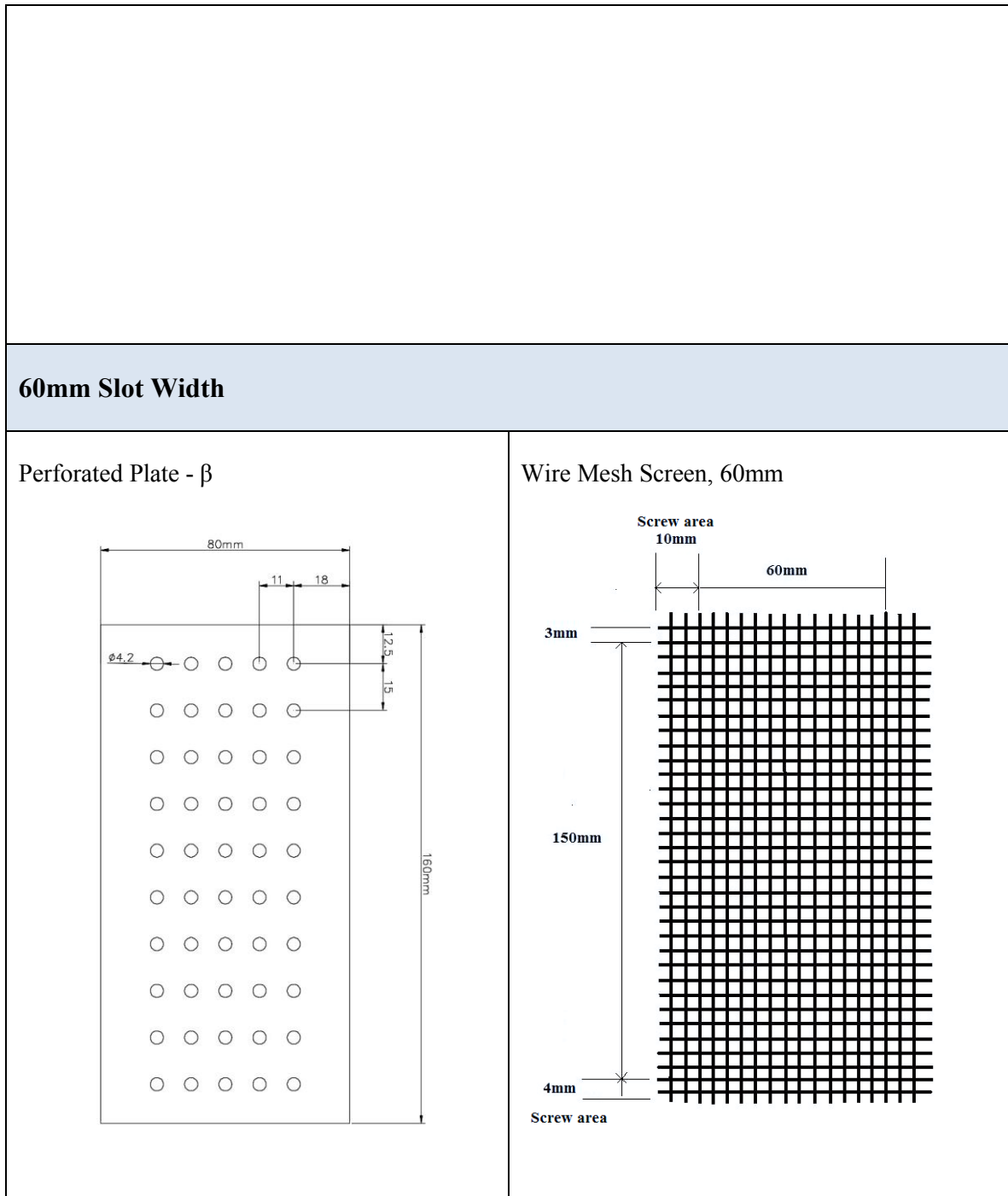
Closed Hopper Valve



## Appendix 3, Spreader Box Assembly Specifications

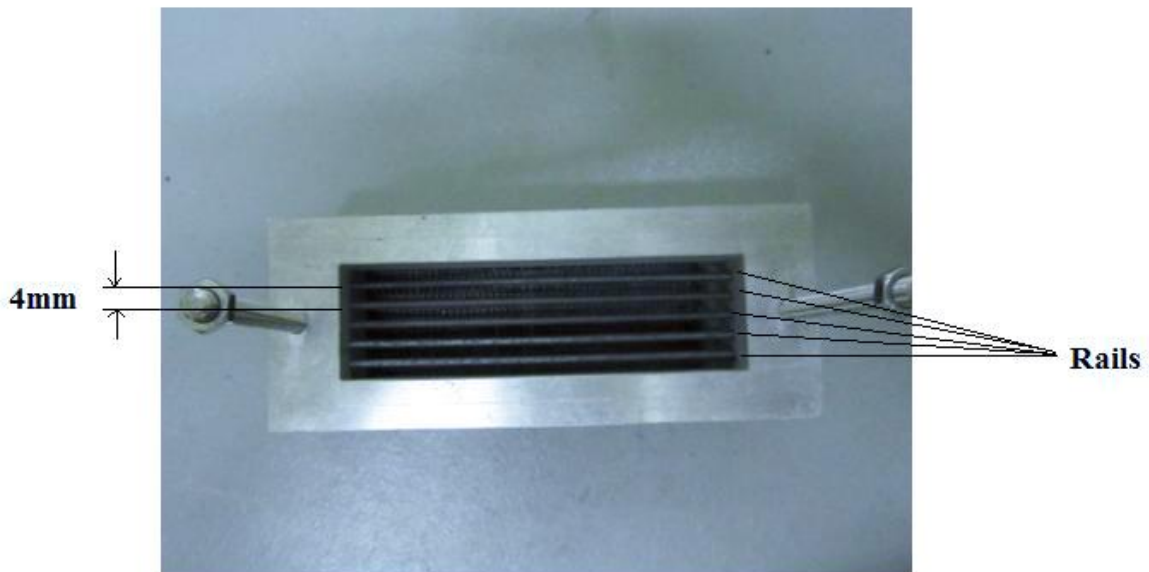
Some dimensioned equipment sketches were sourced from Afshar [9] Appendix C.

<b>20mm Slot Width</b>	
<b>Perforated Plate - <math>\alpha</math></b> 	<b>Wire Mesh Screen, 20mm</b> 
<b>Frontal View of Spreader Box</b> 	



**60mm Slot Width, cont.**

Top View of Rails



## Appendix 4, General Experimental Process

The process of preparing the experimental apparatus and generating a particle curtain is outlined below.

- 1) Closed hopper valve. Used scales to fill hopper with 4.2kg of glass beads from silica beads bucket and sealed hopper with lid.
- 2) Placed entire apparatus (including spreader box assembly) into oven maintained at 120C for at least 10 hours.  
*[Depending on the objective, this time was used to calibrate the IR camera or attach sampling cups at the required height with a retort stand from the spreader box exit]*
- 3) Turned on laptop. Initiated data recording by IR/VIS image camera and scale indicator
- 4) Removed apparatus from oven. Immediately carried spreader box to stand and fastened. Placed hopper in the spreader box.
- 5) Opened valve fully, standing to the side of the hopper (outside camera frame)
- 6) Waited for the contents of the hopper to empty (roughly 50 seconds)
- 7) Concluded data recording. Turned off camera/s and laptop.
- 8) Waited 30 minutes for hopper to cool. Scooped beads from collector receiver back into bucket.

## Appendix 5, Risk Assessment for General Methodology



Townsville Campus

College of Science, Technology and Engineering

**Risk Assessment**

Name of Test: Using the infrared camera to measure heat transfer in particle curtains

<b>Purpose:</b> Thesis Testing		<b>Duration:</b> March 2016 – October 2016
<b>Operator:</b> Laura Kuskopf	<b>SDS Attached:</b> (Tick one) <input checked="" type="checkbox"/> Yes	<b>No</b> <b>N/A</b>
<b>Major Hazard Types:</b> (Tick at least one)		
Chemical	<input checked="" type="checkbox"/>	Mechanical
<input checked="" type="checkbox"/> Electrical		Thermal
<input checked="" type="checkbox"/> Environmental		Other:

**SUMMARY OF RISKS**

Specific Task/Activity	Potential Hazards/Consequences	Assessed Risk	Risk Control Measures	Reassessed Risk
Example: Use of oven to heat particles	Skin burns (THERMAL HAZARD)	HIGH	- Use of anti-fire gloves for carriage of equipment from oven - Wear overall clothes - Wear full-face protective shield - Wear steel-cap safety shoes - Contain particles in the receiver - Insulate hopper and device	LOW
Use of silica beads	They may make the floors slippery if they are not caught by the receiver (TRIP HAZARD)	MEDIUM	- Vacuum the floor after each test - Contain particles in receiver - Take care & tread responsibly - Place sign over entranceway during experimentation & cool-down time.	LOW
Carrying hopper	The 7-8kg weight may be heavy to carry & result in back strain or impact injury (MANUAL HANDLING)	MEDIUM	- Hopper should be equipped with suitable handles to carry easily - Short distances between oven and device - Use assistant whenever necessary	LOW
Use of electrical equipment	Electrocution	MEDIUM	- Dry surfaces - Maintain good housekeeping - Tidy cords away - Check test and tag is current - If building is not RCD protected provide portable earth leakage protection	LOW

**SUMMARY OF REQUIREMENTS**

<b>Personal Protective Equipment</b>	Anti-fire (long elbow length) gloves, safety glasses, enclosed steel-cap shoes, overall clothes
<b>Is Training Required</b>	No
If YES, please state requirements	
<b>Training Manual Location</b>	Nil

**SUMMARY OF ACTIVITY**

**NOTE:** When undertaking experiment the PPE listed on Page 1 **MUST** be worn.

*This procedure is a TWO OPERATOR PROCEDURE, with an observer required for Steps 10-15.*

1. Ensure hopper valve is FULLY CLOSED
2. Weigh empty hopper
3. Open lid of the silica beads bucket
4. Pour particles into hopper with scoop from the bucket
5. Weigh hopper with glass beads on scale
6. Seal hopper with lid and ensure valve is closed
7. Set oven temperature to reach 120°C
8. Wait 2hrs for temperature to reach 120°C
9. Turn on camera on tripod, load cells and laptop and set heat pads to 160°C

**1. Electrical hazard**

- 
10. Open oven
  11. Grab hopper handles carefully with fire-proof (long elbow length) gloves
  12. Carry hopper to particles receiver
  13. Insert hopper into particle receiver device

**1. Lifting Hazard  
2. Thermal Hazard  
3. Trip hazard**

- 
14. Regulate hopper valve to the desired mass flowrate
  15. Record the load cells using the camera
  16. Turn off laptop, camera, load cells and oven
  17. Wait two hours for hopper to cool

**4. Dust Hazard  
5. Hot particles/burns  
6. Trip hazard**

18. Scoop glass beads from collector receiver into bucket

**ASSESSMENT:****OPERATOR** (Student or Technician):Laura Kuskopf

Name

Signature

Date: /03/16 Contact No: 0438306943

**SUPERVISOR:**Madoc Sheehan

Name

Date: 29/03/16 Contact No: 14153

Signature

**SAFETY ADVISOR:**Shaun Robinson

Name

Signature

Date: 29/03/16 Contact No: 0408531068

THIS FORM IS TO BE DISPLAYED IN THE IMMEDIATE VICINITY OF THE EXPERIMENT BEING UNDERTAKEN

**WORK PRACTICE DATA SHEET - THIS IS A SUMMARY ONLY - FULL REPORT AVAILABLE**

**Location:** Not Available **Chemwatch:** 35766

**NON-HAZARDOUS CHEMICAL. NON-DANGEROUS GOODS. According to the Model WHS Regulations and the ADG Code.**

**GLASS BEADS**

INGREDIENTS	CAS No	%	8hr OEL
glass beads	65997-17-3.	100	

**UN No:** None **Hazchem Code:** **DG Class:** None **Subsidiary Risk:** None **Packing Group:** **Poisons Schedule:** None

**PROPERTIES**

Solid. Does not mix with water. Sinks in water. Does not burn.

**EMERGENCY**

**FIRST AID:**  
**SWALLOWED:** Rinse mouth with water.  
**EYE:** Wash with running water. For discomfort seek medical advice.  
**SKIN:** Wash with soap  
**INHALED:** Fresh air. Rest, keep warm.  
**ADVICE TO DOCTOR:** Treat symptomatically.  
**FIRE FIGHTING:** Keep surrounding area cool. Water spray/fog.  
**SPILLS AND DISPOSAL:** Avoid dust. Sweep shovel to safe place.

**PRECAUTIONS FOR USE**

**GLASSES:** Consider chemical goggles.  
**STORAGE AND TRANSPORTATION:** Store in cool, dry, protected area.

**HEALTH HAZARD INFORMATION**

**ACUTE HEALTH EFFECTS:**  
**CHRONIC HEALTH EFFECTS:**

**SAFE STORAGE WITH OTHER CLASSIFIED CHEMICALS**

+	+	+	+	+	+

X: Must not be stored together  
0: May be stored together with specific preventions  
+: May be stored together

This document is copyright. Apart from any fair dealing for the purposes of private study, research, review or criticism, as permitted under the Copyright Act, no part may be reproduced by any process without written permission from CHEMWATCH. TEL (+61 3) 9572 4700.

## Appendix 6, Flow Rate Consistency

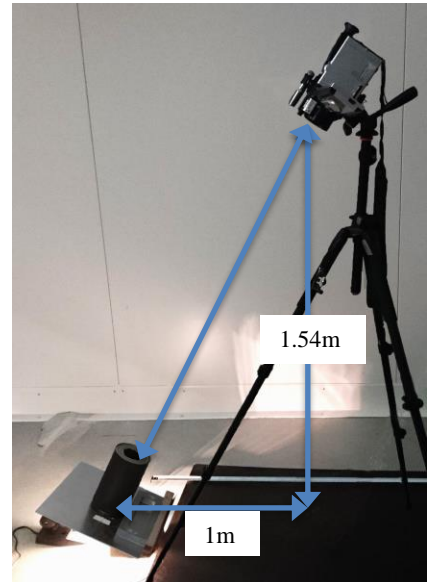
The table below summarises the results of mass flow rate consistency tests performed at ambient conditions.

	Run No.	Mass flow rate (kg/s)	Mean mass flow rate (kg/s)	Flow rate Std. Dev (kg/s)	Relative Humidity (%)	Air Temperature (°C)
20mm	1	0.160	0.160	0.000548	66.7	22.6
	2	0.160			86.3	23.8
	3	0.161			86.4	24.1
	4	0.160			92.6	24.3
	5	0.161			86.0	24.2
60mm	1	0.166	0.166	0.000548	65.7	22.0
	2	0.166			86.7	23.7
	3	0.165			65.2	22.2
	4	0.165			76.1	23.1
	5	0.166			61.7	24.0

## Appendix 7, Emissivity Calibration Steps

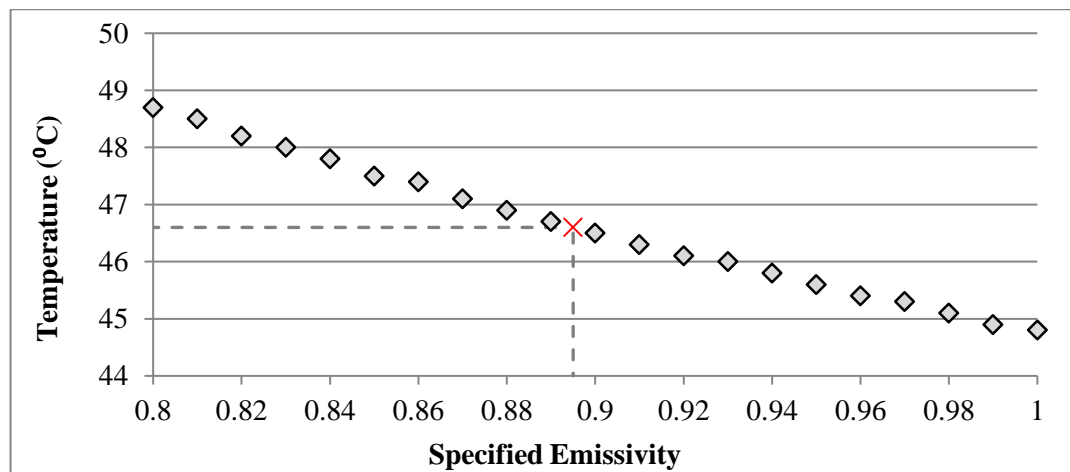
*Described in this appendix are the steps taken to determine the emissivity of the 257 $\mu\text{m}$  silica beads. For details on any in-camera adjustments see manual [ref].*

- 1) Used tape measure to set-up IR camera and metal barrier (holding silica beads), shown at right.
- 2) Inserted T type bead thermocouple into the silica bead sample directly under the surface in the center of the cup. Connected thermocouple to data logger thermometer (SE-378).
- 3) Turned on heat lamp. Left system to equilibrate (with lab door *closed*) for roughly 30 minutes, or until temperature reading from thermocouple remained constant.
- 4) Turned ON IR camera. Performed REF CAL calibration.
- 5) Focused IR camera on the heated silica beads (detectable by sharper image).
- 6) Placed two spot temperatures in the IR view window over the center of the silica beads. Checked they recorded an identical temperature.
- 7) Froze IR image and recorded thermocouple measurement in that instant.
- 8) Adjusted emissivity from 1.00 to 0.80 sequentially in 0.01 increments, recording the in-camera adjustment made to the spot temperatures.
- 9) Repeated steps 7-8 twice more to assess consistency.

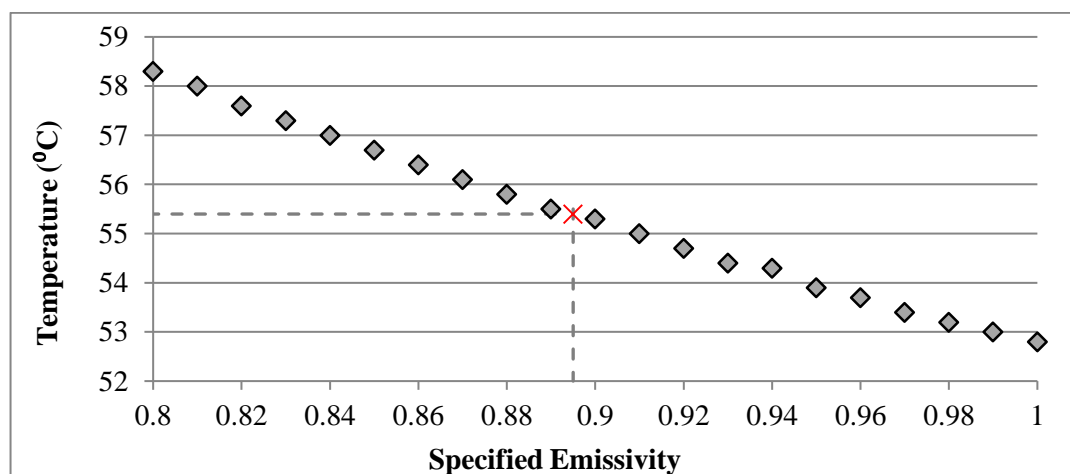


## Appendix 8, Emissivity Graphs

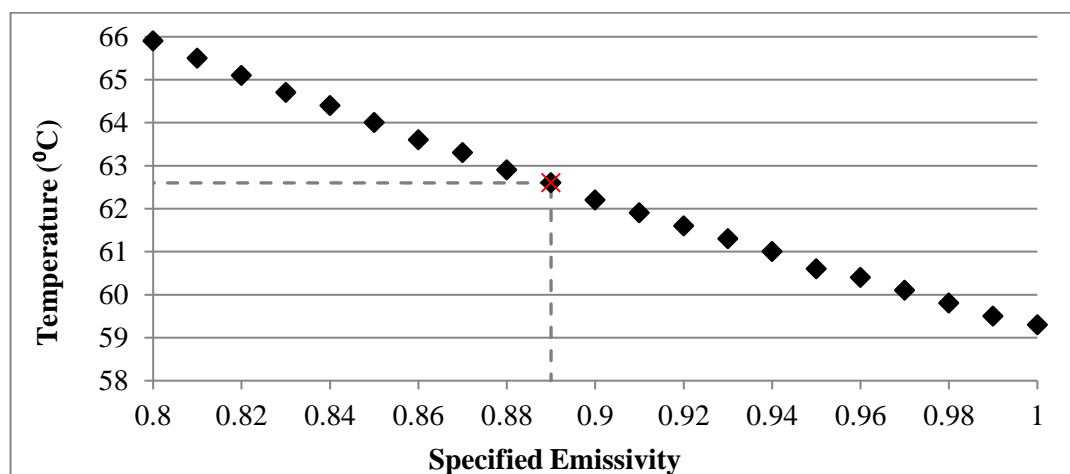
*Run 1 – Silica bead temperature @ 57.6°C*



*Run 2 – Silica bead temperature @ 57.5°C*



*Run 3 – Silica bead temperature @ 57.8°C*



## Appendix 9, MATLAB Code

### Part 1: VIS Image Pre-processing

```

VISIBLE IMAGE (VIS) PROCESSING
%%%%%%%
ACRONYMS --> AOI: 'area of interest',
%%%%%%%
% Input data:
width = 0.054;           % 20mm Spreader box width, [m]
%width = 0.079;          % 60mm Spreader box width, [m]
xmin = 1650;             % Trial & error value for cropping (Step 1)
ymin = 2050;             % " "
angle = 0.5;              % Error in spreader angle to make horiz
CROP = 10;                % Additional pixels cropped of final image
choice1 = 2;               % Initial cond. - don't touch
choice2 = 2;               % Initial cond. - don't touch
%%%%%%%

%%%% Step 1: Import multiple images for processing
d = uigetdir(pwd, 'Select a folder'); % Prompt user to select image folder
A = dir(fullfile(d, '*jpg')); % Make .jpeg files within folder directory
eval(['Vis' num2str(1) '=imread(A(1).name);']); %Get first im

%%%% Step 2: Read FIRST image into workspace & determine scaling factor
% Read greyscale calibration image & rotate
N1 = imrotate(Vis1(:,:,1),270-angle, 'bilinear'); % Rotate image

% Crop image to ROUGH area where spreader box lies:
FOCUS = imcrop(N1, [xmin ymin 380 500]); % [xmin ymin width height]

% Prompt user to select outline of spreader box front for scaling
while choice2 > 1;           % While crop has not been confirmed:
    while choice1 > 1;         % While crop has not been confirmed:
        [BOX, c] = imcrop(FOCUS); % Get dimensions of box
        figure(1), imshow(BOX)    % Show cropped selection
        choice1 = menu('Press yes to submit selection','Yes','Reselect');
    end

    [h,w] = size(BOX);          % Determine width/height of box in pixels
    scale = round(c(3))/width;   % Calculate scaling factor, [pixels/m]

    % Determine scale using spreader box width:
    y_pixels = round(scale * 0.60); % Select 60cm worth of vertical pixels
    x_pixels = round(scale * 0.06); % Select 6.0cm worth of horizontal pixels

    % NB: [ZERO,CENTRE] correspond to pixel co-ords of curtain midpoint @ exit
    ZERO = round(ymin + c(2) + c(4)); % Find location of "0" height
    CENTER = round(xmin + c(1) + 0.5*c(3)); % Find location of center

    figure(2), imshow(FOCUS)      %Show user selection of midpoint/center
    hold on;
    plot([0,380],[ZERO-ymin,ZERO-ymin],'Color','r','LineWidth',2)
    plot([CENTER-xmin,CENTER-xmin],[0,500],'Color','b','LineWidth',3)
    choice2 = menu('Press yes to confirm zero point','Yes','Reselect'); % Confirm
end

```

```

%% Step 3: Select Curtain AOI (60cm below spreader box exit & centered)
COR = round((0.6*tan(degtorad(angle)))*xscale); %Apply correction factor
AOI = N1((ZERO:ZERO+y_pixels),(CENTER-x_pixels-COR:CENTRE+x_pixels-COR),1); % Crop to
AOI
figure(3), imshow(AOI)

[h1,w1] = size(AOI); % Record AOI dimensions

X_m = (1:w1)/xscale; % Convert pixels in x direction to meters
Y_m = (1:h1)/yscale; % Convert pixels in y direction to meters
NewX = (X_m-X_m(round(w1/2)))*100; % Adjust X values from zero [0 @ center]
NewY = (Y_m-Y_m(1))*100; % Adjust Y values from zero [cm];



---


%% Step 4: Crop all images to AOI & apply Gaussian Smoothing & Thresholding

G = fspecial('gaussian',[6 6],1);% Create Gaussian filter

for index = 2:length(A); % Beginning from second image
    PIC = imread(A(index).name);
    PIC_rot = imrotate(PIC(:,1),270-angle, 'bilinear'); % Rotate image
    VIS_IMS(:,:,index) = PIC_rot((ZERO:ZERO+y_pixels),(CENTER-x_pixels-COR:CENTRE+x_pixels-
COR));% Crop to AOI
    VIS_IMS_SMOOTH(:,:,index) = mat2gray(imfilter(VIS_IMS(:,:,index),G,'same'));% Apply filter

    level = multithresh(VIS_IMS_SMOOTH(:,:,index),2);% Find Otsu's 2-level threhsold values
    VIS_IMS_FINAL(:,:,index) = imquantize(VIS_IMS_SMOOTH(:,:,index),level);% Apply threshold to
image
end

%IMAGES ARE READY FOR DATA ANALYSIS
%%%%%%%%%%%%%

```

## Part 2: IR Image Pre-processing

*Note: Replace VIS image import with a call to an excel spreadsheet. All IR data was recorded in four blocks in each Excel worksheet. This code removes unwanted cells and compiles the image directly.*

---

```

%% Import data from excel for first image
[~, SHEETS] = xlsfinfo('ThirtyIR_20mm.xlsx');

% Import the image 'i'
image = xlsread('ThirtyIR_20mm',SHEETS{i}, 'B10:IG1295'); %generic crop region
im1 = fliplr([image(1:320,:);image(645:964,:); image(323:642,:);image(967:1286,:)]);

```

---

### Part 3: VIS Image Edge Detection

(cont. following pre-processing of VIS image)

---

```

outer = zeros(h1,2); % Prepare array for storing edge indexes
inner = zeros(h1,2); %

for z = 1:length(A);

    VG(:,:,z) = abs(gradient(VIS_IMS_FINAL(:,:,z))); % Void fraction gradient of threshold image

    for i = 1:h1;
        row = VG(i,:,z);           % within each row
        tally = find(row'==0.5); % find when a gradient of 0.5 occurs (i.e. peak)

        if length(tally)==8;      % Check that exactly 4 peaks lie in the data (edges)
            outer(i,:,z) = [tally(2,1),tally(7,1)]; % Pinpoint outer edges
            inner(i,:,z) = [tally(4,1),tally(5,1)]; % Pinpoint inner edges
        else
            outer(i,:,z) = NaN; % If more than four peaks, do not accept (noise)
            inner(i,:,z) = NaN; %
        end
    end
    inner_width (:,z) = ((inner(:,2,z) - inner(:,1,z))/xscale) * 100; % [cm]
    outer_width (:,z) = ((outer(:,2,z) - outer(:,1,z))/xscale) * 100; % [cm]

    inner_av_L(:,z) = inner(:,1,z);          % Determine inner and outer widths left and right
    inner_av_R(:,z) = inner(:,2,z);
    outer_av_L(:,z) = outer(:,1,z);
    outer_av_R(:,z) = outer(:,2,z);
end

LEFT_I = mean(transpose(inner_av_L),'omitnan'); % Average
RIGHT_I = mean(transpose(inner_av_R),'omitnan');
LEFT_O = mean(transpose(outer_av_L),'omitnan');
RIGHT_O = mean(transpose(outer_av_R),'omitnan');

edges = [LEFT_I; RIGHT_I; LEFT_O; RIGHT_O]; % Compile resulting edges

%% NOW work out standard deviations
for tt = 1:h1;
    SD_LEFT_I(:,tt) = std(inner_av_L(tt,:),'omitnan');
    SD_RIGHT_I(:,tt) = std(inner_av_R(tt,:),'omitnan');
    SD_LEFT_O(:,tt) = std(outer_av_L(tt,:),'omitnan');
    SD_RIGHT_O(:,tt) = std(outer_av_R(tt,:),'omitnan');
end

SDs_LEFT_I(:,tt) = smooth(SD_LEFT_I,0.1,'sgolay');
SDs_RIGHT_I(:,tt) = smooth(SD_RIGHT_I,0.1,'sgolay');
SDs_LEFT_O(:,tt) = smooth(SD_LEFT_O,0.1,'sgolay');
SDs_RIGHT_O(:,tt) = smooth(SD_RIGHT_O,0.1,'sgolay');

SDs = [SDs_LEFT_I; SDs_RIGHT_I; SDs_LEFT_O; SDs_RIGHT_O];

```

---

### Part 3: IR Image Edge Detection

(cont. following pre-processing of VIS image)

---

```

%% Find & distinguish b/w inner and outer edge location
outer = zeros(h2,2); % Prepare array for storing edge indexes
inner = zeros(h2,2); %

for z = 1:30; % For all 30 images in series

    TG(:,:,z) = abs(gradient(IR_IMS(:,:,z))); % Temperature gradient of threshold image

    x_L = 1:round(w2/2);
    x_R = round(w2/2):w2;

    TG_LEFT = TG(:,x_L,z);
    TG_RIGHT = TG(:,round(w2/2):w2,z);

    for i = 1:h2; % For all rows in each image
        row_L = TG_LEFT(i,:); % Select left-hand data
        row_R = TG_RIGHT(i,:); % Select right-hand data

        TG_func_L(i,:) = polyfit(x_L,row_L,3); % Fit polynomial
        TG_f_L(i,:) = polyval(TG_func_L(i,:),x_L);

        der_func_L(i,:) = polyder(TG_func_L(i,:)); % Derive & calculate roots
        edges_L(i,:) = roots(der_func_L(i,:));

        TG_func_R(i,:) = polyfit(x_R,row_R,3); % Fit polynomial
        TG_f_R(i,:) = polyval(TG_func_R(i,:),x_R);

        der_func_R(i,:) = polyder(TG_func_R(i,:)); % Derive & calculate roots
        edges_R(i,:) = roots(der_func_R(i,:));

    end

    edges_L(edges_L<0) = nan;
    edges_R(edges_R<0) = nan;

    edges_all(:,:,z) = [edges_L(:,2), edges_L(:,1), edges_R(:,2),edges_R(:,1)];

end

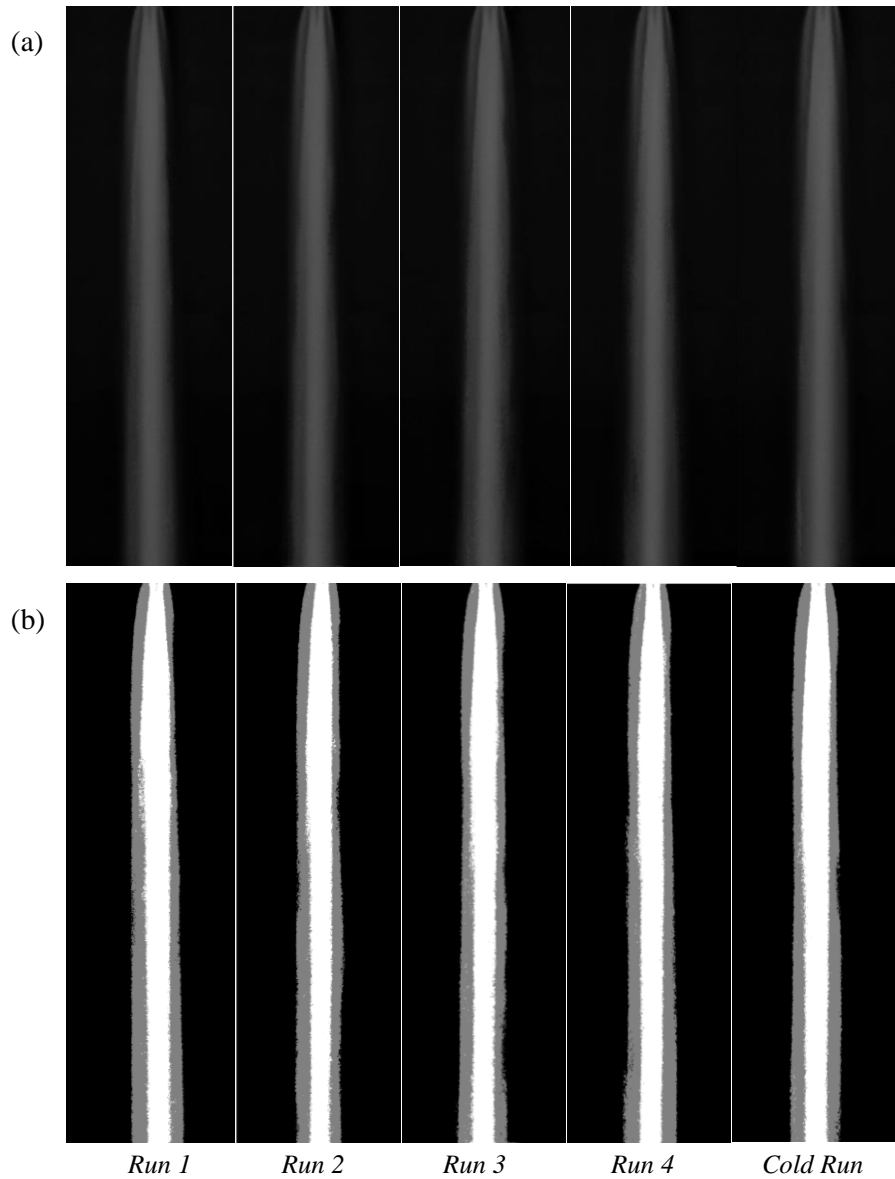
%% Compute dynamic standard deviation
for ss = 1:h2;
    for yy = 1:4;
        av_edge(ss,yy) = mean((edges_all(ss,yy,:)),'omitnan');
    end
end

av_edge_smooth = smooth(av_edge,0.1,'sgolay'); % [cm] Smooth the average profiles

```

## Appendix 10, VIS Image Threshold Consistency

Raw (a) and MATLAB processed VIS images (b) of four independent curtain runs, along with a single cold run. Taken with the 20mm slot width. While the cold curtain run appeared – by eye – to be identical to the hot curtains, it was confirmed (over page) that a statistically significant difference existed in the ratios of white to grey regions.



The ratios presented in suggest that for a given curtain cross-section, a greater area of fuzz is observed for hot curtains compared to ambient ones. The existence of a pressure differential between the air inside and outside the curtain could be directing airflow inwards. This would increase the ratio of curtain area assigned to a low solids volume fraction, explaining this effect.

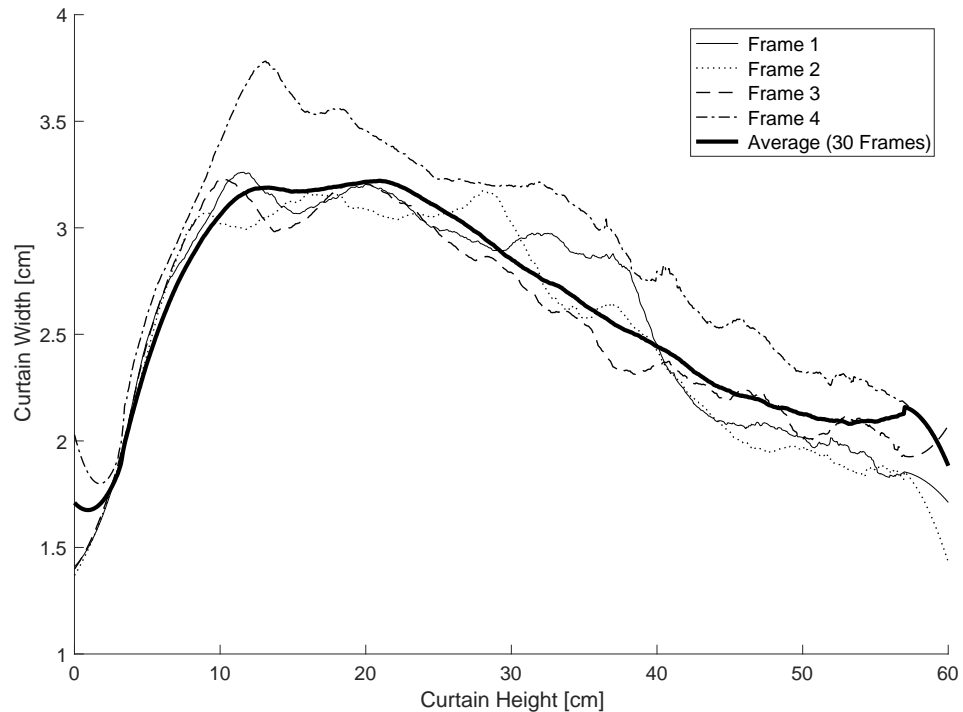
T-test performed at the 95% confidence interval on five hot and five cold runs. Presented are the ratios of white to grey regions (as determined from VIS imagery thresholding). Results confirm that a statistically significant difference existed between the two datasets, implying that the thermal conditions for IR & VIS images must be kept consistent.

	Run No.	Ratio of White to Grey Region	Average	P-Two-tail	Null Hypothesis Rejected?
Hot Curtain	1	1.117			
	2	1.077			
	3	1.135	1.086		
	4	1.024			
	5	1.076			
Cold Curtain	1	1.163		0.002731	Yes
	2	1.187			
	3	1.197	1.191		
	4	1.182			
	5	1.226			

## Appendix 11, VIS Image Repeatability

Examples are provided for the 20mm slot width.

*Inner curtain width vs. curtain height for four individual frames, overlaid 30-frame average.*

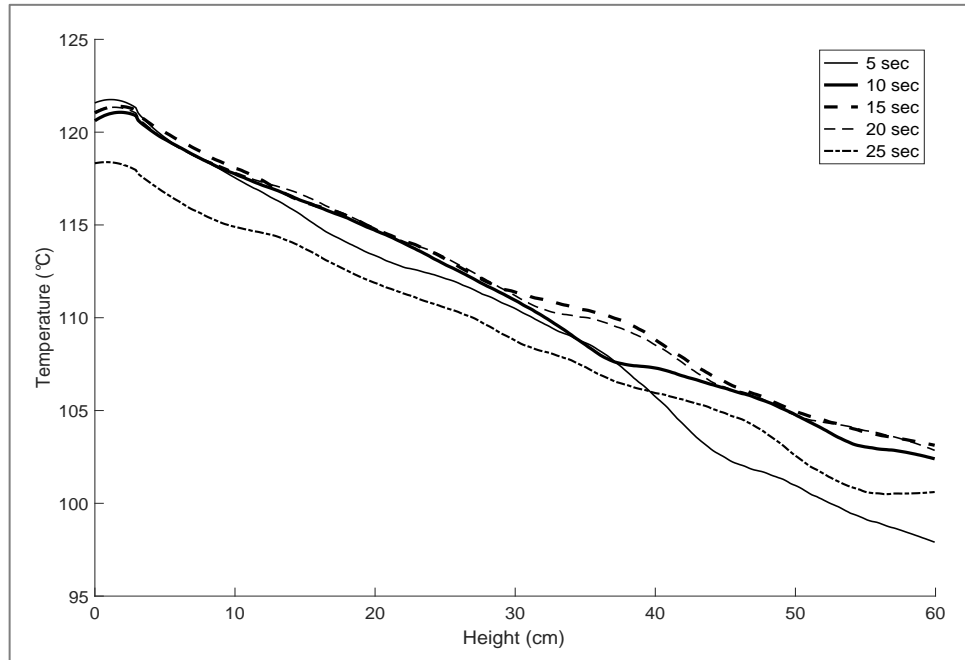


*Inner curtain width vs. curtain height for four individual frames, overlaid 30-frame average.*

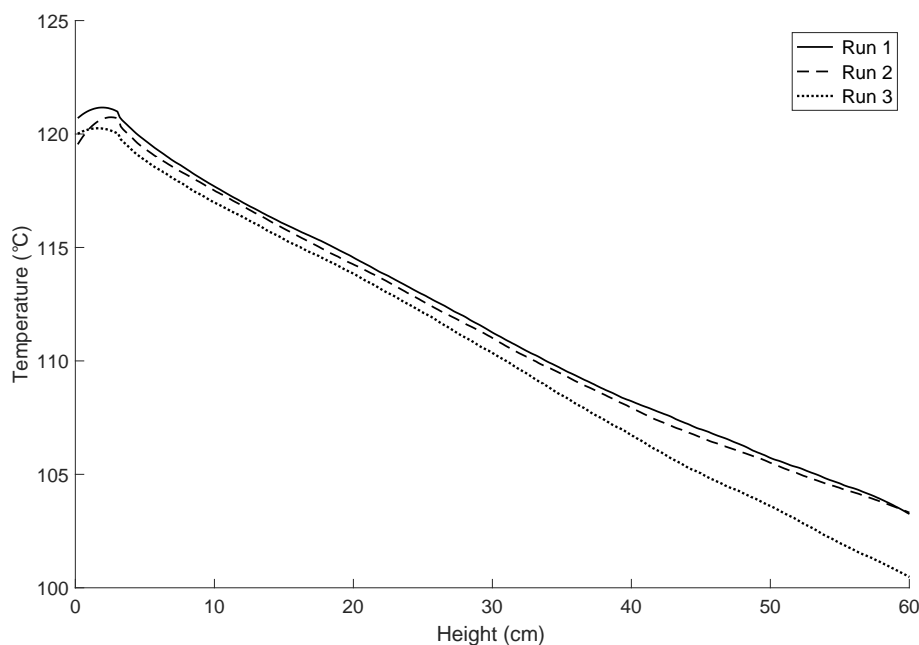
## Appendix 12, IR Image Repeatability

Examples shown for 60mm slot width.

*Centerline temperature profiles at five-second intervals following valve release:*



*Centreline temperature profiles for three distinct tests:*



Consistent for all experimental conditions were observed for all bar Run 3, whose maximum hopper temperature was 0.8°C less than Runs 1 and 2.